Structural control of amorphous films of organic semiconductors and its effect on electrical and luminescence properties

江﨑, 有

https://doi.org/10.15017/4060121

出版情報：九州大学, 2019, 博士（工学）, 課程博士
バージョン：
権利関係：

2020

Doctor Thesis

Structural control of amorphous films of organic semiconductors and its effect on electrical and luminescence properties

Yu Esaki

Department of Chemistry and Biochemistry

Graduate School of Engineering

Kyushu University

Contents

Chapter 1

Introduction

1-1. Research background

1-1-1. Organic light-emitting diodes

Organic light-emitting diodes (OLEDs) have attracted wide interests as next-generation displays and lighting devices. Since OLEDs based on a multilayered structure having a hole transport and a fluorescent organic emitter were reported by C. W. Tang *et al*. [1], OLED performance has been rapidly improved. However, internal quantum efficiency of classic fluorescent OLEDs is limited at 25% because radiative singlet excitons and non-radiative triplet excitons are formed in a 1:3 ratio after the recombination of electrons and holes injected from electrodes. To overcome this 25% limit, room-temperature phosphorescent emitters, such as iridium complexes, were developed [2]. With the phosphorescent emitters, internal quantum efficiency could be increased to ~100% because of the efficient intersystem crossing from the singlets to the triplets and the highly efficient phosphorescence from the triplets. In 2012, our group in Kyushu University discovered that thermally activated delayed fluorescence (TADF) is promising for achieving an internal quantum efficiency of 100% [3]. TADF-based organic emitters have a very small energy gap between the singlets and the triplets by carefully designing their chemical structures, leading to the efficient reverse intersystem crossing from the non-radiative triplets to the radiative singlets. Additionally, driving voltage and operational stability of OLEDs have also been improved by developing new organic semiconductor materials, device structures, and encapsulation technology. Thorough the comprehensive researches and developments in last 30 years, OLEDs are now on the commercialization stage.

Many advantages of OLEDs derive from the unique characteristics of organic materials. One is the flexibility of their chemical structures with different functionalities. This provides a wide range of the material choice for OLED fabrication. For OLEDs, several elastic films of organic materials are fabricated on a substrate, including a flexible plastic substrate, using simple vacuum deposition or solution process, making it possible to obtain light and flexible devices at a lower cost.

In OLEDs, holes and electrons are injected from electrodes and, then, recombine to form excitons for light emission. To carry holes and electrons efficiently, OLEDs are composed of several stacked organic films, each of which has an ability of hole transport, emission, or electron transport. Because these films are very thin, each with a thickness of tens of nanometers, uniform and pinhole-free amorphous organic films are commonly used in OLEDs.

Typical strategies to improve OLED performance are a design of new organic materials which have higher carrier mobility and more efficient luminescence and an optimization of device structures considering energy levels of organics, a recombination zone, and light propagation paths. On the other hand, it has been revealed that the structural control of amorphous films is also effective for enhancing OLED performance [4–8]. An understanding of the relationship between amorphous film structures, electrical properties, and OLED performance is very important for establishing fundamental science and developing OLED industry. However, how film density affects OLED performance has not well been studied while controlling molecular orientation is known to be a key to improve OLED performances [4–7]. In this thesis, I performed a comprehensive study regarding both molecular orientation and film density. In this chapter, I introduce amorphous structures of organic films, their problems, and research backgrounds. Finally, I mention the research purpose and the outline of this thesis.

1-1-2. Structure of organic films

Electrical and luminescence properties of amorphous films of organic materials are determined by not only the nature of molecular structures but also their film structures. In other words, these properties can be controlled even in the same materials. Basically, films of low-molecular-weight organic materials are categorized into two types: polycrystalline films and amorphous films. Structural models of polycrystalline and amorphous films fabricated using a vacuum deposition process are shown in **Fig. 1-1**. Planar molecules have strong intermolecular interaction and tend to form polycrystalline films. There are macroscopic voids between crystallites and other crystallites or a substrate in polycrystalline films. On the other hand, bulky molecules having weak intermolecular interaction are difficult to form a crystal phase, resulting in the formation of films with a disordered amorphous state. In amorphous films, a number of microscopic voids (namely, free volume) exist. These voids in polycrystalline and amorphous films would affect the film density; the larger amount of voids makes their film density low and causes the following problems:

(1) Voids work as carrier traps and energy barriers and, therefore, lower the carrier transport through films [9–11].

(2) Voids work as penetration paths for water and oxygen molecules and, therefore, lower the electrical and structural stability of films in air [12,13].

If these problems can be solved by removing voids from films through the optimization of vacuum deposition conditions, the electrical properties and stability of organic films would be enhanced.

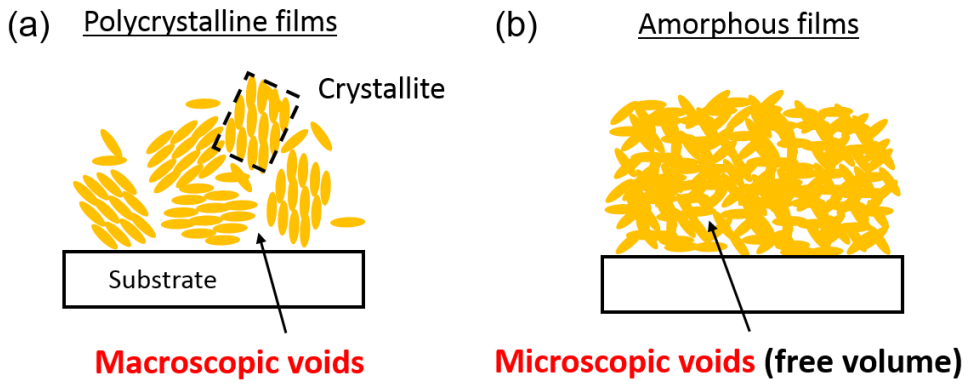

Fig. 1-1. Structural models of (a) polycrystalline and (b) amorphous films of organic materials.

1-1-3. Structural control of polycrystalline films

As one method to remove macroscopic voids in polycrystalline films, in my master thesis, I investigated the compression of organic films by applying high pressure using a cold isostatic pressing (CIP) method [14,15]. After the compression, the thicknesses of polycrystalline metal-free phthalocyanine (H_2PC) films decreased by approximately 40%, indicating a removal of voids from films and an increase in film density. **Figure 1-2**(a) exhibits current density (*J*)–voltage (*V*) curves of as-deposited and CIP-treated H_2PC films. Current densities were enhanced by three orders of magnitude after the compression in a whole voltage range, corresponding to a 2000-fold enhancement of hole mobilities. I found that this current enhancement was because of not only the rotation of crystallites to a direction in which carrier transport is more favorable, but also an improvement of the carrier conduction paths associated with a reduction of macroscopic voids. I carried out this CIP treatment on a wide variety of organic films. The current enhancement ratio increased as the compression ratio increased as shown in **Fig. 1-2**(b). All polycrystalline films were compressed by the CIP treatment and, therefore, their current densities were enhanced. The current enhancement was more significant when the compression ratio was higher. On the other hand, it was difficult to modulate the densities of amorphous films and improve their current densities using this CIP treatment.

Although the compression was not effective for the amorphous films, the aforementioned results proved that there was a clear relationship between the film densities and the current densities of polycrystalline films. Therefore, it is probable that the electrical properties of amorphous films are also improved if the film density can be increased using other methods.

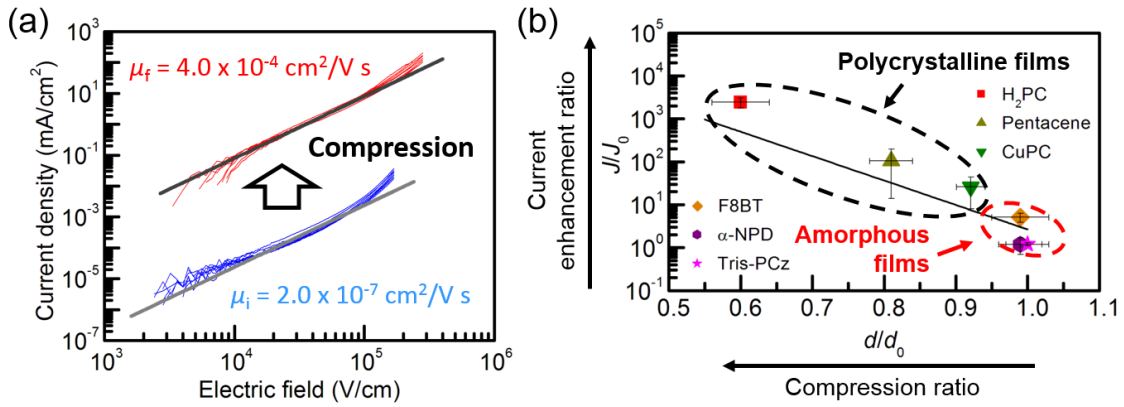

Fig. 1-2. (a) Current density (J)–voltage (V) curves of as-deposited (blue lines) and CIP-treated (red lines) H_2PC films and (b) relationship between the ratios of current densities J/J_0 (current enhancement ratio) and film thicknesses d/d_0 (compression ratio) before and after the CIP treatment. The structure of the devices was glass substrate/indium tin oxide (ITO)/organic layer/Al. These results were taken from my master thesis.

1-1-4. Structural control of amorphous films

Amorphous is a quasi-stable state as a result of kinetic relaxation of molecules. Although amorphous structures do not have a long-range ordering, it is misunderstanding that molecules are always random in amorphous systems. Since Lin *et al.* reported an optical anisotropy in vacuum-deposited amorphous organic films [16], many researchers started investigating the structures of amorphous films and developing methods to control amorphous structures.

Yokoyama *et al.* found that a variety of amorphous films of typical organic semiconductor materials showed optical anisotropy [17]. This anisotropy can be controlled by substrate temperature during vacuum deposition [18]. Because spin-coated films of organic materials are isotropic, this phenomenon is specific to a vacuum deposition process [19]. It was also confirmed that vacuum-deposited films exhibited higher thermal stability and density than spin-coated films and that these characteristics disappeared after annealing over the glass transition temperature of organic films [19]. Ediger *et al.* and several researchers also revealed a detailed film formation mechanism during vacuum deposition and named the vacuum-deposited amorphous films with high thermal stability, density, and anisotropy as “stable glasses” in contrast to “ordinary glasses” fabricated by liquid cooling or spin-coating [20–24].

The key to obtain the stable glass films is a kinetics of molecules, namely, how each organic molecule moves and stops (stabilizes) on a film surface during film formation. The relationship between the kinetics of molecules and the final amorphous structure is summarized in **Fig. 1-3**. Note that the molecular orientation shown in the figure is valid for long-stick-shaped molecules. During vacuum deposition, molecules which reach the film surface do not stop immediately and move around until molecules find a stable position or are buried by next-coming molecules. This process sometimes looks like a famous video game “Tetris.” The motion of molecules can be understood considering a kinetic energy of molecules and explained by an energy landscape. Molecules can test many configurations and positions on the film surface, and each condition corresponds to a certain free energy. Although the number of states which molecules can take is very large because of the bulky and flexible molecular structures, the stable state with better packing (large enthalpic gain) is quite limited. Therefore, the energy landscape in **Fig. 1-3** has many energetic valleys, but most of them are shallow. Because the structures of as-deposited amorphous films are the result of repeated relaxations,

the kinetics of molecules dominates the final film structure. There are three patterns of the relaxation processes concerning the kinetic energy of molecules, as summarized below. A substrate temperature (T_{sub}) during vacuum deposition can be used to control the kinetic energy. The conditions of T_{sub} corresponding to these three patterns are also appended in the figure. The glass transition temperature (T_g) of ordinary glasses is typically used as a reference temperature because the glass transition reflects the relationship between a local molecular motion and a temperature.

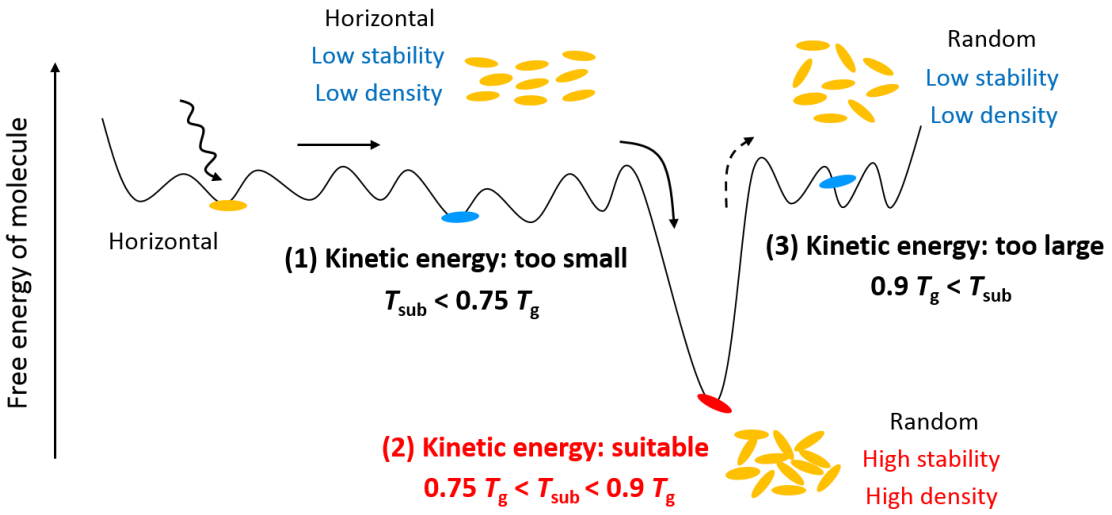

Fig. 1-3. Energy landscape, molecular kinetics, and structural models of vacuum-deposited amorphous films of long-stick-shaped molecules.

(1) Too small kinetic energy ($T_{sub} < 0.75\ T_g$):

Kinetic energy of molecules is not sufficient and the number of states which molecules can test is limited, so that most of molecules cannot find a deep valley position and stop in a shallow one. The molecules have small enthalpic gain and inferior packing, resulting in low thermal stability and low density of amorphous films. Basically, the molecules orientate horizontally on the film surface to obtain enthalpic gain at the moment of landing.

(2) Suitable kinetic energy ($0.75\ T_g < T_{sub} < 0.9\ T_g$):

Kinetic energy of molecules is sufficient and molecules can test many states, so that molecules can stop in a deep valley position with a high probability. Therefore, the molecules obtain large

enthalpic gain and better packing, resulting in the formation of films with high thermal stability and high density. It is difficult for the molecules to maintain a horizontal orientation after a long-range migration. Thus, the molecules in amorphous films become random.

(3) Too large kinetic energy (0.9 $T_g < T_{sub}$):

Although molecules once find a stable position, they are released from there due to the excess kinetic energy and continue migration until molecules are buried by next-coming molecules. The molecules lack enthalpic gain and packing. This leads to low thermal stability and density of films. In this case, molecular orientation in amorphous films is slightly vertical relative to the substrate as a result of collisions of molecules and gradually approaches to no orientational order as T_{sub} increases to T_g.

It is known that the kinetic energy of molecules can be controlled by deposition conditions, such as T_{sub} and deposition rate. In this thesis, I mainly changed T_{sub} to fabricate films with different amorphous structures as a simple and most effective method. The range of T_{sub} used in this study corresponded to the three relaxation patterns as I mentioned earlier. The thermal stability and film density are known to exhibit the highest value around 0.75 $T_g < T_{sub} < 0.9$ T_g [case (2) in **Fig. 1-3**]. Molecules near the film surface are easier to move than those in the bulk. The T_g of the film surface is typically smaller than that of the film interior [25,26]. It is conceivable that T_{sub} which can provide the maximum thermal stability and film density corresponds to the T_g of the film surface.

While the mechanism of the amorphous film formation has been clarified to some extent, there are several studies regarding the effect of amorphous structures on the basic electrical properties and OLED performance. It has been reported that horizontal orientation of long-stick-shaped molecules on a substrate increases the transfer integral between adjacent molecules and, therefore, enhances carrier mobility in the substrate-normal direction [18]. Horizontal orientation of transition dipole moments of emitting molecules can increase light outcoupling efficiency [4]. The importance of controlling molecular orientation was experimentally confirmed in actual OLED structures [5–7]. In contrast, detailed study on how film density affects the electrical and photoluminescence (PL) properties and OLED performance has been lacked to date although enhanced photostability [27,28]

and improved external quantum efficiency and operational stability [8] with high-density amorphous films were reported.

Furthermore, vacuum-deposited amorphous films of organic molecules with large permanent dipole moment have strong polarization due to the anisotropic molecular orientation. This phenomenon is known as spontaneous orientation polarization (SOP) [29,30]. The SOP formation mechanism and the relationship to OLED performance have been investigated by comparing the degree of SOP in films of various materials with different molecular shapes and permanent dipole moments. If the SOP of single-material films can be controlled, a further discussion on the SOP formation mechanism and its influence on OLED performance would be possible.

1-2. Research purpose and outline

The main concept of this thesis is summarized in **Fig. 1-4**. Density and molecular orientation of amorphous films are controlled using T_{sub} during vacuum deposition to resolve the aforementioned problems and maximize the functionalities of organic materials. By increasing film density, I aim at improving the carrier conduction paths and suppressing the absorption of water and oxygen molecules into films, leading to the enhanced electrical properties and air stability. Formation of a thermally stable amorphous structure would result in the reduced crystallization and reorientation of molecules and the suppression of the film degradation during continuous operation. If OLEDs with extremely high air stability can be realized, the encapsulation widely used to protect devices from water and oxygen in air is no longer necessary, making a device fabrication cost lower. Furthermore, by tuning molecular orientation, not only the improvement of the light propagation paths but also the control of SOP in devices are expected. Through these studies, I aim at clarifying the detailed relationship between comprehensive amorphous structures (especially film density), fundamental electrical properties, and OLED performance, which is the originality of this thesis.

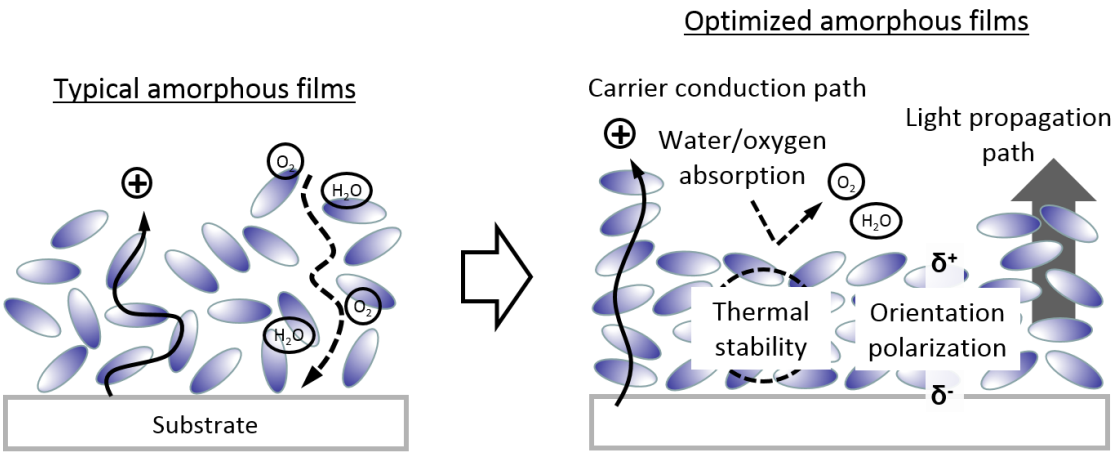

Fig. 1-4. Structural models of typical and optimized amorphous films of organic materials.

I briefly explain the outline of this thesis. In Chapter 2, I discussed the structure and electrical properties of amorphous films of a typical hole-transporting material, *N*,*N*'-di(1-naphthyl)-*N*,*N*'-diphenyl-(1,1'-biphenyl)-4,4'-diamine (α-NPD), controlled by T_{sub} during vacuum deposition. In Chapter 3, I evaluated carrier traps in α-NPD films using a thermally stimulated current method to clarify the origins of the current enhancement in the high-density films. In Chapter 4, I investigated the structure and PL properties of amorphous films of a typical electron-transporting and emitting material, tris(8-hydroxyquinolinato)aluminum (Alq_3), controlled by T_{sub} and deposition rates. In Chapter 5, I fabricated OLEDs with α-NPD and Alq_3 layers having different amorphous structures to prove how SOP induced by the molecular orientation affects OLED performance. In Chapter 6, I summarized main results of this thesis and mentioned future perspectives.

References

[1] C. W. Tang, S. A. VanSlyke, Organic electroluminescent diodes, *Appl. Phys. Lett.* **51**, 913 (1987).

[2] M. A. Baldo, S. Lamansky, P. E. Burrows, M. E. Thompson, S. R. Forrest, Very high-efficiency green organic light-emitting devices based on electrophosphorescence, *Appl. Phys. Lett.* **75**, 4 (1999).

[3] H. Uoyama, K. Goushi, K. Shizu, H. Nomura, C. Adachi, Highly efficient organic light-emitting diodes from delayed fluorescence, *Nature* **492**, 234–238 (2012).

[4] W. Brütting, J. Frischeisen, T. D. Schmidt, B. J. Scholz, C. Mayr, Device efficiency of organic light-emitting diodes: progress by improved light outcoupling, *Phys. Stat. Sol. A* **210**, 44–65 (2013).

[5] T. Komino, H. Nomura, T. Koyanagi, C. Adachi, Suppression of efficiency roll-off characteristics in thermally activated delayed fluorescence based organic light-emitting diodes using randomly oriented host molecules, *Chem. Mater.* **25**, 3038–3047 (2013).

[6] T. Komino, H. Tanaka, C. Adachi, Selectively controlled orientational order in linear-shaped thermally activated delayed fluorescent dopants, *Chem. Mater*. **26**, 3665–3671 (2014).

[7] T. Komino, Y. Sagara, H. Tanaka, Y. Oki, N. Nakamura, H. Fujimoto, C. Adachi, Electroluminescence from completely horizontally oriented dye molecules, *Appl. Phys. Lett.* **108**, 241106 (2016).

[8] J. R. Ribé, P. A. Will, C. Hänisch, M. G. Silveira, S. Lenk, J. R. Viejo, S. Reineke, High-performance organic light-emitting diodes comprising ultrastable glass layers, *Sci. Adv.* **4**, eaar8332 (2018).

[9] G. Horowitz, M. E. Hajlaoui, Mobility in polycrystalline oligothiophene field-effect transistors dependent on grain size, *Adv. Mater.* **12**, 1046–1050 (2000).

[10] T. W. Kelley, C. D. Frisbie, Gate voltage dependent resistance of a single organic semiconductor grain boundary, *J. Phys. Chem. B* **105**, 4538–4540 (2001).

[11] S. Seki, Y. Terashima, Y. Kunimi, T. Kawamori, M. Tashiro, Y. Honda, S. Tagawa, The effects of free volumes on charge carrier transport in polysilanes probed by positron annihilation, *Radiat. Phys. Chem.* **68**, 501–505 (2003).

[12] K. J. Dawson, K. L. Kearns, M. D. Ediger, M. J. Sacchetti, G. D. Zografi, Highly stable indomethacin glasses resist uptake of water vapor, *J. Phys. Chem. B* **113**, 2422–2427 (2009).

[13] R. Surana, A. Pyne, R. Suryanarayanan, Effect of aging on the physical properties of amorphous trehalose, *Pharm. Res.* **21**, 867–874 (2004).

[14] T. Matsushima, Y. Esaki, C. Adachi, Enhancement of the electrical characteristics of metal-free phthalocyanine films using cold isostatic pressing, *Appl. Phys. Lett.* **105**, 243301 (2014).

[15] Y. Esaki, T. Matsushima, C. Adachi, Current enhancement in organic films through gap compression by cold and hot isostatic pressing, *Adv. Funct. Mater.* **26**, 2940–2949 (2016).

[16] H.-W. Lin, C.-L. Lin, H.-H. Chang, Y.-T. Lin, C.-C. Wu, Anisotropic optical properties and molecular orientation in vacuum-deposited ter(9,9-diarylfluorene)s thin films using spectroscopic ellipsometry, *J. Appl. Phys.* **95**, 881–886 (2004).

[17] D. Yokoyama, A. Sakaguchi, M. Suzuki, C. Adachi, Horizontal molecular orientation in vacuum-deposited organic amorphous films, *Appl. Phys. Lett.* **93**, 173302 (2008).

[18] D. Yokoyama, Y. Setoguchi, A. Sakaguchi, M. Suzuki, C. Adachi, Orientation control of linear-shaped molecules in vacuum-deposited organic amorphous films and its effect on carrier mobilities, *Adv. Funct. Mater.* **20**, 386–391 (2010).

[19] M. Shibata, Y. Sakai, D. Yokoyama, Advantages and disadvantages of vacuum-deposited and spin-coated amorphous organic semiconductor films for organic light-emitting diodes, *J. Mater. Chem. C* **3**, 11178–11191 (2015).

[20] S. F. Swallen, K. L. Kearns, M. K. Mapes, Y. S. Kim, R. J. McMahon, M. D. Ediger, T. Wu, L. Yu, S. Satija, Organic glasses with exceptional thermodynamic and kinetic stability, *Science* **315**, 353–356 (2007).

[21] Y. Z. Chua, M. Ahrenberg, M. Tylinski, M. D. Ediger, C. Schick, How much time is needed to form a kinetically stable glass? AC calorimetric study of vapor-deposited glasses of ethylcyclohexane, *J. Chem. Phys.* **142**, 054506 (2015).

[22] S. S. Dalal, D. M. Walters, I. Lyubimov, J. J. de Pablo, M. D. Ediger, Tunable molecular orientation and elevated thermal stability of vapor-deposited organic semiconductors, *Proc. Natl. Acad. Sci.* **112**, 4227–4232 (2015).

[23] A. Gujral, K. A. O'Hara, M. F. Toney, M. L. Chabinyc, M. D. Ediger, Structural characterization of vapor-deposited glasses of an organic hole transport material with X-ray scattering, *Chem. Mater.* **27**, 3341–3348 (2015).

[24] J. Jiang, D. M. Walters, D. Zhou, M. D. Ediger, Substrate temperature controls molecular orientation in two-component vapor-deposited glasses, *Soft Matter* **12**, 3265–3270 (2016).

[25] T. Komino, H. Nomura, M. Yahiro, C. Adachi, Real-time measurement of molecular orientational randomization dynamics during annealing treatments by in-situ ellipsometry, *J. Phys. Chem. C* **116**, 11584–11588 (2012).

[26] S. S. Dalal, M. D. Ediger, Influence of substrate temperature on the transformation front velocities that determine thermal stability of vapor-deposited glasses, *J. Phys. Chem. B* **119**, 3875–3882 (2015).

[27] Y. Qiu, L. W. Antony, J. J. de Pablo, M. D. Ediger, Photostability can be significantly modulated by molecular packing in glasses, *J. Am. Chem. Soc.* **138**, 11282–11289 (2016).

[28] Y. Qiu, L. W. Antony, J. M. Torkelson, J. J. de Pablo, M. D. Ediger, Tenfold increase in the photostability of an azobenzene guest in vapor-deposited glass mixtures, *J. Chem. Phys.* **149**, 204503 (2018).

[29] E. Ito, Y. Washizu, N. Hayashi, H. Ishii, N. Matsuie, K. Tsuboi, Y. Ouchi, Y. Harima, K. Yamashita, K. Seki, Spontaneous buildup of giant surface potential by vacuum deposition of Alq_3 and its removal by visible light irradiation, *J. Appl. Phys.* **92**, 7306–7310 (2002).

[30] Y. Noguchi, W. Brütting, H. Ishii, Spontaneous orientation polarization in organic light-emitting diodes, *Jpn. J. Appl. Phys.* **58**, SF0801 (2019).

Chapter 2

Enhanced electrical properties and air stability of amorphous organic thin films by engineering film density

Y. Esaki, T. Komino, T. Matsushima, and C. Adachi
The Journal of Physical Chemistry Letters **8**, 5891–5897 (2017).

2-1. Introduction

Amorphous films composing OLEDs include microscopic voids originating from inefficient molecular packing. The presence of these voids are known to strongly limit charge-carrier injection and transport [1–3] and allow oxygen and water molecules to penetrate into organic films, causing the current–voltage properties and air stability of organic devices to deteriorate [4–6]. Some researchers have suggested that increasing the density of amorphous organic films results in lower moisture penetration [7,8]. In this thesis, I focus my attention on controlling T_{sub} during vacuum deposition of amorphous organic films to decrease the voids in films and increase the film density. If highly densified amorphous films can be obtained by controlling T_{sub}, these films should display enhanced electrical properties and air stability. In this chapter, I comprehensively investigate the influence of T_{sub} on the film density, molecular orientation, electrical properties, and air stability of amorphous α-NPD films. I reveal that an increase of film density achieved by controlling T_{sub} simultaneously leads to enhanced electrical properties and air stability. Although T_{sub} also controls the molecular orientation, molecular orientation has less influence than density on electrical properties and air stability of the α-NPD films.

2-2. Results and discussion

2-2-1. Film structure analysis

I used α-NPD purchased from Nippon Steel & Sumikin Chemical to fabricate films and devices because it is widely known to form amorphous films by vacuum deposition [9]. The chemical structure of α-NPD is shown in the inset of **Fig. 2-4**(a). For the measurements of density and molecular orientation, α-NPD films with a thickness of approximately 100 nm were vacuum-deposited on Si substrates kept at various T_{sub} ranging from 212 to 342 K. The Si substrates were pre-cleaned by ultrasonication in acetone, detergent, pure water, and isopropanol, followed by UV/O_3 treatment. T_{sub} was calibrated with an alumel/chromel thermocouple attached to the substrate surface beforehand. The pressure and deposition rate during the vacuum deposition of α-NPD were of the order of 10^{-4} Pa and 0.13 ± 0.03 nm/s, respectively. α-NPD films obtained at this T_{sub} range were in the amorphous state and had very smooth surfaces without pinholes. In contrast, α-NPD films fabricated at T_{sub} = 200 K were opaque and had large surface roughness. I speculate that water molecules condensed in the films during α-NPD deposition at this T_{sub} and then evaporated from films when T_{sub} was increased to room temperature after the deposition, which may result in the rough surface.

Variable angle spectroscopic ellipsometry (VASE; M-2000, J. A. Woollam) was performed on the vacuum-deposited α-NPD films on Si substrates to evaluate their molecular orientation, refractive index n, extinction coefficient k, and film thickness d. In the VASE measurements, the incident light angle ranging from 45° to 75° with a step of 5° and the spectral range was 245–1000 nm. As I discuss later, the molecular orientation evaluated by VASE changed markedly depending on T_{sub}, corresponding to a change of the transition dipole orientation of α-NPD molecules in the films. The transition dipole moment of α-NPD is known to be parallel to its long molecular axis [10]. The n and k spectra of organic semiconductor films are known to show anisotropy between the directions parallel and perpendicular to the substrate plane because of the orientation of molecules, even in amorphous films [10–17]. Experimentally obtained Ψ and Δ curves were analyzed with an optical model considering uniaxial anisotropy based on an ordinary glass of α-NPD. The model was composed of Gaussian-type and Tauc–Lorentz-type oscillators to simultaneously obtain d values and spectra of n and k in each axis. The oscillator model parameters are shown in **Table 2-1** and **2-2**. Several examples of fitting results are presented in **Fig. 2-1**.

Table 2-1. Oscillator model parameters (Gaussian).

Oscillator type	Amplitude	Energy (eV)	Breadth (eV)
Gaussian	1.0859	3.5807	0.53957
Gaussian	0.5599	4.444	0.84802
Gaussian	1.8865	5.6488	0.83336

Table 2-2. Oscillator model parameters (Tauc–Lorentz).

Oscillator type	Amplitude	Energy (eV)	C (eV)	Gap energy (eV)
Tauc–Lorentz	42.477	3.134	0.39286	2.944

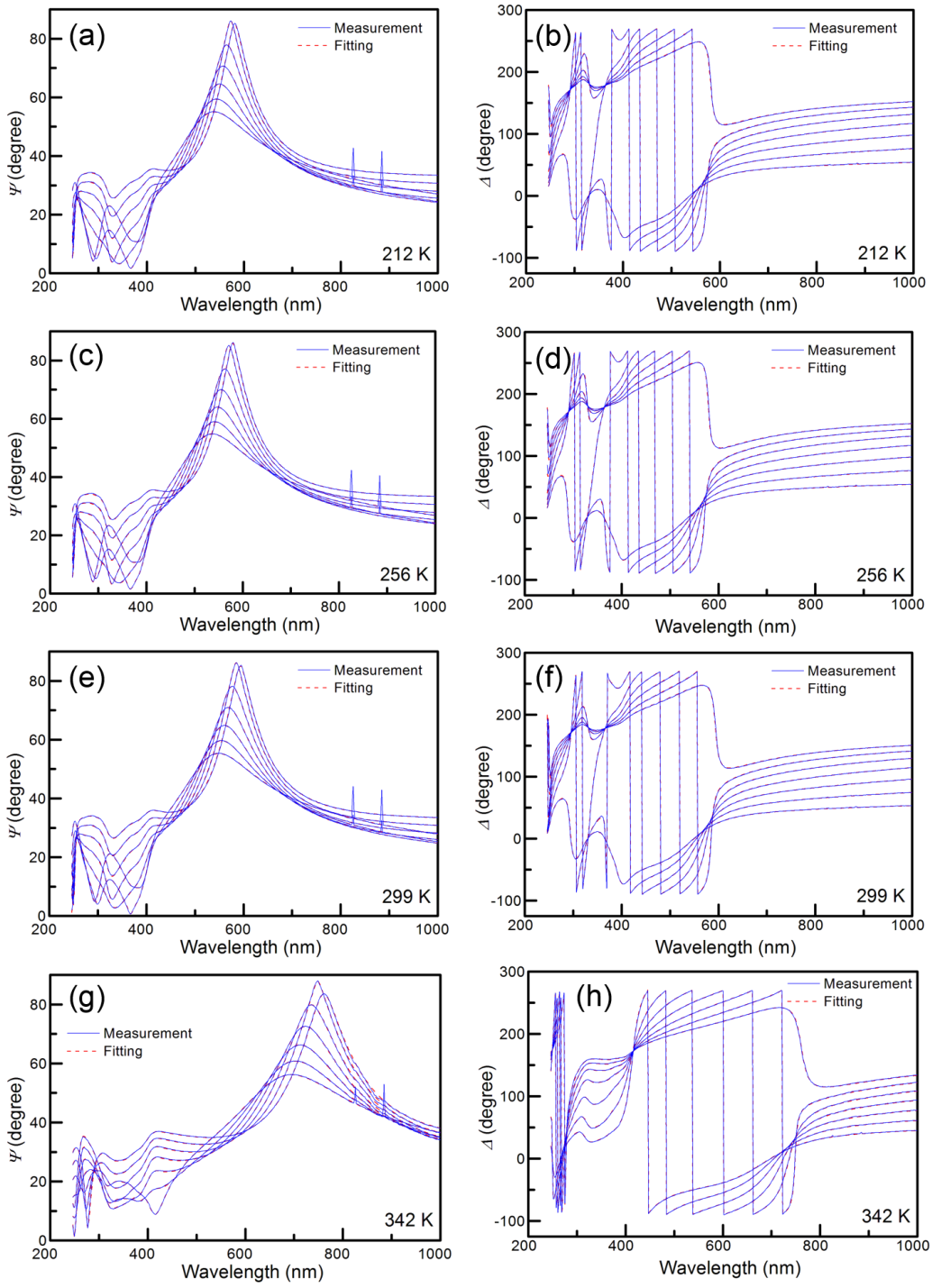

Fig. 2-1. (a, c, e, g) Ψ and (b, d, f, h) Δ curves of α-NPD films vacuum-deposited at different T_{sub}. The experimental data (blue solid lines) was successfully fitted with the model (red dashed lines).

The accuracy of my optical model was confirmed by comparing the mean-squared error (MSE). **Figure 2-2** shows MSE values for α-NPD films vacuum-deposited at a T_{sub} of 212 K. The MSE showed the lowest value at a d of 88.474 nm. I chose this value as the real α-NPD thickness. When I increased or decreased the thickness parameter by 0.1 nm, the MSE value clearly rose as shown in this figure. This result indicates that a small change of film thickness can be detected by my optical model.

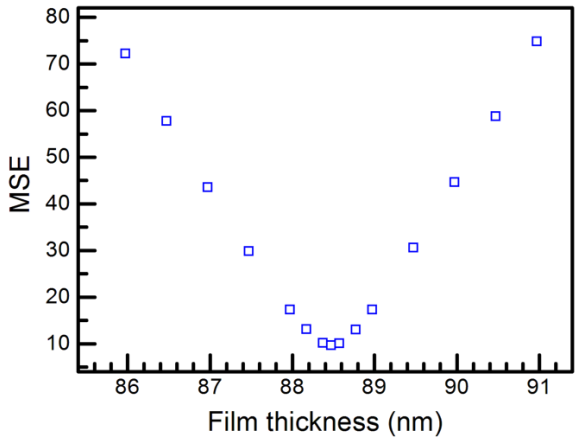

Fig. 2-2. Plot of MSE values as a function of film thickness for an α-NPD film vacuum-deposited at a T_{sub} of 212 K.

The molecular orientation in each α-NPD film was then evaluated by calculating the orientation order parameter (S), which is defined as [14,16]:

$$S = \frac{3\langle\cos^2\theta_{TDM}\rangle - 1}{2} = \frac{k_z - k_x}{k_z + 2k_x}, \qquad (2\text{-}1)$$

where θ_{TDM} is the orientation degree of transition dipole moment of the molecules to the substrate-normal direction and k_{x} and k_{z} are the extinction coefficients in the directions parallel and perpendicular to the substrate plane, respectively.

For the measurement of relative film density (ρ_{rel}), α-NPD films were annealed under vacuum (< 1.0×10^{-3} Pa) for 30 min at 381 K after the first VASE measurements, and then cooled to room temperature at a certain rate. This annealing temperature was higher by about 20 K than the glass transition temperature of a bulk α-NPD film ($T_{\mathrm{g,\ bulk}}$ = 362 K) [11]. The thermal annealing is known to result in the formation of randomized molecular films with a certain density (ordinary glasses), the value of which is generally lower than that of as-deposited films, as reported previously [10,11,17]. Thus, the annealed films can be used as references to compare the density of the as-deposited films. The annealed films were measured using VASE again. VASE after the annealing evidently indicated the randomization of α-NPD molecules accompanied with the change of optical parameters n and k and a slight increase of d in the annealed films compared with that before annealing. It should be noted that no obvious crystallization was observed in all films after the annealing. Assuming that the film area and the material weight on a substrate are unchanged before and after annealing, ρ_{rel} values are given by,

$$\rho_{rel} = \frac{d_{annealed}}{d_{as-deposited}}, \qquad (2\text{-}2)$$

where d_{annealed} and $d_{\mathrm{as\text{-}deposited}}$ are the thicknesses of the annealed and as-deposited films, respectively.

Figure 2-3(a–d) display the n and k spectra of α-NPD films vacuum-deposited at T_{sub} = 212, 256, 299, and 342 K. While n_x and k_x were similar to n_z and k_z for films vacuum-deposited at T_{sub} = 342 K, anisotropy of both n and k began to appear and became larger at low T_{sub}. The large anisotropy of the n and k spectra can be attributed to the anisotropy of the molecular orientation of α-NPD [10–17].

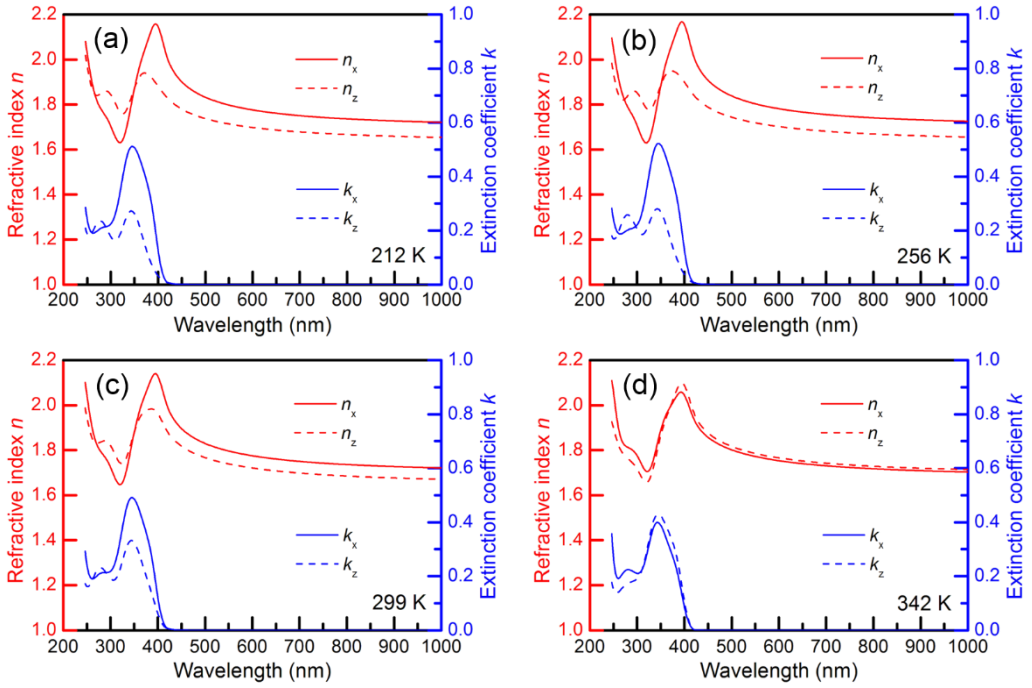

Fig. 2-3. Refractive index n and extinction coefficient k spectra of representative α-NPD films vacuum-deposited on substrates kept at different substrate temperatures (T_{sub}) of (a) 212, (b) 256, (c) 299, and (d) 342 K.

The S values estimated from the spectra at a wavelength of 344 nm using **Eq. (2-1)** are plotted as a function of T_{sub} in **Fig. 2-4**(a). Molecules (transition dipole moments) are vertically oriented, random, and horizontally oriented at S values of 1, 0, and −0.5, respectively. Therefore, the S value of nearly 0 for films vacuum-deposited at T_{sub} = 342 K indicates the randomization of α-NPD molecules. The S value decreased as T_{sub} was lowered, indicating a gradual change from random to horizontal orientation of α-NPD molecules. Below T_{sub} ~250 K, the S values became almost constant. Similar T_{sub}-dependent orientations have been observed for other organic films [11–13].

The ρ_{rel} values at each T_{sub}, which were calculated from the change of d with **Eq. (2-2)**, are plotted against T_{sub} in **Fig. 2-4**(b). I found that ρ_{rel} was a convex function of T_{sub} and that the maximum ρ_{rel} was between 270 and 300 K (0.75−0.83 $T_{g, bulk}$), which is close to a previous report [11].

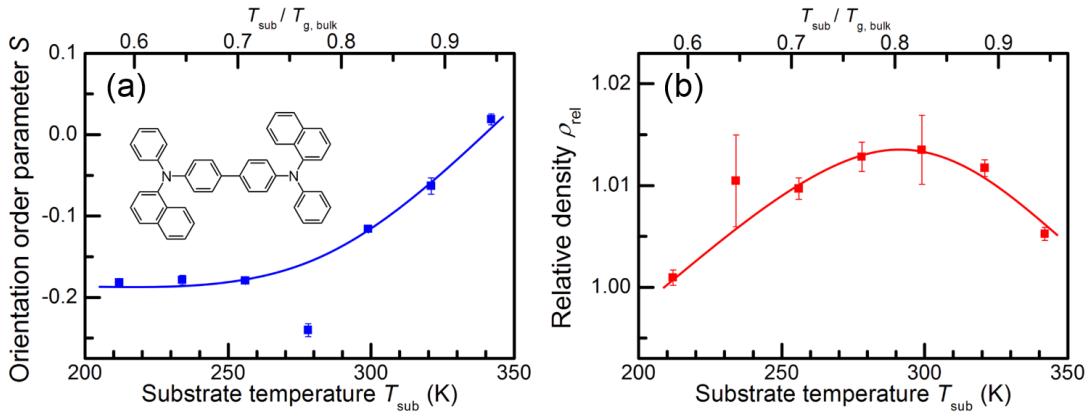

Fig. 2-4. Plots of (a) orientation order parameter S and (b) relative density ρ_{rel} as a function of substrate temperature (T_{sub}) during vacuum deposition. The chemical structure of α-NPD is shown in the inset of (a).

To check the accuracy of the analysis, ρ_{rel} values were compared to those estimated from n of α-NPD films using the generalized Lorentz–Lorenz equation [11,17]:

$$\frac{\langle n^2\rangle-1}{\langle n^2\rangle+2}=\frac{4\pi}{3}\frac{N_A\alpha}{M_w}\rho \propto \rho \qquad (2\text{-}3) \qquad \text{and}$$

$$\langle n^2\rangle=\frac{2{n_x}^2+{n_z}^2}{3}, \qquad (2\text{-}4)$$

where N_A is the Avogadro constant, M_w is the molecular weight (588.74 g/mol for α-NPD), and α is the molecular polarizability. **Figure 2-5** shows plots of ρ_{rel} values estimated from the change of d values and n values at a wavelength of 600 nm, where the films have no absorption, as a function of T_{sub}. The ρ_{rel}-T_{sub} plot estimated from n was found to be similar to that estimated from d.

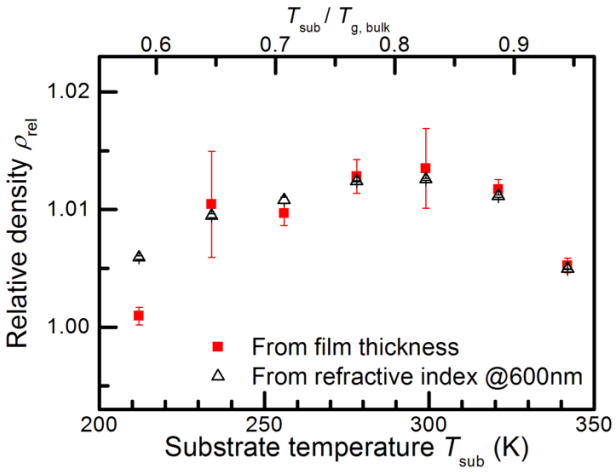

Fig. 2-5. Plots of ρ_{rel} estimated from the film thicknesses d (red) and refractive indexes n (black) of α-NPD films as a function of T_{sub}. The red plot was taken from **Fig. 2-4**(b).

At low T_{sub}, the kinetic mobility of α-NPD molecules at a substrate surface is low, so molecules can move only a short distance and have a difficulty of finding an energetically stable position, leading to smaller ρ_{rel}. In contrast, at high T_{sub}, molecules have a sufficient kinetic mobility (a long enough molecular movement distance) to reach a more stable position, which provides better molecular packing, thereby resulting in higher ρ_{rel}. When T_{sub} was higher than about 0.8 $T_{g,\,bulk}$, ρ_{rel} decreased again. This would be because the excess kinetic mobility makes it difficult to keep molecules at a stable position. Thus, to obtain the highest ρ_{rel}, a substrate needs to be kept at about 0.8 $T_{g,\,bulk}$ during the vacuum deposition of α-NPD films.

Here I discuss an increase of T_{sub} during vacuum deposition. It was reported that the radiant heat from a heated evaporation source does not affect the film morphology when the source temperature during vacuum deposition of α-NPD is around 570 K [18]. The deposited molecules orientate horizontally to obtain an enthalpic gain at the moment of landing, meaning that such a heating effect is sufficiently small not to destruct the film structure and randomize the horizontal orientation. Although there is a possibility that this sort of heating effect increases the actual T_{sub} slightly, its effect on the film structure is assumed to be small. In fact, the T_{sub} is known to be increased by 1−2 ºC from room temperature when α-NPD is vacuum-deposited using a similar deposition system [19].

2-2-2. Electrical properties

I now examine how T_{sub} affects the electrical properties and air stability of α-NPD films considering the variations of S and ρ_{rel}. For this purpose, hole-only devices (HODs) containing an α-NPD layer were fabricated. The structure of the HODs was glass substrate/indium tin oxide (ITO) anode (100 nm)/α-NPD (about 350 nm)/MoO_3 (30 nm)/Au cathode (50 nm). First, glass substrates coated with a 100-nm-thick ITO layer were cleaned using the method mentioned earlier. An α-NPD layer with a thickness of about 350 nm was vacuum-deposited on substrates kept at various T_{sub} under the conditions mentioned earlier. After T_{sub} was returned to room temperature, MoO_3 and Au layers were vacuum-deposited on top of the α-NPD layer to complete the HODs. The active device area was 0.04 cm^2. I used MoO_3/Au as the cathode in the HODs because these layers are expected to be more stable in air than the Al and MgAg cathodes commonly used in OLEDs. Use of MoO_3 with high work function suppressed electron injection in this structure [20,21]. Current density (J)–voltage (V) properties of HODs were measured with a computer-controlled sourcemeter (2400, Keithley) in nitrogen under the dark. I tried to precisely control the α-NPD film thickness at 350 nm using a quartz crystal microbalance installed near a substrate in a vacuum chamber. However, actual thicknesses showed a slight variation among films. Therefore, I used electric field E instead of V to allow better comparison of the film parameters. Here, E was calculated by simply dividing V by the α-NPD film thickness of each HOD measured using a profilometer (DEKTAK XT, Bruker).

Figure 2-6(a) shows the *J*-*E* properties of the HODs. It was clear that the *J*-*E* properties were strongly affected by T_{sub}. Below about 3.0×10^4 V/cm, I observed a bend in the *J*-*E* properties for the HODs except for those with α-NPD layers fabricated at T_{sub} = 314 and 328 K. I attributed this to an increase of carrier trap density, which will be discussed in the next chapter. The *J* values at an *E* of 1.0×10^5 V/cm without the influence of the bend are plotted as a function of T_{sub} in **Fig. 2-6**(b). *J* changes in a similar manner to that of ρ_{rel} in **Fig. 2-4**(b). T_{sub} where the maximum *J* was obtained was 260–290 K (0.72–0.80 $T_{g, bulk}$), which is not far from the results for ρ_{rel} [270–300 K (0.75–0.83 $T_{g, bulk}$)]. A higher ρ_{rel} indicates decreased intermolecular distance because the α-NPD molecules are packed more closely, which might be expected to enhance carrier transport in a film. In contrast, there was no clear relationship between *J* and *S*, even though it has been reported that the horizontal orientation of molecules on a substrate plane leads to enhanced carrier transport because of the better overlap of π orbitals between neighboring molecules in a substrate-normal direction [14]. There is a possibility that the density and orientation are different between films vacuum-deposited on ITO-coated glass substrates and Si substrates even at the same T_{sub} because of different substrate surface roughness [14]. Also, the molecular orientation might be different between the film surface and interior, which can change the energy level [22]. However, the substrate-dependent density and orientation and orientation-dependent energy level did not appear to be major factors here because *J* was strongly related to ρ_{rel} and not *S*. It should be noted that the ρ_{rel} and *S* values estimated by VASE here are the average values of the whole films. From the above results, I conclude that, for α-NPD, the film density has more influence on carrier transport than the molecular orientation does. Even though the ρ_{rel} variation observed here is very small, just 1%–2%, the effect of ρ_{rel} on *J* is considerable, as can be seen in **Fig. 2-6**(b).

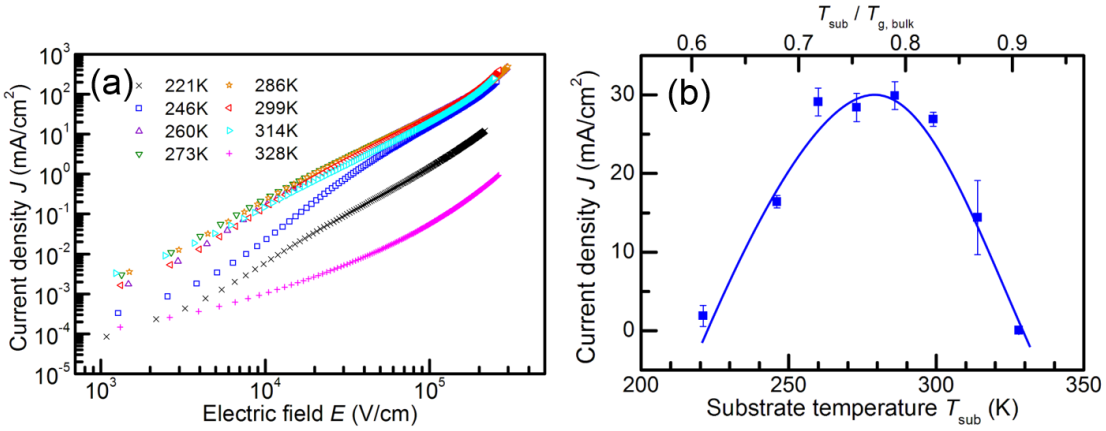

Fig. 2-6. (a) Representative current density (J)–electric field (E) properties of HODs with α-NPD layers vacuum-deposited at different substrate temperatures (T_{sub}) and (b) plot of J at E = 1.0 × 10^5 V/cm versus T_{sub}.

2-2-3. Carrier transport model analysis

To gain insight into the observed increase of *J*, the *J*-*E* properties were analyzed with an injection-limited current (ILC) model, which can be given by [23–25]:

$$J = 4N_0\psi^2 eE exp(-e\phi_B/k_BT)\exp(f^{0.5})\mu(0)\exp(\gamma E^{0.5}), \qquad (2\text{-}5)$$

where N_0 is the density of chargeable sites in an organic film, e is the elementary charge, Φ_B is the injection barrier height, k_B is the Boltzmann constant, T is the temperature, $\mu(0)$ is the zero-field carrier mobility, γ is the Poole–Frenkel factor, f is the reduced electric field ($f = e^3E/4\pi\varepsilon_0\varepsilon_r{k_B}^2T^2$), ε_0 is the vacuum permittivity, ε_r is the relative permittivity, and ψ is a function of f [$\psi = f^{-1} + f^{-0.5} - f^{-1}(1 + 2f^{0.5})^{0.5}$]. Here, N_0 was assumed to be equal to the number density of α-NPD molecules in the films and could be obtained by the following equation:

$$N_0 = \rho_{abs}\rho_{rel}N_A/\rho_{rel,300K}M_w, \qquad (2\text{-}6)$$

where ρ_{abs} is the absolute density of the films deposited at T_{sub} = 300 K (1.19 ± 0.01 g/cm^3) [26], ρ_{rel} is the relative film density, $\rho_{rel,300K}$ is the relative density of the films deposited at T_{sub} = 300 K. The standard ε_r value of 3.0 and T of 300 K were used for the calculation. The work function of ITO was 5.0 eV and the ionization energy of α-NPD was 5.4 eV, both of which were measured by photoelectron yield spectroscopy (AC-3, RikenKeiki). Therefore, Φ_B was estimated to be 0.4 eV. The HODs had a built-in potential (V_{bi}), which is probably defined by the difference between the work functions of ITO and MoO_3 (5.0 and 5.9 eV, both measured by AC-3 spectroscopy). The electric fields of the HODs were calibrated with a V_{bi} value of −0.9 V using the relation: $E_{calibrated} = (V - V_{bi})/d$. Fitting was performed with $\mu(0)$ and γ as variables in the high voltage region, where the influence of the bend seems negligible. The fitting results are shown in **Fig. 2-7**.

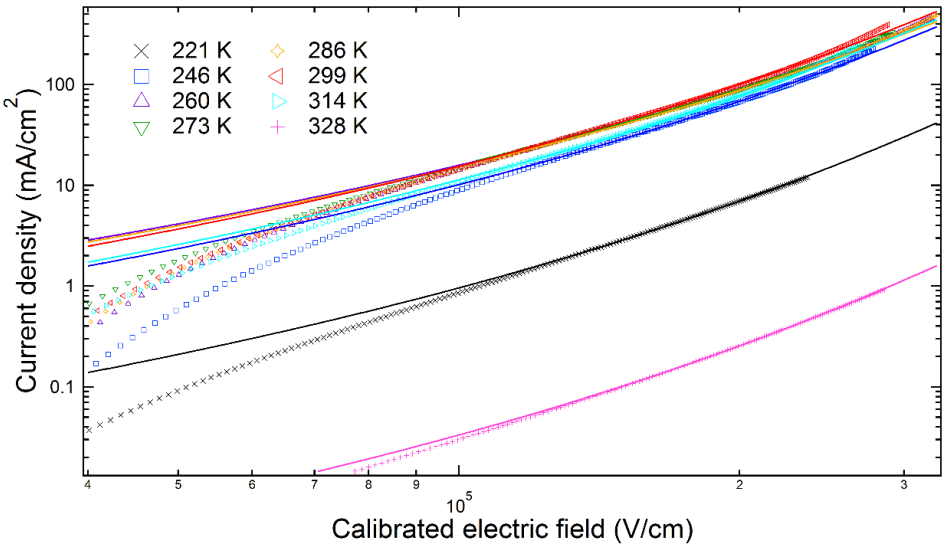

Fig. 2-7. J-$E_{\text{calibrated}}$ properties of HODs with α-NPD layers vacuum-deposited at different substrate temperatures (T_{sub}). Solid lines are the fitting results of the ILC model used to estimate $\mu(0)$ and γ values.

Figure 2-8(a) and (b) show $\mu(0)$ and γ for which the best fitting results were obtained, respectively. The results revealed that the highest $\mu(0)$ and lowest γ appeared at 260–290 K (0.72–0.80 $T_{\text{g, bulk}}$), nearly agreeing with the T_{sub} values where the maximum ρ_{rel} was observed [270–300 K (0.75–0.83 $T_{\text{g, bulk}}$)]. In films with higher density, the distribution of density of states (DOS) of molecules might be expected to be narrower because of the location of molecules at stable positions. This narrowing of DOS distribution can result in a lower barrier between neighboring states near the center of the distribution. The changes of tail states and state-to-state barriers probably led to a decrease of activation energy and enhanced rate of carrier hopping, which could be the origins of the increased $\mu(0)$ and decreased γ.

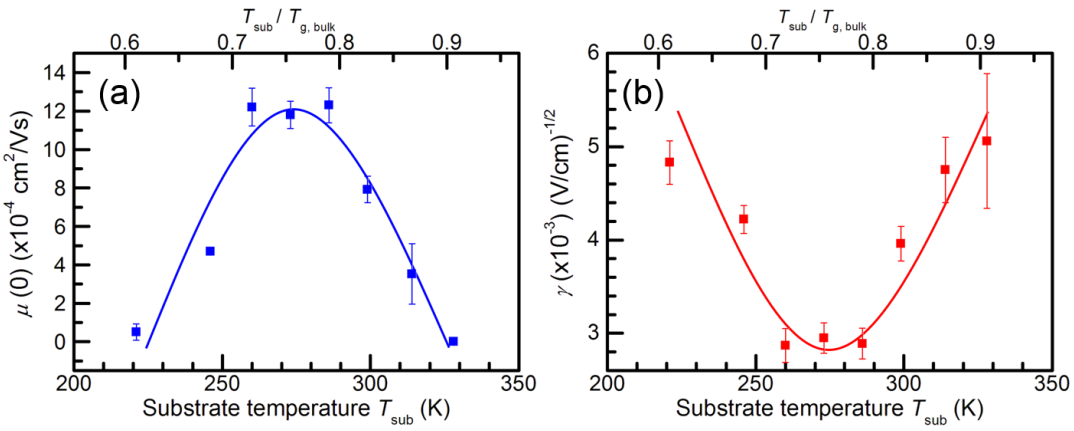

Fig. 2-8. Plots of (a) zero field mobility $\mu(0)$ and (b) Poole–Frenkel factor γ as a function of substrate temperature (T_{sub}) during vacuum deposition. The $\mu(0)$ and γ values were obtained by fitting the *J*-*E* properties in **Fig. 2-6**(a) with **Eq. (2-5)**.

2-2-4. Air stability

After the *J*-*V* measurements, the air stability of HODs was evaluated from the temporal change of driving voltage under continuous current application at 0.1 mA/cm^2 in air (without encapsulation) under the dark using an OLED lifetime measurement system (EAS-26B, System Engineers Co.). The temperature and relative humidity during the stability measurements were around 24 ºC and 50%, respectively.

The temporal changes of driving voltage are exhibited in **Fig. 2-9**(a). To make it easier to compare the temporal *V* changes among different HODs, the initial voltage ($V_{initial}$) at 0 h in **Fig. 2-9**(a) was offset to 0 V by subtracting $V_{initial}$ from *V*. For most of the HODs, $V-V_{initial}$ values increased monotonically over time. HODs with α-NPD vacuum-deposited at the lowest T_{sub} of 221 K showed a unique behavior; $V-V_{initial}$ values decreased during initial device operation and then began to increase rapidly; the reason for this behavior is still unclear and needs to be investigated in future. To quantitatively evaluate the air stability of the HODs from **Fig. 2-9**(a), slopes were calculated by dividing the difference in $V-V_{initial}$ between 0 and 300 h by the elapsed time of 300 h; the results are displayed in **Fig. 2-9**(b). In this figure, a smaller slope means higher air stability. The trend of air stability was a concave function with the minimum value at T_{sub} of around 270–300 K (0.75–0.83 $T_{g,\ bulk}$), consistent with the T_{sub} where the maximum ρ_{rel} was observed [270–300 K (0.75–0.83 $T_{g,\ bulk}$)]. These results reveal that α-NPD films with higher ρ_{rel} have higher air stability, while *S* has no relation to not only the electrical properties but also the air stability of the films. There is a possibility that *S* changes during the stability measurements. However, such a change of *S* should not markedly affect the stability results because carrier transport properties did not depend on *S* for α-NPD, as I discussed earlier.

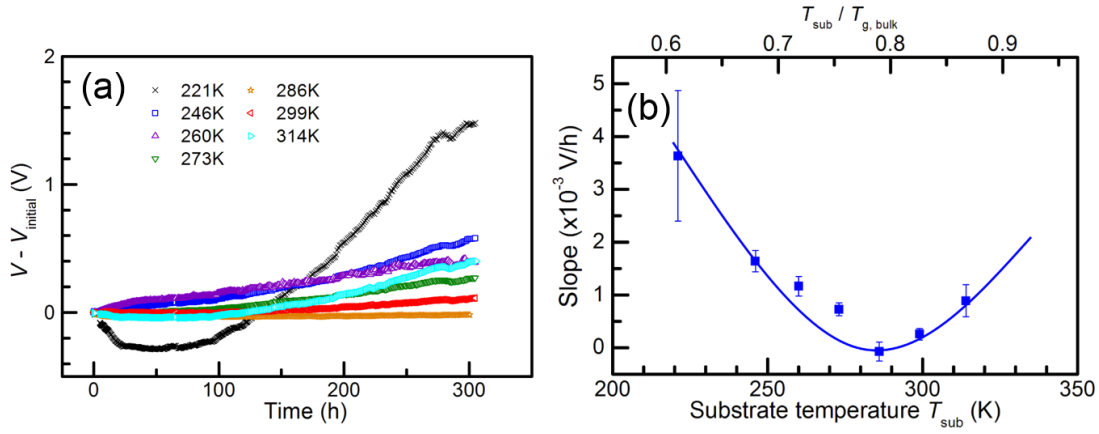

Fig. 2-9. (a) Temporal changes of V for HODs with α-NPD layers vacuum-deposited at different T_{sub}. HODs were operated at a fixed current density of 0.1 mA/cm^2 in air under the dark. The initial V at 0 h was offset to 0 V. (b) Slopes calculated by dividing the difference in V between 0 and 300 h by the elapsed time (300 h).

An increase of V under continuous operation of organic HODs may be caused by several factors, which include (1) degradation of metal electrodes [27], (2) decomposition of organic materials via excited states [28], (3) crystallization of amorphous films [6], and (4) absorption of gas molecules by films [4–8,29]. Factor (1) can be ruled out here because the ITO, Au, and MoO_3 layers should be relatively stable in air and were used in all of the HODs discussed here. Also, factor (2) can be ignored because no excited state is formed by carrier recombination in the fabricated HODs [28]. It is expected that crystallization during device operation is likely suppressed for thermally stable films with high density. Optical microscopy revealed no marked α-NPD crystallization for all the HODs after 300 h of continuous operation. Thus, factor (3) is assumed not to be dominant. The factor (4) is a probable reason for the observed increase in V over time because the inclusion of water and oxygen into organic films accelerates degradation [4–6]. There are several reports describing film density being related to absorption of gas molecules [7,8,29]. Results in some reports [7,8] indicated that densification of organic films led to decreased water uptake, consistent with my present results. Conversely, water uptake decreased when T_{sub} was above room temperature, where the film density is expected to be lower, in another study [29]. Thus, how film density affects absorption of gas molecules (water uptake)

by films is still unclear. Based on my present results, air stability is undoubtedly enhanced with increasing film density. I speculate that the absorption of water and oxygen by the HODs operated in air was suppressed in high-density α-NPD films, and therefore the air stability was improved. The detailed roles of water and oxygen in the device degradation will be clarified in future.

2-3. Conclusion

In this chapter, I investigated the influence of T_{sub} during vacuum deposition of α-NPD films on their molecular orientation, film density, electrical properties, and air stability. I found that the electrical properties and air stability of the α-NPD films were most enhanced at T_{sub} of around 0.8 $T_{g,bulk}$. The reason for the enhanced electrical properties and air stability is mainly because of an increase of the film density at this T_{sub} and not a change of the molecular orientation. However, the aggregation-state change in the amorphous films, accompanied with the densification, is still unclear, and needs to be deeply clarified from a fundamental viewpoint. It is conceivable that there is a uniform decrease of intermolecular distance and that the spatial fluctuation of free volume in the films is lowered. While horizontal orientation is known to be very important to enhance the light outcoupling efficiency of OLEDs [30,31], it did not affect the electrical properties and air stability in this study. If horizontal orientation and high density can be achieved in the same film by controlling the chemical structures of organic materials and T_{sub} during their vacuum deposition, OLEDs with simultaneous higher external quantum efficiency, lower driving voltage, and higher air stability compared with conventional ones will be realized.

References

[1] G. Horowitz, M. E. Hajlaoui, Mobility in polycrystalline oligothiophene field-effect transistors dependent on grain size, *Adv. Mater.* **12**, 1046–1050 (2000).

[2] T. W. Kelley, C. D. Frisbie, Gate voltage dependent resistance of a single organic semiconductor grain boundary, *J. Phys. Chem. B* **105**, 4538–4540 (2001).

[3] S. Seki, Y. Terashima, Y. Kunimi, T. Kawamori, M. Tashiro, Y. Honda, S. Tagawa, The effects of free volumes on charge carrier transport in polysilanes probed by positron annihilation, *Radiat. Phys. Chem.* **68**, 501–505 (2003).

[4] T. Ikeda, H. Murata, Y. Kinoshita, J. Shike, Y. Ikeda, M. Kitano, Enhanced stability of organic light-emitting devices fabricated under ultra-high vacuum condition, *Chem. Phys. Lett.* **426**, 111–114 (2006).

[5] F. Wölzl, I. R. de Moraes, B. Lüssem, S. Hofmann, K. Leo, M. C. Gather, Performance and lifetime of vacuum deposited organic light-emitting diodes: influence of residual gases present during device fabrication, *Org. Electron.* **15**, 3251–3258 (2014).

[6] H. Aziz, Z. Popovic, S. Xie, A.-M. Hor, N.-X. Hu, C. Tripp, G. Xu, Humidity-induced crystallization of tris(8-hydroxyquinoline) aluminum layers in organic light-emitting devices, *Appl. Phys. Lett.* **72**, 756–758 (1998).

[7] K. J. Dawson, K. L. Kearns, M. D. Ediger, M. J. Sacchetti, G. D. Zografi, Highly stable indomethacin glasses resist uptake of water vapor, *J. Phys. Chem. B* **113**, 2422–2427 (2009).

[8] R. Surana, A. Pyne, R. Suryanarayanan, Effect of aging on the physical properties of amorphous trehalose, *Pharm. Res.* **21**, 867–874 (2004).

[9] T. Kato, T. Mori, T. Mizutani, Effect of fabrication conditions on photoluminescence and absorption of hole transport materials, *Thin Solid Films* **393**, 109–113 (2001).

[10] Y. Sakai, M. Shibata, D. Yokoyama, Simple model-free estimation of orientation order parameters of vacuum-deposited and spin-coated amorphous films used in organic light-emitting diodes, *Appl. Phys. Express* **8**, 096601 (2015).

[11] S. S. Dalal, D. M. Walters, I. Lyubimov, J. J. de Pablo, M. D. Ediger, Tunable molecular orientation and elevated thermal stability of vapor-deposited organic semiconductors, *Proc. Natl. Acad. Sci.* **112**, 4227–4232 (2015).

[12] A. Gujral, K. A. O'Hara, M. F. Toney, M. L. Chabinyc, M. D. Ediger, Structural characterization of vapor-deposited glasses of an organic hole transport material with X-ray scattering, *Chem. Mater.* **27**, 3341–3348 (2015).

[13] J. Jiang, D. M. Walters, D. Zhou, M. D. Ediger, Substrate temperature controls molecular orientation in two-component vapor-deposited glasses, *Soft Matter* **12**, 3265–3270 (2016).

[14] D. Yokoyama, Y. Setoguchi, A. Sakaguchi, M. Suzuki, C. Adachi, Orientation control of linear-shaped molecules in vacuum-deposited organic amorphous films and its effect on carrier mobilities, *Adv. Funct. Mater.* **20**, 386–391 (2010).

[15] H.-W. Lin, C.-L. Lin, H.-H. Chang, Y.-T. Lin, C.-C. Wu, Y.-M. Chen, R.-T. Chen, Y.-Y. Chien, K.-T. Wong, Anisotropic optical properties and molecular orientation in vacuum-deposited ter(9,9-diarylfluorene)s thin films using spectroscopic ellipsometry, *J. Appl. Phys.* **95**, 881–886 (2004).

[16] D. Yokoyama, Molecular orientation in small-molecule organic light-emitting diodes, *J. Mater. Chem.* **21**, 19187–19202 (2011).

[17] M. Shibata, Y. Sakai, D. Yokoyama, Advantages and disadvantages of vacuum-deposited and spin-coated amorphous organic semiconductor films for organic light-emitting diodes, *J. Mater. Chem. C* **3**, 11178–11191 (2015).

[18] T. Kato, T. Mori, T. Mizutani, Polarizing microscope observation for thin film of hole transport material -Effect of evaporation temperature and deposition rate-, *T. IEE Japan* **121-A**, 672–676 (2001) [in Japanese].

[19] T. Matsushima, K. Shiomura, S. Naka, H. Murata, Optical, morphological, structural, electrical, molecular orientation, and electroluminescence characteristics of organic semiconductor films prepared at various deposition rates, *Thin Solid Films* **520**, 2283–2288 (2012).

[20] M. Kröger, S. Hamwi, J. Meyer, T. Riedl, W. Kowalsky, A. Kahn, P-type doping of organic wide band gap materials by transition metal oxides: a case-study on molybdenum trioxide, *Org. Electron.* **10**, 932–938 (2009).

[21] J. Meyer, S. Hamwi, M. Kröger, W. Kowalsky, T. Riedl, A. Kahn, Transition metal oxides for organic electronics: energetics, device physics and applications, *Adv. Mater.* **24**, 5408–5427 (2012).

[22] W. Chen, W. H. Huang, S. Chen, Y. L. Huang, X. Y. Gao, A. T. S. Wee, Molecular orientation-dependent ionization potential of organic thin films, *Chem. Mater.* **20**, 7017–7021 (2008).

[23] J. C. Scott, G. G. Malliaras, Charge injection and recombination at the metal–organic interface, *Chem. Phys. Lett.* **299**, 115–119 (1999).

[24] Z. B. Wang, M. G. Helander, M. T. Greiner, J. Qiu, Z. H. Lu, Analysis of charge-injection characteristics at electrode-organic interfaces: case study of transition-metal oxides, *Phys. Rev. B* **80**, 235325 (2009).

[25] Z. B. Wang, M. G. Helander, M. T. Greiner, J. Qiu, Z. H. Lu, Carrier mobility of organic semiconductors based on current-voltage characteristics, *J. Appl. Phys.* **107**, 034506 (2010).

[26] H.-F. Xiang, Z.-X. Xu, V. A. L. Roy, C.-M. Che, P. T. Lai, Method for measurement of the density of thin films of small organic molecules, *Rev. Sci. Instrum.* **78**, 034104 (2007).

[27] Y.-F. Liew, H. Aziz, N.-X. Hu, H. S.-O. Chan, G. Xu, Z. Popovic, Investigation of the sites of dark spots in organic light-emitting devices, *Appl. Phys. Lett.* **77**, 2650–2652 (2000).

[28] D. Y. Kondakov, Role of chemical reactions of arylamine hole transport materials in operational degradation of organic light-emitting diodes, *J. Appl. Phys.* **104**, 084520 (2008).

[29] J. M. Torres, N. Bakken, J. Li, B. D. Vogt, Substrate temperature to control moduli and water uptake in thin films of vapor deposited *N*,*N*'-di(1-naphthyl)-*N*,*N*'-diphenyl-(1,1'-biphenyl)-4,4'-diamine (NPD), *J. Phys. Chem. B* **119**, 11928–11934 (2015).

[30] W. Brütting, J. Frischeisen, T. D. Schmidt, B. J. Scholz, C. Mayr, Device efficiency of organic light-emitting diodes: progress by improved light outcoupling, *Phys. Stat. Sol. A* **210**, 44–65 (2013).

[31] T. Komino, H. Tanaka, C. Adachi, Selectively controlled orientational order in linear-shaped thermally activated delayed fluorescent dopants, *Chem. Mater.* **26**, 3665–3671 (2014).

Chapter 3

Discussion on hole traps of amorphous films of α-NPD deposited at different substrate temperatures

Y. Esaki, T. Matsushima, and C. Adachi
Applied Physics Letters **114**, 173301 (2019).

3-1. Introduction

As I discussed in Chapter 2, I found that the hole current and air stability of amorphous films of α-NPD were the highest when T_{sub} during vacuum deposition was about 275 K [1]. This enhanced hole current was attributed to the decreased molecular distance and narrowing of DOS distribution in higher-density films deposited at this T_{sub}. However, there was a possibility that other factors also affected the electrical properties. In this chapter, I discuss the thermally stimulated currents (TSCs) of α-NPD films deposited at various T_{sub}. TSC measurements have been used to estimate the density and depth of carrier traps in inorganic, polymer, and small-molecule organic materials [2,3]. Analysis of the TSC results reveals that hole traps exist in bulk films and are the shallowest when films are deposited at the optimized T_{sub} of around 275 K.

3-2. Results and discussion

3-2-1. Current enhancement in high-density films

For measurements of electrical properties and TSCs, I first fabricated HODs with the same structure used in Chapter 2. However, the obtained TSC signals were too noisy, probably due to small leakage currents caused by diffusion of Au atoms into α-NPD. Therefore, I replaced the Au cathode with Al for reliable TSC measurements. The new HOD structure was glass substrate/ITO anode (100 nm)/α-NPD (300 nm)/MoO_3 (30 nm)/Al cathode (50 nm). α-NPD was deposited on the substrate kept at various T_{sub} ranging from 240 to 330 K to form a film with a thickness of 300 nm. After α-NPD deposition, T_{sub} was returned to room temperature and then MoO_3 (30 nm) and Al cathode (50 nm) layers were vacuum-deposited on the α-NPD layer. After the *J-E* properties were obtained, HODs were encapsulated using a glass cap and UV curing epoxy resin in the nitrogen-filled glove box to avoid degradation of the films in air during TSC measurements. The detailed conditions of the vacuum deposition and the *J-E* measurement were the same as those in Chapter 2.

I first confirmed whether the current enhancement was correctly reproduced in the new HODs. *J*-*E* properties of the new HODs fabricated with different T_{sub} are shown in **Fig. 3-1**(a). *J* values taken from these curves at an *E* of 5.0 × 10^4, 1.0 × 10^5, and 1.5 × 10^5 V/cm are plotted versus T_{sub} in **Fig. 3-1**(b–d). At every *E*, *J* values strongly depended on T_{sub} and were the highest at a T_{sub} of around 275 K (~0.75 $T_{g,bulk}$), consistent with the result obtained in Chapter 2 [1].

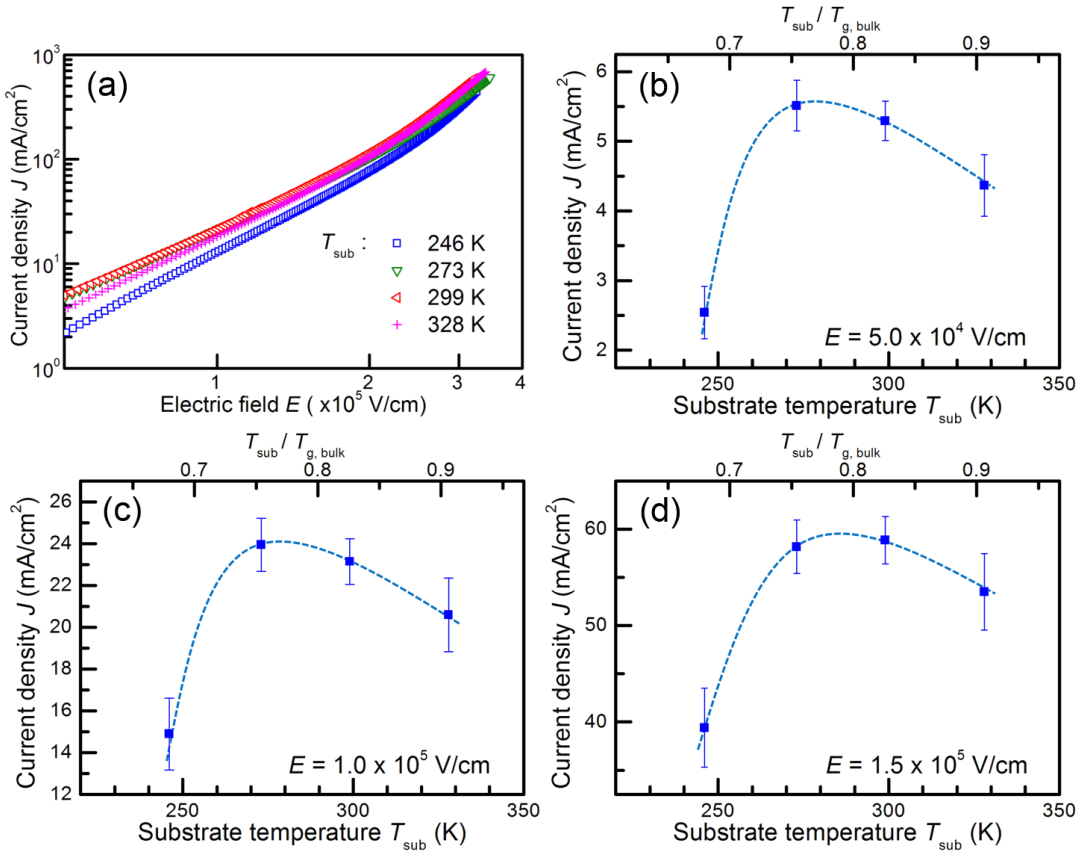

Fig. 3-1. (a) Representative current density (*J*)–electric field (*E*) curves of HODs fabricated at various substrate temperatures (T_{sub}) during vacuum deposition. (b–d) Plots of *J* values at an *E* of (b) 5.0 × 10^4, (c) 1.0 × 10^5, and (d) 1.5 × 10^5 V/cm as a function of T_{sub} for HODs fabricated at T_{sub} = 246, 273, 299, and 328 K. The dashed lines are guides to the eye.

3-2-2. Theory of thermally stimulated current originating from bulk traps [2–5]

Here a TSC measurement method is overviewed. The HOD is biased at low temperature to fill hole traps with injected holes. After trap filling, the HOD is heated at a certain heating rate (β) under a collecting voltage (V_c). The holes are released by thermal activation during heating. When trapped holes exist in the bulk film, the same amount of negative charge is induced on the electrodes. The released holes drift to the electrode(s) along the electric potential, resulting in the gradual change of the amount of induced negative charge on each electrode, which is detected as a TSC. (See **Fig. 3-5** for actual TSC curves.)

Figure 3-2(a) illustrates a dielectric film sandwiched with two electrodes denoted as electrode 1 and 2. The film thickness is d and hole traps are dispersed homogeneously throughout the film. The horizontal axis shows the distance from electrode 1. The vertical axis is the electric potential. Trapped holes form a concave-shaped potential with a minimum at position x_m, as described with Poisson's equation. The amounts of negative charge induced on electrode 1 (Q_1) and 2 (Q_2) are written as:

$$Q_1 = \frac{d - x_{av}}{d} Q_{tot} \qquad (3\text{-}1) \qquad \text{and}$$

$$Q_2 = \frac{x_{av}}{d} Q_{tot}, \qquad (3\text{-}2)$$

where x_{av} is the average distance of the trapped holes and Q_{tot} is the total amount of induced charge on electrodes, which is equal to the total amount of trapped charges ($Q_{tot} = Q_1 + Q_2$). Here, x_{av}/d is equal to Q_2/Q_{tot}. When the temperature is increased, thermally activated holes drift along the electric potential. As a result, the holes activated at $0 < x < x_m$ move toward electrode 1 and the other holes activated at $x_m < x < d$ drift toward electrode 2. These conditions are inappropriate to estimate carrier trap density because positive and negative TSC signals coexist or cancel out each other (an example is shown in **Fig. 3-3**). Application of higher V_c is known to suppress this effect. **Figure 3-2**(b) shows the electric potential under $V_c = V_{sat}$, where the saturation voltage (V_{sat}) satisfies the following relationship:

$$V_{sat} = \frac{Q_2}{C} = \frac{1}{C} \frac{x_{ave}}{d} Q_{tot}, \qquad (3\text{-}3)$$

where C is the capacitance of the dielectric film. Under this saturated condition, all the induced charge on electrode 2 move toward electrode 1, meaning $Q_{1,sat} = -Q_{tot}$ and $Q_{2,sat} = 0$. Now, the electric potential is a monotonic slope ($x_m = d$) and all of the thermally activated holes drift to electrode 1. After the

drift of all of the trapped holes [**Fig. 3-2**(c)], the linear electric potential formed by V_{sat} is left, where $Q_{1,final} = -\frac{x_{av}}{d}Q_{tot} = -Q_2$ and $Q_{2,final} = \frac{x_{av}}{d}Q_{tot} = Q_2$. The detected TSC is a result of the move of induced charge during the drift of activated holes, corresponding to Q_2 in this case. Conversely, when the bias direction of V_c is reversed and $V_{sat} = -\frac{Q_1}{C} = -\frac{1}{C}\frac{d-x_{av}}{d}Q_{tot}$ is applied, TSC corresponding to Q_1 is detected. Therefore, when the bulk traps exist in the dielectric film, one should measure TSC curves at positive and negative V_c and add up Q_1 and Q_2 to obtain Q_{tot}. The coexistence of positive and negative TSC signals at small V_c is indicative of carrier traps in bulk films and not at the interfaces.

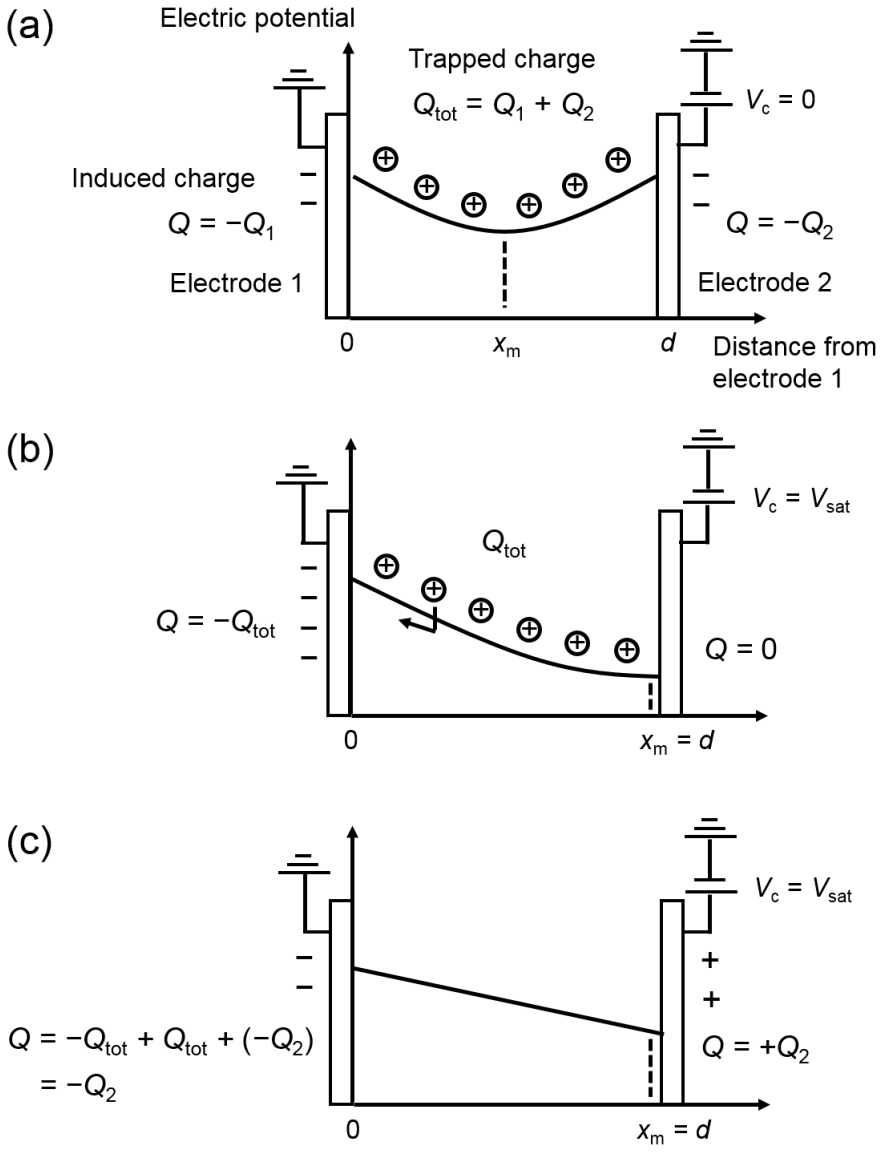

Fig. 3-2. Schematics of electric potentials for an HOD during a TSC measurement. Trap-filled conditions before the temperature increase at V_c = (a) 0 V and (b) V_{sat} and (c) conditions after complete carrier releasing by a temperature increase at $V_c = V_{sat}$.

3-2-3. Thermally stimulated current and its origin

TSC curves were measured using a dedicated measurement system (TS-FETT, Rigaku). An HOD was connected to the system with gold wires and silver paste. The electrical bias where holes were injected from ITO anode and extracted to Al cathode was termed “forward” bias. Here, the forward and reverse bias corresponded to the negative and positive values of applied voltages, respectively. The HOD was cooled with liquid nitrogen to 81 K and biased at a trap-filling voltage (V_{fill}) for 30 s. To ensure sufficient trap filling, I used a V_{fill} that induced a current flow of 1 mA/cm^2 through the HOD at low temperature. Then, the temperature of the HOD was gradually increased toward 170 K at a certain β using a heater under a negative or positive V_c. After this measurement, the same measurement was carried out without trap filling (V_{fill} = 0 V). β was fixed at 0.046±0.003 K/s for TSC measurements with different V_c. Additionally, V_c was fixed at 1.0 or –1.0 V (except for –1.4 V for the HOD fabricated at T_{sub} = 246 K) for TSC measurements with different β. Actual TSC curves were obtained by simply subtracting a curve measured without trap filling from that measured with trap filling. Because the subtraction was frequently unsuccessful in the high temperature region where injected current exists, TSC curves in these regions were cut off. The β values were estimated from the slope of a plot of temperature versus time for each measurement.

When V_c was small, the coexistence of positive and negative signals in a TSC profile was observed as shown in **Fig. 3-3**, being consistent with the aforementioned theory that some of the released holes drift to one electrode and other released holes drift to the opposite electrode along with a concave-shaped electric potential. Thus, it can be concluded that the origin of the observed TSC is hole traps in the bulk film rather than at the interfaces. Increasing V_c is effective for obtaining an electric potential with a monotonic slope, where all of the released holes drift to one electrode, leading to the appearance of only positive or negative signals in TSC profiles. **Figures 3-4** and **3-5** present current and TSC curves measured with various V_c for HODs fabricated at various T_{sub}. When V_c was −1.4 to −2.0 V [**Fig. 3-5**(a)], negative signals completely disappeared and only positive signals were obtained, meaning that the applied V_c was sufficiently large to move the released holes to one electrode. Conversely, when V_c was 0.8 to 1.4 V [**Fig. 3-5**(b)], positive signals completely disappeared and only negative signals were obtained. A slight peak shift observed at high V_c for both signals was because of the lowering of the energy barrier, which is discussed later. Similar behavior was observed in TSC curves of all HODs fabricated here [**Fig. 3-5**(c−h)].

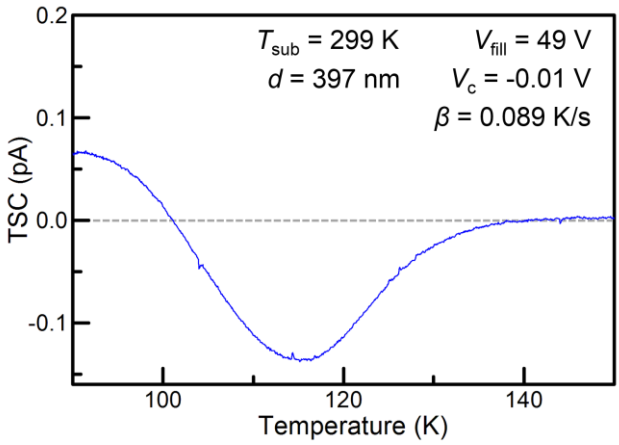

Fig. 3-3. A TSC curve of a representative HOD fabricated at T_{sub} = 299 K measured with a small V_c of –0.01 V. This curve had a positive signal at ~90 K and negative signal at ~115 K.

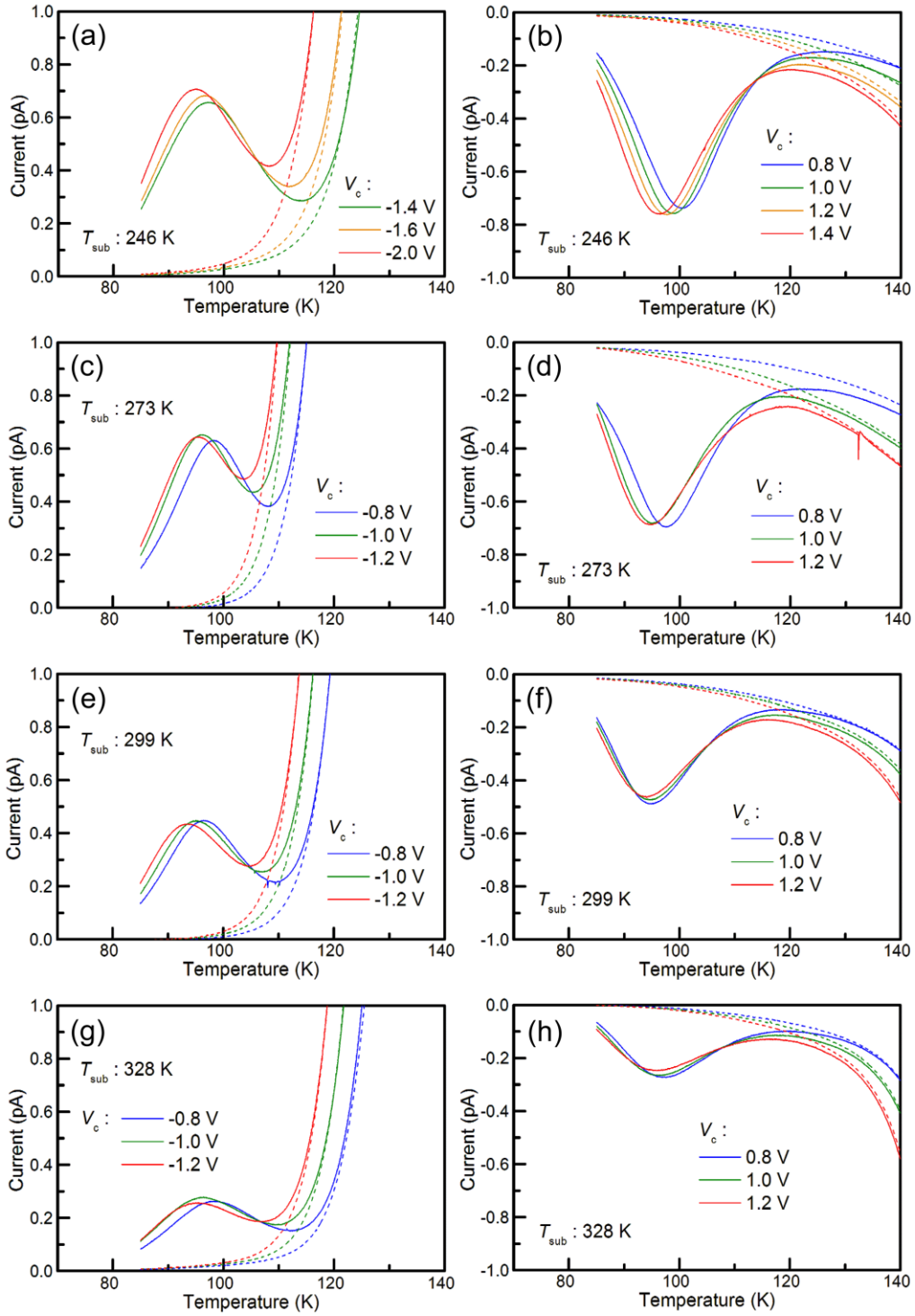

Fig. 3-4. Current curves of HODs fabricated at various T_{sub} when the collecting voltages (V_c) were (a, c, e, g) negative and (b, d, f, h) positive. The solid and dashed lines represent measurement results with and without trap filling, respectively.

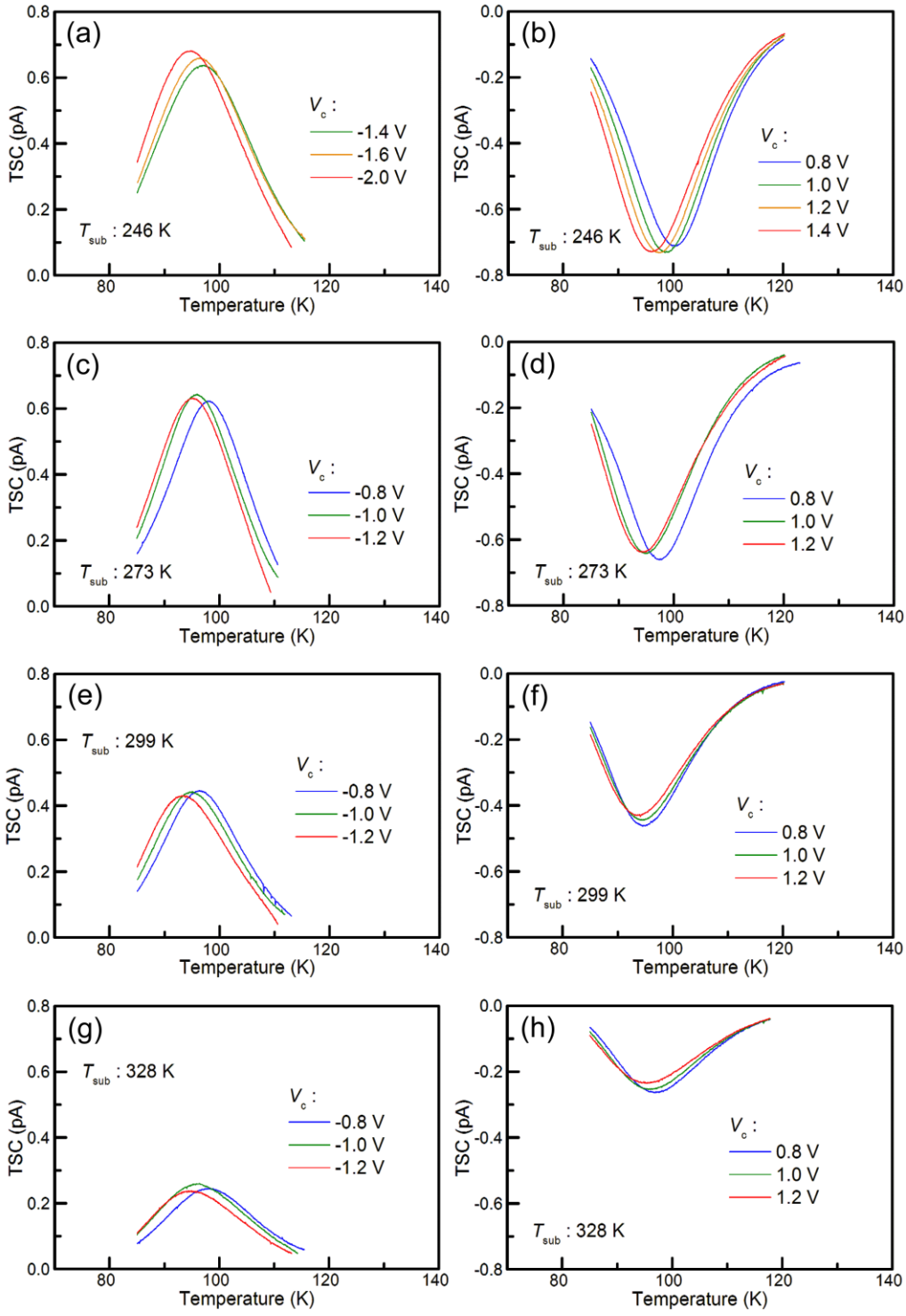

Fig. 3-5. TSC curves of HODs fabricated at various T_{sub} when the collecting voltages (V_c) were (a, c, e, g) negative and (b, d, f, h) positive. These TSC curves were obtained from **Fig. 3-4** by subtracting the measurement result without trap filling from that with trap filling.

3-2-4. Estimation of trap density

All TSC curves lacked signals below 85 K and over 115 K because 85 K was the lower limit of temperature for my TSC system and current injection from an electrode was non-negligible above 115 K. To compensate the lack of signals, I fitted the TSC curves with a pseudo-Voigt function considering asymmetry, which is written as [6–9]:

$$F(x) = \frac{I_0}{\left\{1+\frac{4M\frac{(x-x_0)}{\{1+\alpha(x-x_0)/\Gamma\}}}{\Gamma^2}\right\}\exp\left\{(1-M)4\frac{\ln(2)\left(\frac{(x-x_0)}{\{1+\alpha(x-x_0)/\Gamma\}}\right)^2}{\Gamma^2}\right\}}, \qquad (3\text{-}4)$$

where I_0 is the peak height, Γ is the parameter for the peak width, x_0 is the peak position, M is the mixing ratio of Lorentzian and Gaussian functions, and α is the asymmetric parameter. All TSC curves could be well fitted with this function. Representative fitting results are shown in **Fig. 3-6**.

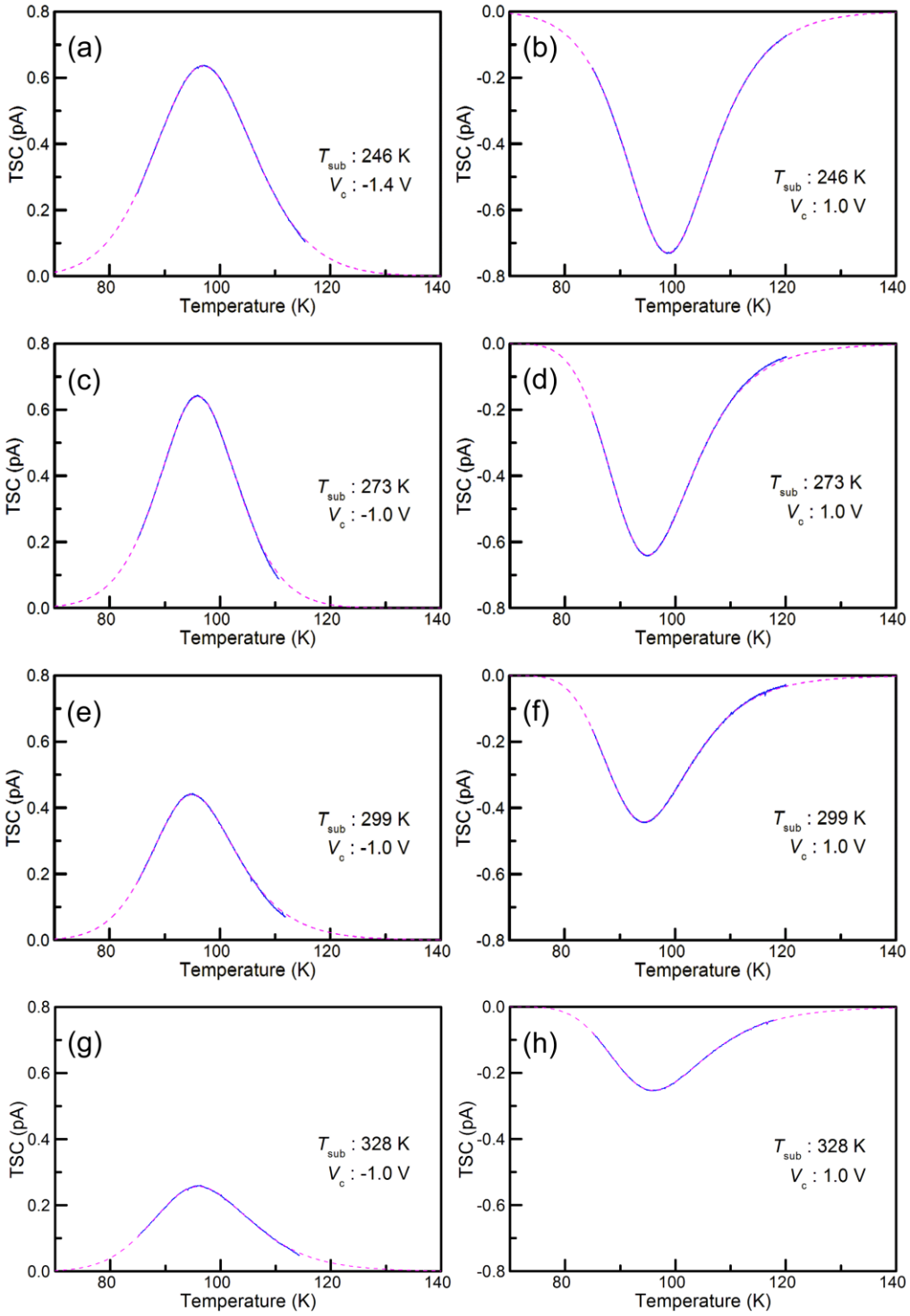

Fig. 3-6. Representative fitting results of TSC curves with a pseudo-Voigt function considering asymmetry. The blue solid and pink dashed lines are the experimental and fitting results, respectively.

The amount of charge Q was calculated by dividing an area of a fitting curve by β. I plotted Q values as a function of V_c for each HOD fabricated at various T_{sub} [**Fig. 3-7**(a)]. Plots of Q versus collecting field E_c are shown in **Fig. 3-8**. The positive Q_1 and negative Q_2 values in this figure were obtained from TSC curves measured under negative and positive V_c, respectively. Q_1 and Q_2 were independent of V_c as shown in **Fig. 3-7**(a), indicating the saturated measurement conditions at these V_c. The sum of Q_1 and Q_2 is equal to the total amount of charges Q_{tot}, which corresponds to the amount of trapped holes in the films. Calculated values of x_{av}/d were about 0.5 for all HODs as shown in **Fig. 3-9**. This means that the hole traps homogeneously exist throughout the α-NPD films. The hole trap density N_t was calculated by:

$$N_t = Q_{tot}/eSd, \qquad (3\text{-}5)$$

where e is the elementary charge and S is the active device area. **Figure 3-7**(b) displays the relationship between N_t and T_{sub}. N_t decreased monotonically as T_{sub} increased.

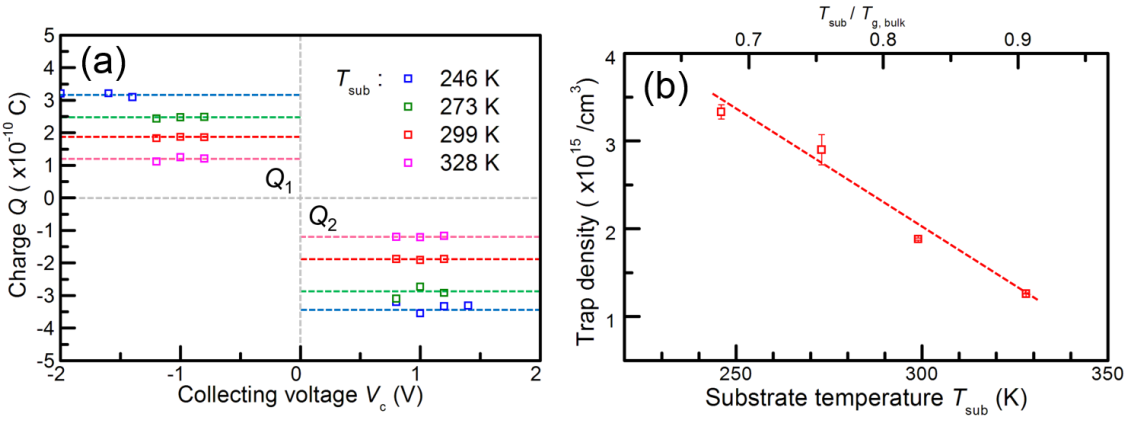

Fig. 3-7. (a) Relationship between the amounts of charge estimated from positive and negative signals in TSC curves (Q_1 and Q_2, respectively) and collecting voltage (V_c) for HODs fabricated at various T_{sub} and (b) T_{sub} dependence of hole trap density calculated from the total amount of charge (Q_{tot}). The dashed lines are guides to the eye.

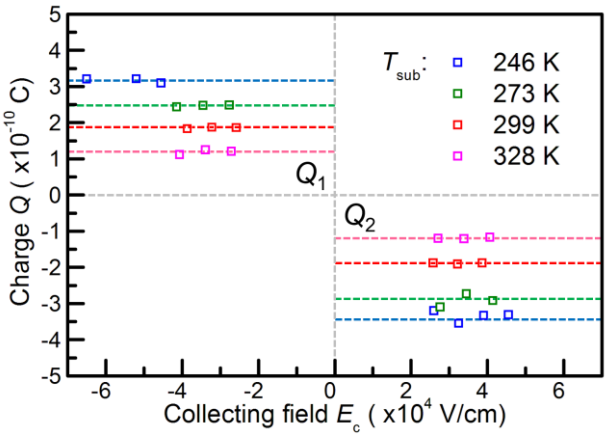

Fig. 3-8. Relationship between the amounts of charge estimated from positive and negative signals in TSC curves (Q_1 and Q_2, respectively) and collecting field (E_c) for HODs fabricated at various T_{sub}. E_c was calculated by dividing V_c with α-NPD film thickness. The dashed lines are guides to the eye.

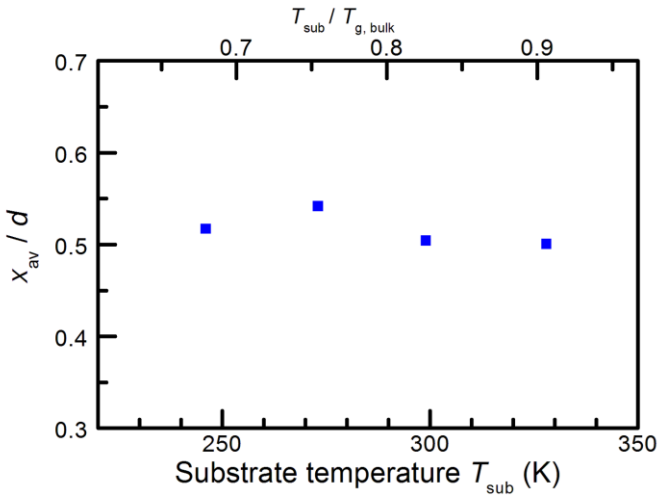

Fig. 3-9. Plot of x_{av}/d values as a function of T_{sub} for HODs fabricated at various T_{sub}.

3-2-5. Estimation of trap depth

To estimate the hole trap depth d_t, I used the following equation considering the relationship between β and the temperature at a TSC peak T_m[3−5,10]:

$$\frac{d_t}{kT_m} = \ln\left(\frac{{T_m}^2}{\beta}\right) + \ln\left(\frac{k_B}{\tau_0 d_t}\right), \qquad (3\text{-}6)$$

where k_B is the Boltzmann constant and τ_0 is a constant. I measured TSC curves under the saturated V_c conditions with different β ranging from 0.04 to 0.16 K/s. The β dependence of current and TSC curves for HODs fabricated with various T_{sub} is shown in **Fig. 3-10** and **3-11**. T_m shifted to higher temperature as β increased because of the delay of carrier releasing.

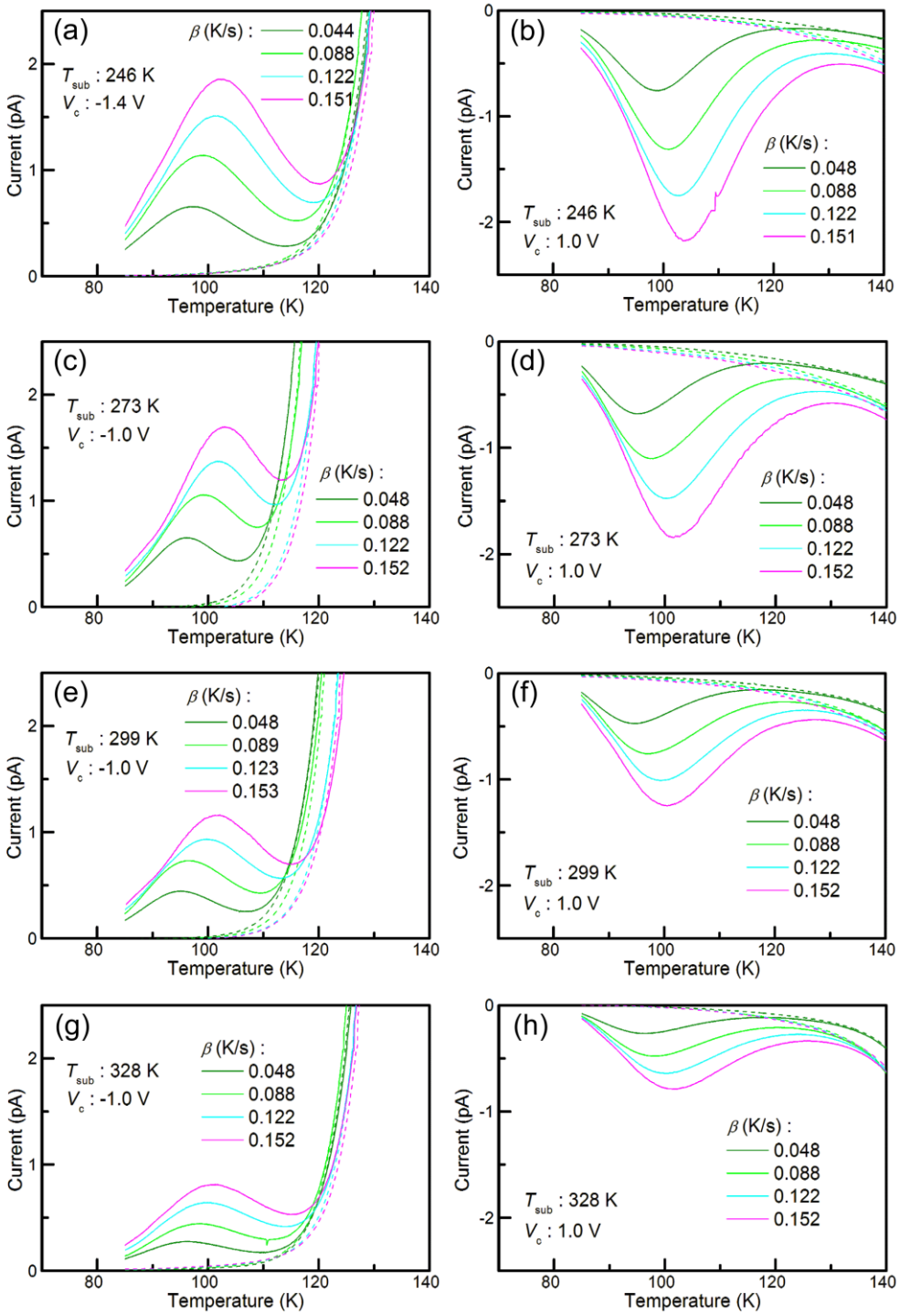

Fig. 3-10. Current curves of HODs fabricated at various T_{sub} and measured with different heating rates (β) and (a, c, e, g) negative and (b, d, f, h) positive collecting voltages (V_c). The solid and dashed lines are measurement results with and without trap filling, respectively.

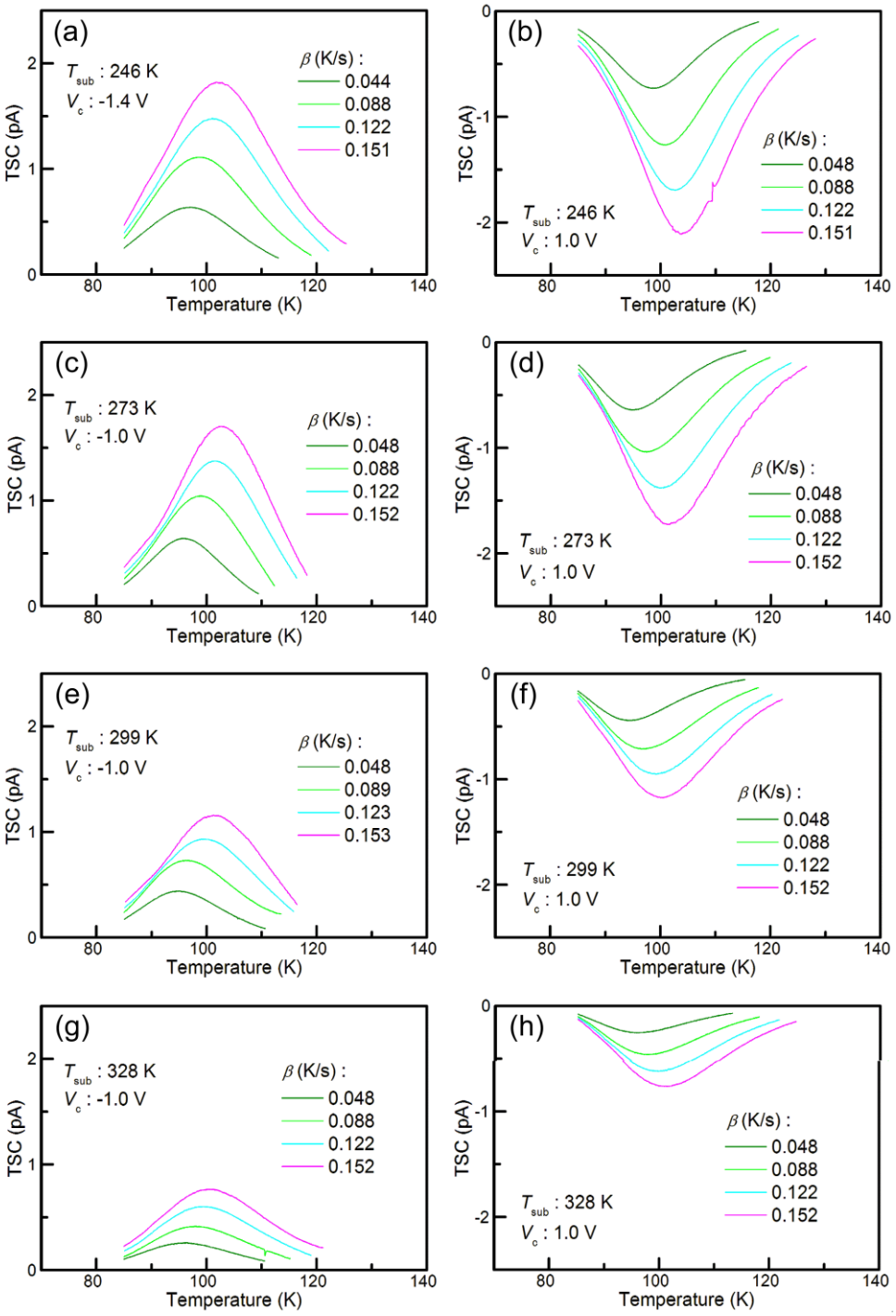

Fig. 3-11. TSC curves of HODs fabricated at various T_{sub} and measured with different heating rates (β) and (a, c, e, g) negative and (b, d, f, h) positive collecting voltages (V_c). These TSC curves were obtained from **Fig. 3-10** by subtracting the measurement result without trap filling from that with trap filling.

I performed a linear fitting of $\ln(T_m^2/\beta)$ versus $1/T_m$ plots to calculate d_t (**Fig. 3-12**). These d_t values need to be calibrated to estimate the true trap depth because they include the influence of energy barrier lowering induced by the external electric field formed by V_c. The calibration was performed considering the Poole–Frenkel effect. Assuming that a Coulomb potential is formed by the trapped carriers, the barrier lowering $\Delta\Phi$ induced by V_c can be written as [11,12]:

$$\Delta\Phi = \sqrt{\frac{e^3 E_c}{4\pi\varepsilon_0\varepsilon_r}}, \qquad (3\text{-}7)$$

where E_c is the collecting field (obtained by dividing V_c by d), ε_0 is the permittivity in vacuum, and ε_r is the relative permittivity (3.0). The calibrated trap depth ($d_{t,cal}$) was obtained by adding the calculated $\Delta\Phi$ to the experimentally determined trap depth (d_t) (**Table 3-1**).

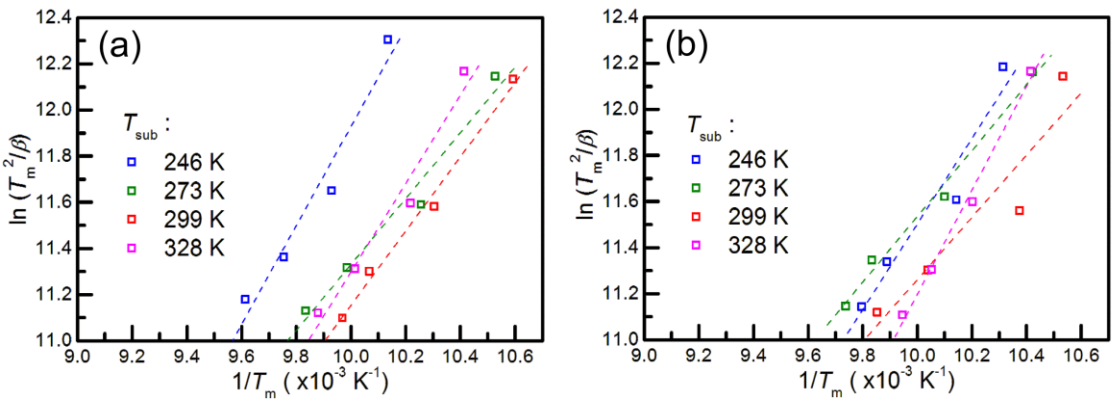

Fig. 3-12. Plots of ln (T_m^2/β) versus $1/T_m$ obtained from (a) positive and (b) negative TSC signals. The plots are fitted with a least-square method (dashed lines).

Table 3-1. Summary of d_t, $\Delta\Phi$, and $d_{t,cal}$ values for HODs fabricated at various T_{sub}.

T_{sub} (K)	V_c (V)	d_t (eV)	$\Delta\Phi$ (eV)	$d_{t,cal}$ (eV)
246	–1.4	0.160	0.047	0.207
	1.0	0.185	0.040	0.224
273	–1.0	0.123	0.041	0.164
	1.0	0.123	0.041	0.164
299	–1.0	0.116	0.039	0.156
	1.0	0.139	0.039	0.178
328	–1.0	0.195	0.040	0.235
	1.0	0.165	0.040	0.205

The calibrated trap depth ($d_{t,cal}$) is plotted against T_{sub} in **Fig. 3-13**. The $d_{t,cal}$ values showed a concave-shaped trend against T_{sub}, with the minimum $d_{t,cal}$ at a T_{sub} of around 275 K (~0.75$T_{g,bulk}$). I performed photoelectron spectroscopy (AC-3, RIKEN KEIKI) to estimate ionization energies (hole transport levels) of α-NPD films deposited at T_{sub} = 246 and 299 K. Although these films have different current densities and hole trap depths, the estimated ionization energies seem similar (**Fig. 3-14**).

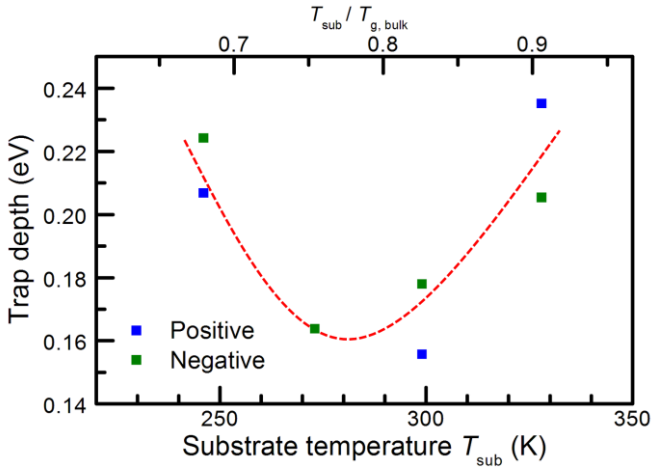

Fig. 3-13. T_{sub} dependence of calibrated trap depth $d_{t.cal}$ estimated from positive and negative TSC signals. The dashed line is a guide to the eye.

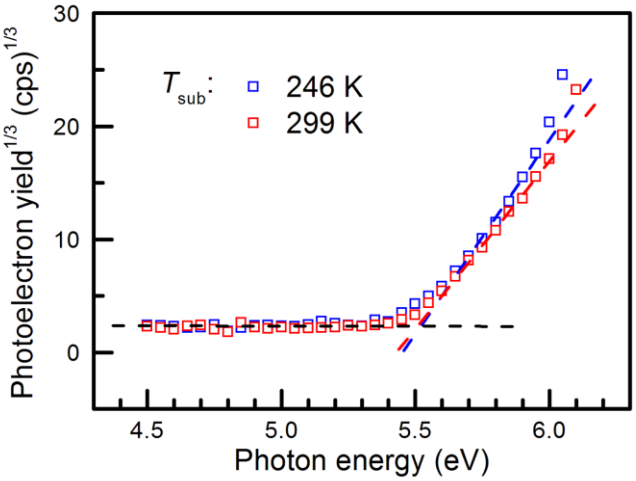

Fig. 3-14. Plots of cubic root of photoelectron yield versus photon energy for α-NPD films deposited on ITO at T_{sub} = 246 and 299 K. The ionization energies estimated from the photoelectron onsets were ~5.5 eV for both films.

3-2-6. Discussion

As reasons for the enhanced current density [**Fig. 3-1**], better carrier hopping between neighboring molecules and narrowing of DOS distribution in higher-density films are possible as I discussed in Chapter 2. Another reason could be the smaller hole trap depth shown in **Fig. 3-13**. However, there is no clear interplay between the current density and the hole trap density [**Fig. 3-7**(b)]. Perhaps, the better carrier hopping and the smaller hole trap depth more strongly affect the current density than the change of hole trap density does. Further, it is possible that there are other unknown parameters which modulate the current density.

Many types of impurities exist in vacuum-deposited films, such as water, oxygen, and other materials deposited previously in the vacuum chamber [13−16]. In addition, impurities generated by thermal decomposition in a heated deposition source are included in vacuum-deposited films, and the amount of impurities is assumed to be larger in films fabricated at lower T_{sub}, which will be discussed in next Chapter 4 [17]. In contrast, vacuum-deposited amorphous films intrinsically contain molecular disorder, which impedes carrier transport. Molecular disorder is likely minimized for α-NPD films deposited at a T_{sub} of around 275 K because they have the highest film density and thermal stability with better molecular packing [1]. Impurities and molecular disorder are expected to behave as hole traps in α-NPD films discussed here. However, the true origin of the hole traps is still unclear and should be investigated in future.

3-3. Conclusion

In summary, to investigate the reason why the maximum hole current was obtained when α-NPD films were vacuum-deposited at a T_{sub} of around 275 K, hole traps were estimated by analyzing TSCs. The obtained TSC results indicated the homogeneous distribution of hole traps in bulk α-NPD films. While the trap density decreased monotonically as T_{sub} increased, the trap depth displayed a concave-shaped trend, with the minimum value at a T_{sub} of around 275 K. The hole current was higher at T_{sub} where the trap depth was shallower. In Chapter 2, I attributed the current enhancement to the decreased molecular distance and narrowing of DOS distribution in high-density α-NPD films [1]. In this chapter, I found that the change of the carrier traps by T_{sub} is an additional possible origin of the current enhancement.

References

[1] Y. Esaki, T. Komino, T. Matsushima, C. Adachi, Enhanced electrical properties and air stability of amorphous organic thin films by engineering film density, *J. Phys. Chem. Lett.* **8**, 5891–5897 (2017).

[2] T. Hino, Thermally stimulated characteristics in solid dielectrics, *IEEE Trans. Electr. Insul.* **EI-15**, 301–311 (1980).

[3] M. Iwamoto, D. Taguchi, Research trend in thermally stimulated current method for development of materials and devices in Japan, *Jpn. J. Appl. Phys.* **57**, 03EA04 (2018).

[4] 日野 太郎, 熱刺激電流(TSC)の測定と応用, 電気学会雑誌 **95**, 109–116 (1975) [in Japanese].

[5] 岩本 光正, 田口 大, 熱刺激電流による電気電子材料評価 –基礎と応用–, コロナ社 (2014) [in Japanese].

[6] R. O. Ansell, T. Dickinson, A. F. Povey, P. M. A. Sherwood, X-ray photoelectron spectroscopic studies of electrode surfaces using a new controlled transfer technique. Part II. Results for a molybdenum electrode and the curve fitting procedure, *J. Electroanal. Chem.* **98**, 79–89 (1979).

[7] H. Darmstadt, D. Pantea, L. Sümmchen, U. Roland, S. Kaliaguine, C. Roy, Surface and bulk chemistry of charcoal obtained by vacuum pyrolysis of bark: influence of feedstock moisture content, *J. Anal. Appl. Pyrolysis* **53**, 1–17 (2000).

[8] I. Kojima, N. Fukumoto, M. Kurahashi, Analysis of X-ray photoelectron spectrum with asymmetric Gaussian-Lorentzian mixed function, *J. Jpn. Soc. Anal. Chem.* (分析化学) **35**, T96–T100 (1986) [in Japanese].

[9] S. Maenosono, J. D. Lee, A. T. N. Dao, D. Mott, Peak shape analysis of Ag 3d core-level X-ray photoelectron spectra of Au@Ag core-shell nanoparticles using an asymmetric Gaussian–Lorentzian mixed function, *Surf. Interface Anal.* **44**, 1611–1614 (2012).

[10] R. Chen, On the analysis of thermally stimulated processes, *J. Electrostat.* **3**, 15–24 (1977).

[11] M. R. Boon, Anomalous value of Poole–Frenkel coefficient, *Thin Solid Films* **8**, R5–R6 (1971).

[12] M. R. Boon, The Poole–Frenkel pre-exponential factor, *Thin Solid Films* **11**, 183–186 (1972).

[13] H. Fujimoto, M. Yahiro, S. Yukiwaki, K. Kusuhara, N. Nakamura, T. Suekane, H. Wei, K. Imanishi, K. Inada, C. Adachi, Influence of material impurities in the hole-blocking layer on the lifetime of organic light-emitting diodes, *Appl. Phys. Lett.* **109**, 243302 (2016).

[14] H. Fujimoto, T. Suekane, K. Imanishi, S. Yukiwaki, H. Wei, K. Nagayoshi, M. Yahiro, C. Adachi, Influence of vacuum chamber impurities on the lifetime of organic light-emitting diodes, *Sci. Rep.* **6**, 38482 (2016).

[15] F. Wölzl, I. R. de Moraes, B. Lüssem, S. Hofmann, K. Leo, M. C. Gather, Performance and lifetime of vacuum deposited organic light-emitting diodes: influence of residual gases present during device fabrication, *Org. Electron.* **15**, 3251–3258 (2014).

[16] T. Ikeda, H. Murata, Y. Kinoshita, J. Shike, Y. Ikeda, M. Kitano, Enhanced stability of organic light-emitting devices fabricated under ultra-high vacuum condition, *Chem. Phys. Lett.* **426**, 111–114 (2006).

[17] Y. Esaki, T. Matsushima, C. Adachi, Dependence of the amorphous structures and photoluminescence properties of tris(8-hydroxyquinolinato)aluminum films on vacuum deposition conditions, *Org. Electron.* **67**, 237–241 (2019).

Chapter 4

Dependence of the amorphous structures and photoluminescence properties of Alq_3 films on vacuum deposition conditions

Y. Esaki, T. Matsushima, and C. Adachi
Organic Electronics **67**, 237−241 (2019).

4-1. Introduction

In Chapters 2 and 3, I found that both carrier transport and air stability were enhanced in the high-density amorphous films of α-NPD obtained by optimizing T_{sub} [1,2]. To fabricate high-performance OLEDs using highly stable vacuum-deposited films, it is important to investigate how deposition conditions affect the PL properties of films. In this chapter, I focus on Alq_3, a famous emitting material used in OLEDs. I control T_{sub} and deposition rates during vacuum deposition of Alq_3 films and then investigate their amorphous structures and PL properties in detail, especially focusing on an effect of inclusion of impurities into Alq_3 films. It is revealed that a lower T_{sub} and higher deposition rate accelerate PL quenching in Alq_3 films. Although there is no clear relationship between amorphous structures (molecular orientation and density) and PL properties, inclusion of impurities in Alq_3 films is probably related to the observed PL quenching. Impurities in organic films are known to act as PL quencher and accelerate degradation of OLEDs [3–6]. These results highlight the importance of managing impurities in organic films to obtain high-performance organic devices.

4-2. Experimental

Highly pure Alq_3 (sublimation grade, Nippon Steel & Sumikin Chemical) was used for film fabrication. The purity of the Alq_3 powder estimated using elemental analysis based on the amount of carbon was 99.7%. Thermal analysis of Alq_3 powder at 1 atm and 1 Pa by thermogravimetry–differential thermal analysis did not reveal a clear T_g. Alq_3 films with a thickness of approximately 100 nm were vacuum-deposited on clean Si and fused silica substrates under a pressure of $(2.0\pm0.5) \times 10^{-4}$ Pa. An alumina crucible (C-1, Nilaco) was used as an evaporation source for Alq_3 and was carefully cleaned by ultrasonication in chloroform and dried under vacuum before every Alq_3 deposition. First, I used T_{sub} ranging from 200 to 400 K and a constant deposition rate of 0.1 nm/s to prepare Alq_3 films. Next, I used deposition rates ranging from 0.01 to 1 nm/s and a constant T_{sub} of 299 K. The deposition rates and thicknesses of Alq_3 films were monitored with a quartz crystal microbalance.

Variable angle spectroscopic ellipsometry was carried out on Alq_3 films deposited on Si substrates to analyze amorphous structures. The detailed measurement methods and fitting procedure were already explained in Chapter 2. The oscillator model parameters shown in **Table 4-1** and **4-2** were used for the fitting. Several examples of fitting results are presented in **Fig. 4-1**.

Table 4-1. Oscillator model parameters (Gaussian).

Oscillator type	Amplitude	Energy (eV)	Breadth (eV)
Gaussian	0.064851	3.8458	0.3598
Gaussian	1.3342	4.5438	0.17219
Gaussian	1.902	4.6727	0.3182
Gaussian	1.1415	5.0112	1.0954

Table 4-2. Oscillator model parameters (Tauc–Lorentz).

Oscillator type	Amplitude	Energy (eV)	C (eV)	Gap energy (eV)
Tauc–Lorentz	10.472	2.9848	0.53424	2.5389

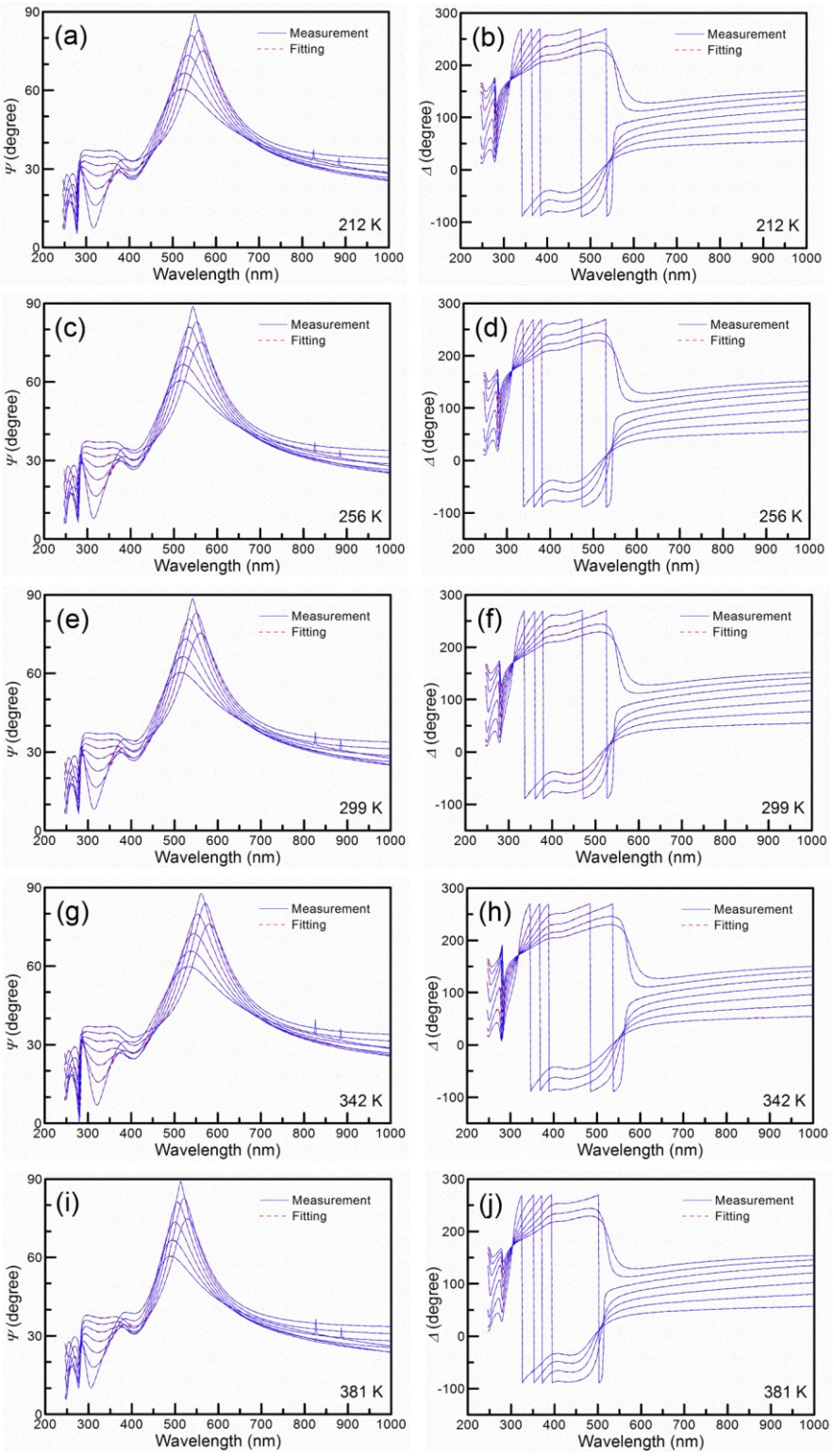

Fig. 4-1. Examples of (a, c, e, g, i) Ψ and (b, d, f, h, j) Δ curves of Alq_3 films vacuum-deposited at different T_{sub}. The experimental data (blue solid lines) was successfully fitted with the model (red dashed lines).

Spectra of refractive index n and extinction coefficient k, and film thickness d were obtained from the fitting. The orientation order parameter S was calculated using **Eq. (2-1)** with k values at a wavelength of 268.54 nm, which corresponds to the π-π^* transition of Alq_3. The molecular orientation discussed here indicates the orientation of the transition dipole moment of Alq_3. A solution method was used to precisely estimate a variation of Alq_3 densities among films [7]. Specifically, a film deposited on a Si substrate was dissolved in chloroform (20 mL, Wako Pure Chemical) and an absorbance of the solution was measured with a spectrometer (LAMBDA 950, PerkinElmer). From the absorbance at 260 nm and a calibration curve measured beforehand, the mass of the film was obtained. The film volume was simply calculated by multiplying d and the film area. Film density ρ was calculated by dividing the mass by the volume. The fluorescence quantum yield Φ and lifetime τ of Alq_3 films deposited on quartz substrates were measured using Quantaurus-QY system (Hamamatsu Photonics) under Ar flow with an excitation wavelength of 392 nm and Quantaurus-tau system (Hamamatsu Photonics) in air with an excitation wavelength of 405 nm, respectively. To assess the film degradation during the measurements, Φ and τ were measured twice: for films fabricated with lower to higher T_{sub} (or deposition rates) in order and then *vice versa*.

4-3. Results and Discussion

4-3-1. Film structure analysis

Alq_3 films deposited at every T_{sub} and deposition rate were smooth and amorphous. Although some tiny particles were observed on the surfaces of films deposited at a high deposition rate of 1 nm/s, VASE results were successfully fitted with the optical model. From the VASE results, *n* and *k* spectra and *d* values of each film were estimated. Most films had different *n* and *k* spectra between the directions parallel and perpendicular to the substrate, indicating anisotropic molecular orientation. Representative *n* and *k* spectra are shown in **Fig. 4-2**.

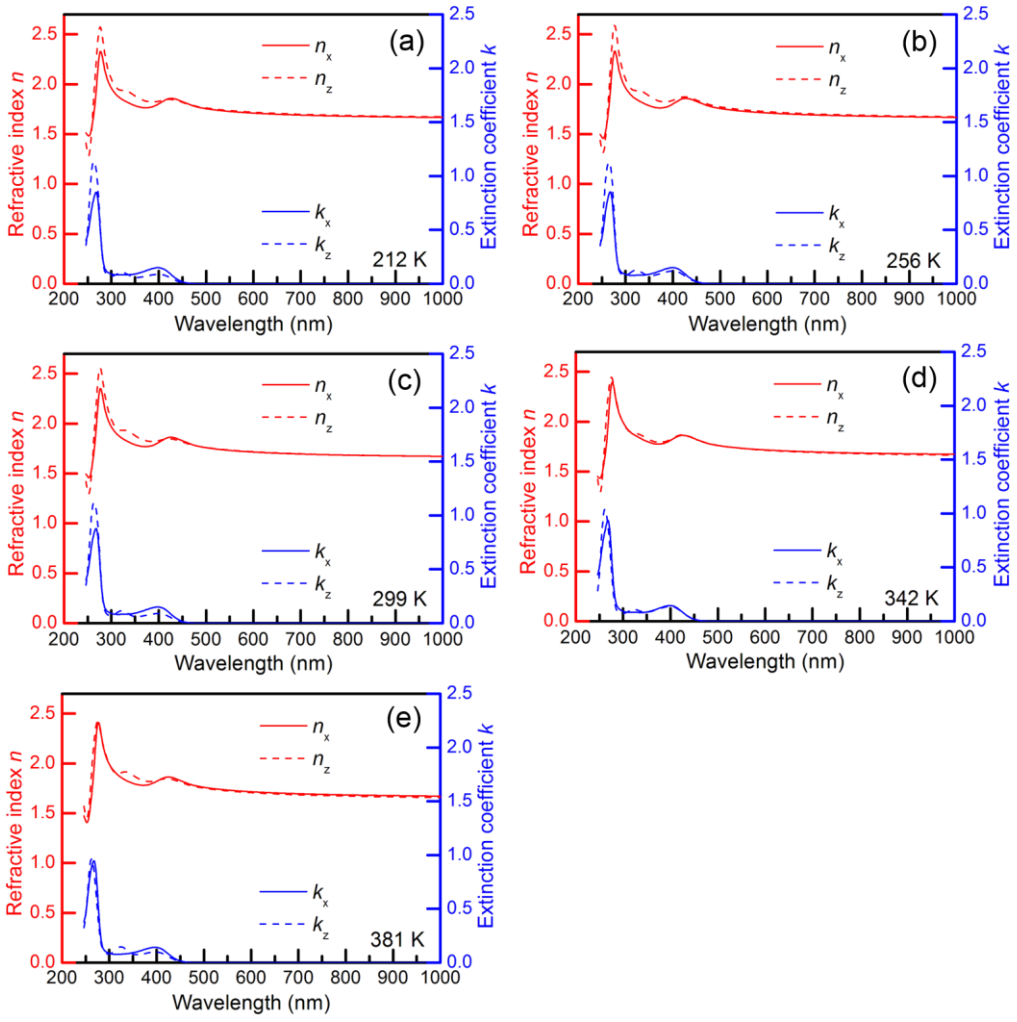

Fig. 4-2. Refractive index *n* and extinction coefficient *k* spectra of Alq_3 films vacuum-deposited at a T_{sub} of (a) 212, (b) 256, (c) 299, (d) 342, and (e) 381 K.

Alq_3 films were annealed at various temperatures under vacuum to estimate T_g. When amorphous films experience a glass transition during annealing, the molecular orientation becomes random [8,9]. However, crystallization occurred in all annealed Alq_3 films, and the molecular orientation of the annealed films could not be evaluated, indicating that Alq_3 films have no detectable T_g.

First, I evaluated S and ρ of Alq_3 films fabricated at different T_{sub} and a constant deposition rate of 0.1 nm/s [**Fig. 4-3**(a) and (b)]. S values depended on T_{sub}; Alq_3 films were anisotropic at T_{sub} < 320 K and T_{sub} > 320 K and random at a T_{sub} of ~320 K. T_{sub} dependence of molecular orientation has been reported for amorphous films of rod- or disk-shaped molecules [8,10]. **Figure 4-3**(a) indicates that molecular orientation can be controlled by T_{sub} even for spherical Alq_3 molecules.

Values of ρ also depended on T_{sub}, with a maximum value at T_{sub} of 320–340 K. The T_{sub} dependence of ρ observed for the Alq_3 films is similar to those of stable glasses of other organic materials [1,8]. It has been reported that the highest ρ is obtained when T_{sub} is 0.75–0.9 of $T_{g, bulk}$ of an ordinary glass under vacuum [1,8]. Although the T_g of Alq_3 films could not be detected, the kinetic mobility of Alq_3 molecules is believed to depend on T_{sub}.

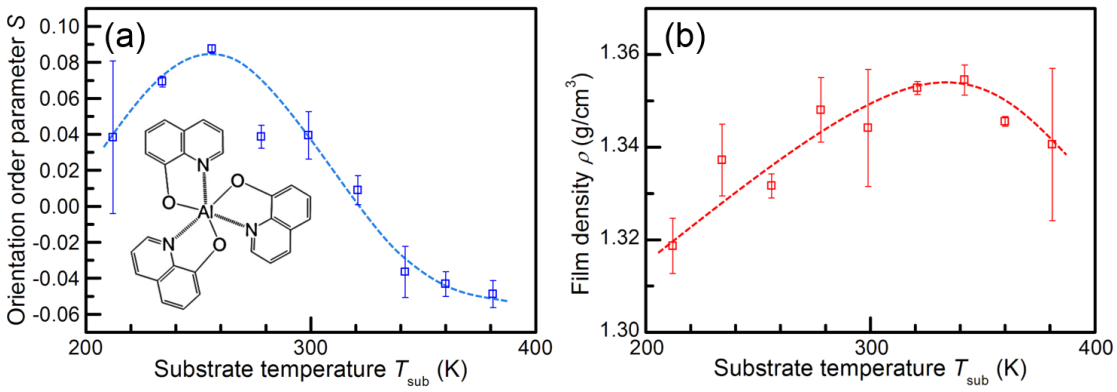

Fig. 4-3. Dependence of (a) orientation order parameter S and (b) density ρ of Alq_3 films on substrate temperature (T_{sub}) during deposition. Inset in (a) is the molecular structure of Alq_3.

4-3-2. Substrate-temperature dependence of photoluminescence properties

PL properties of Alq_3 films deposited at different T_{sub} were investigated. Plots of Φ and τ as a function of T_{sub} are shown in **Fig. 4-4**(a) and (b), respectively. The obtained values of Φ and τ for films deposited at T_{sub} = 299 K were similar to those in a previous report [11]. The values measured in the first and second scans overlapped with each other, indicating negligible film degradation during measurements. Both Φ and τ decreased as T_{sub} decreased. Next, the radiative decay rate constant k_r and the sum of other rate constants ($k_{nr} + k_{ISC} + k_q$) were calculated using following equations:

$$k_r = \frac{\phi}{\tau} , \qquad (4\text{-}1)$$

$$k_{nr} + k_{ISC} + k_q = \frac{1-\phi}{\tau}. \qquad (4\text{-}2)$$

Here, k_{nr}, k_{ISC}, and k_q are the rate constants of non-radiative decay, intersystem crossing, and quenching, respectively. **Figure 4-4**(c) and (d) present the T_{sub} dependence of k_r and $k_{nr} + k_{ISC} + k_q$, respectively. While k_r values were almost similar among films, $k_{nr} + k_{ISC} + k_q$ values clearly increased as T_{sub} decreased. Values of k_r seemed to depend slightly on T_{sub}; the reason for this is still unclear and under investigation. Meanwhile, $k_{nr} + k_{ISC} + k_q$ values clearly increased as T_{sub} decreased. Both S and ρ did not have a clear relation to $k_{nr} + k_{ISC} + k_q$. If T_{sub} affects k_{nr} and k_{ISC}, T_{sub} may affect k_r similarly to k_{nr} and k_{ISC} because these rate constants are the intrinsic properties of Alq_3. However, the trend of $k_{nr} + k_{ISC} + k_q$ against T_{sub} was different from that of k_r. This may mean that the contribution of k_{nr} and k_{ISC} to $k_{nr} + k_{ISC} + k_q$ is small and an increase of k_q is the reason for the observed increase of $k_{nr} + k_{ISC} + k_q$ at low T_{sub}. PL quenching represented by an increased k_q can be caused by the inclusion of impurities that work as PL quenchers in Alq_3 films.

Impurities included in vacuum-deposited films can originate from the source material used for the vacuum deposition or the atmosphere in the vacuum chamber. When the source material contains impurities, both the material and impurities may evaporate together from the heated evaporation source. At low T_{sub}, impurities are easily buried under Alq_3 molecules because the kinetic mobility of impurities is relatively small. On the other hand, at high T_{sub}, the kinetic mobility of impurities is enhanced, which results in a more frequent re-sublimation of impurities from films and a decrease of impurity concentration. Even when a pure source material is used, impurities may be produced by decomposition or side reactions of the heated source material. The impurities existing in the

atmosphere of the vacuum chamber should also be considered. A longer fabrication time at lower deposition rate gives more opportunities for impurities from the vacuum chamber atmosphere to be included in films. Not only water and oxygen molecules but also materials previously used in the vacuum chamber could behave as impurities [3–6].

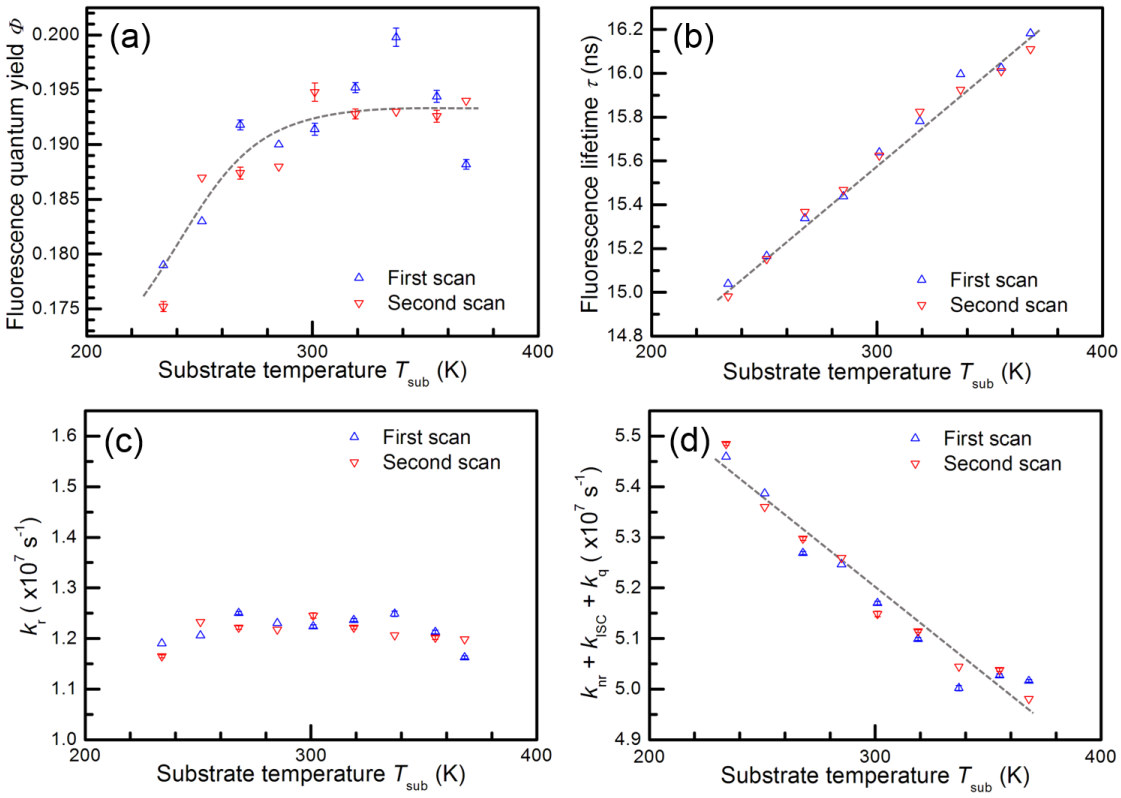

Fig. 4-4. Dependence of PL properties of Alq_3 films on T_{sub}. (a) Fluorescence quantum yield Φ, (b) fluorescence lifetime τ, (c) radiative decay rate constant k_r, and (d) the sum of other rate constants $k_{nr} + k_{ISC} + k_q$.

4-3-3. Deposition-rate dependence of photoluminescence properties

To gain insight into the origin(s) of impurities in the Alq_3 films, I investigated the amorphous structures and PL properties of Alq_3 films fabricated using different deposition rates and a constant T_{sub} of 299 K. As shown in **Fig. 4-5**, changes of S and ρ for these films were very small compared with those of films fabricated using different T_{sub} (**Fig. 4-3**), indicating that deposition rate has less influence than T_{sub} on the amorphous structures.

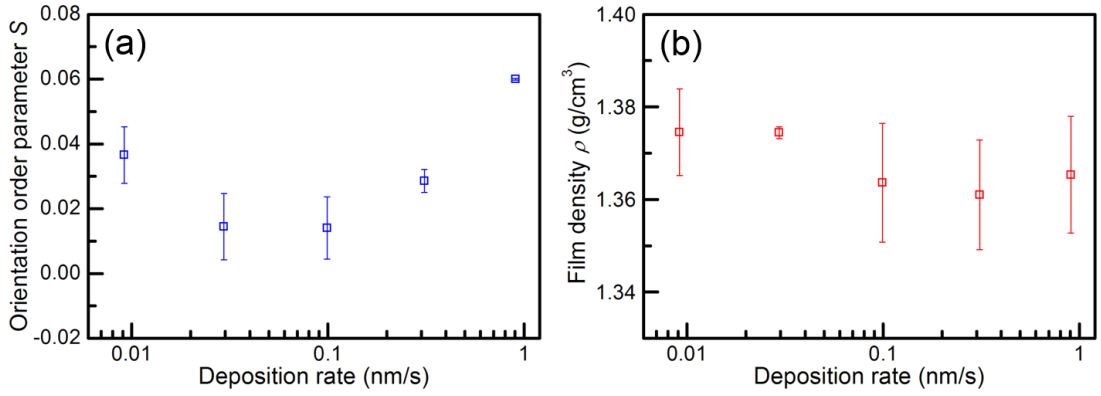

Fig. 4-5. Dependence of (a) orientation order parameter S and (b) density ρ of Alq_3 films on deposition rate.

Conversely, both Φ and τ clearly decreased monotonically as deposition rate increased [**Fig. 4-6**(a) and (b)]. Values of k_r and $k_{nr} + k_{ISC} + k_q$ of each film were calculated and are shown in **Fig. 4-6**(c) and (d), respectively. Although it was difficult to see a correlation between k_r and deposition rate, $k_{nr} + k_{ISC} + k_q$ unquestionably increased at high deposition rates. As I discussed earlier, the change of $k_{nr} + k_{ISC} + k_q$ may be attributed to the change of k_q. A higher deposition rate corresponds to a shorter deposition time to obtain the same film thickness, which means that impurities from the vacuum chamber atmosphere have less opportunity to reach the film surface. To obtain higher deposition rate, the evaporation source was heated at higher temperature. This may cause decomposition or side reactions of Alq_3 molecules and evaporation of more impurities from the Alq_3 powder source. Therefore, the origin of impurities that induced PL quenching in these films is probably the Alq_3 powder and not the vacuum chamber atmosphere.

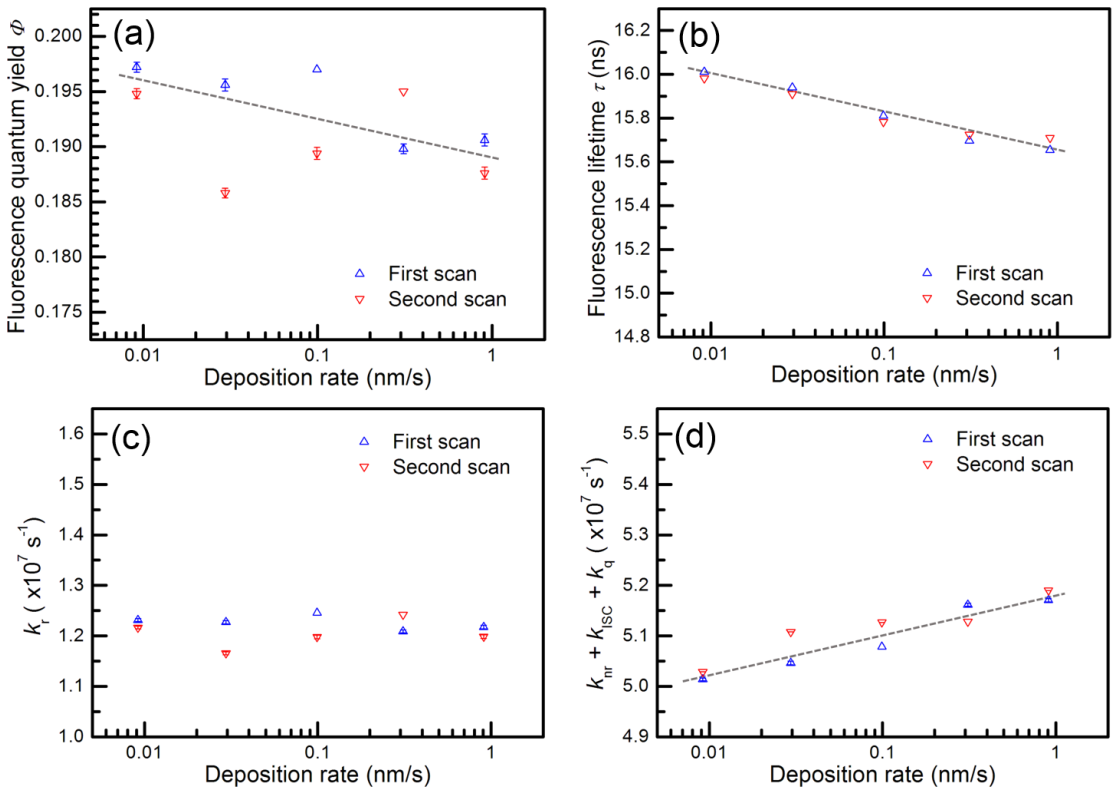

Fig. 4-6. Dependence of PL properties of Alq_3 films on deposition rate. (a) Fluorescence quantum yield Φ, (b) fluorescence lifetime τ, (c) radiative decay rate constant k_r, and (d) the sum of other rate constants $k_{nr} + k_{ISC} + k_q$. The scales of the vertical axes are the same in **Fig. 4-4** and **4-6** for each parameter.

4-3-4. Discussion

It is important to identify the chemical species of the impurities in films. Unfortunately, it was difficult to analyze the trace amount of impurities in my deposited films using liquid chromatography and mass spectroscopy because quinolate ligands were easily eliminated during the analysis. Hydrolysis of Alq_3 occurs during thermal annealing even in the presence of a trace amount of water [12–14]. This hydrolysis produces 8-hydroxyquinoline (8-HQ) and Alq_2-OH by replacing one quinolate ligand with a hydroxyl group. Calculation and experimental results implied that 8-HQ and Alq_2-OH themselves cannot work as quenchers for Alq_3 but products of further reactions, such as Alq_2-O-Alq_2 and condensed 8-HQs, may quench Alq_3 excited states. Therefore, I speculate that the above-mentioned chemical reactions occur in the heated Alq_3 powder source with a trace amount of water and that generated impurities like Alq_2-O-Alq_2 and condensed 8-HQs evaporate together with Alq_3 and work as quenchers in the films. The amount of such quenching impurities in the films would be larger when T_{sub} is lower and deposition rate is higher. I need further studies to fully understand how impurities are generated in the heated powder and incorporated into films.

Organic films are usually vacuum-deposited on room-temperature substrates for OLED fabrication. However, my results indicate that the effect of impurities on PL properties cannot be ignored even for the films fabricated using this standard condition. To minimize the impurity concentration and obtain true PL properties, organic films should be vacuum-deposited at as high as possible for T_{sub} and as low as possible for deposition rate. Impurities may exist that do not affect the PL properties but lower OLED operational stability [4]. Thus, it is necessary to choose suitable deposition conditions for each organic material considering ρ, S, and impurities to enhance OLED performance.

4-4. Conclusion

I prepared Alq_3 films by vacuum deposition at different T_{sub} and deposition rates and investigated their S, ρ, and PL properties. S and ρ strongly depended on T_{sub}, even for the spherical-shaped molecule Alq_3, as observed in previous reports on stable glasses [8,10] and Chapter 2 [1]. PL quenching occurred in all Alq_3 films investigated and became stronger in films fabricated at lower T_{sub} and higher deposition rate. The PL quenching is believed to originate from the inclusion of impurities in films during vacuum deposition. These results emphasize the importance of decreasing the amount of impurities in deposited films by not only purifying the source material but also optimizing film fabrication conditions for device applications.

References

[1] Y. Esaki, T. Komino, T. Matsushima, C. Adachi, Enhanced electrical properties and air stability of amorphous organic thin films by engineering film density, *J. Phys. Chem. Lett.* **8**, 5891–5897 (2017).

[2] Y. Esaki, T. Matsushima, C. Adachi, Discussion on hole traps of amorphous films of *N*,*N*'-di(1-naphthyl)-*N*,*N*'-diphenyl-(1,1'-biphenyl)-4,4'-diamine (α-NPD) deposited at different substrate temperatures, *Appl. Phys. Lett.* **114**, 173301 (2019).

[3] H. Fujimoto, M. Yahiro, S. Yukiwaki, K. Kusuhara, N. Nakamura, T. Suekane, H. Wei, K. Imanishi, K. Inada, C. Adachi, Influence of material impurities in the hole-blocking layer on the lifetime of organic light-emitting diodes, *Appl. Phys. Lett.* **109**, 243302 (2016).

[4] H. Fujimoto, T. Suekane, K. Imanishi, S. Yukiwaki, H. Wei, K. Nagayoshi, M. Yahiro, C. Adachi, Influence of vacuum chamber impurities on the lifetime of organic light-emitting diodes, *Sci. Rep.* **6**, 38482 (2016).

[5] T. Ikeda, H. Murata, Y. Kinoshita, J. Shike, Y. Ikeda, M. Kitano, Enhanced stability of organic light-emitting devices fabricated under ultra-high vacuum condition, *Chem. Phys. Lett.* **426**, 111–114 (2006).

[6] F. Wölzl, I. Rabelo de Moraes, B. Lüssem, S. Hofmann, K. Leo, M. C. Gather, Performance and lifetime of vacuum deposited organic light-emitting diodes: influence of residual gases present during device fabrication, *Org. Electron.* **15**, 3251–3258 (2014).

[7] H.-F. Xiang, Z.-X. Xu, V. A. L. Roy, C.-M. Che, P. T. Lai, Method for measurement of the density of thin films of small organic molecules, *Rev. Sci. Instrum.* **78**, 034104 (2007).

[8] S. S. Dalal, D. M. Walters, I. Lyubimov, J. J. de Pablo, M. D. Ediger, Tunable molecular orientation and elevated thermal stability of vapor-deposited organic semiconductors, *Proc. Natl. Acad. Sci.* **112**, 4227–4232 (2015).

[9] Y. Sakai, M. Shibata, D. Yokoyama, Simple model-free estimation of orientation order parameters of vacuum-deposited and spin-coated amorphous films used in organic light-emitting diodes, *Appl. Phys. Express* **8**, 096601 (2015).

[10] D. M. Walters, L. Antony, J. J. de Pablo, M. D. Ediger, Influence of molecular shape on the thermal stability and molecular orientation of vapor-deposited organic semiconductors, *J. Phys. Chem. Lett.* **8**, 3380–3386 (2017).

[11] Y. Kawamura, H. Sasabe, C. Adachi, Simple accurate system for measuring absolute photoluminescence quantum efficiency in organic solid-state thin films, *Jpn. J. Appl. Phys.* **43**, 7729–7730 (2004).

[12] F. Papadimitrakopoulos, X.-M. Zhang, D. L. Thomsen, K. A. Higginson, Chemical failure mechanism for aluminum(III) 8-hydroxyquinoline light-emitting devices, *Chem. Mater.* **8**, 1363–1365 (1996).

[13] K. A. Higginson, X.-M. Zhang, F. Papadimitrakopoulos, Thermal and morphological effects on the hydrolytic stability of aluminum tris(8-hydroxyquinoline) (Alq_3), *Chem. Mater.* **10**, 1017–1020 (1998).

[14] J. E. Knox, M. D. Halls, H. P. Hratchian, H. B. Schlegel, Chemical failure modes of AlQ3-based OLEDs: AlQ3 hydrolysis, *Phys. Chem. Chem. Phys.* **8**, 1371–1377 (2006).

Chapter 5

Effect of structural control of amorphous films on performance of organic light-emitting diodes

Y. Esaki, M. Tanaka, T. Matsushima, and C. Adachi

In preparation.

5-1. Introduction

In the previous chapters, I discussed the effect of T_{sub} during vacuum-deposition on amorphous films of organic semiconductor materials used in OLEDs. In this chapter, I performed a comprehensive study on how the OLED performance is affected by the changes in amorphous structures controlled using T_{sub}. There have been several studies on the effect of T_{sub} on OLED performance. Komino *et al*. reported that external quantum efficiency (EQE) of OLEDs based on TADF emitters was enhanced by choosing organic molecules horizontally oriented relative to a substrate plane because of the improved carrier balance [1] and light outcoupling efficiency [2,3]. These reports focused on molecular orientation, and film density and thermal stability were not investigated. Recently, Ribé *et al*. reported that EQE and operational stability of OLEDs based on phosphorescent emitters were dramatically enhanced by optimizing T_{sub} and increasing the density and thermal stability of organic emitting layers [4]. In a high-density emitting layer, the non-radiative decay of emitter molecules was suppressed [4] and the photostability was improved [5,6], which led to the enhancement of EQE and operational stability.

On the other hand, it is known that vacuum-deposited amorphous films have molecular anisotropy and, therefore, have spontaneous orientation polarization (SOP, P_0) in the substrate-normal direction originating from the oriented permanent dipole moments p of molecules [7–12] as shown in **Fig. 5-1**. Here, P_0 is given by:

$$P_0 = p\langle \cos \theta_{PDM} \rangle N_0, \qquad (5\text{-}1)$$

where θ_{PDM} is the orientation degree of permanent dipole moment of the molecules to the substrate-normal direction and N_0 is the number density of the molecules. Although one may think that films of organic materials with large permanent dipole moment have large SOP considering **Eq. (5-1)**, there are many materials which do not follow a linear relationship between permanent dipole moment and SOP [11]. To explain this phenomenon, not only a horizontal orientation of permanent dipole moments but also a formation of an anti-parallel configuration of molecules have been suggested [10,11]. It was reported that the direction of SOP is unchanged even when an organic layer is deposited on another organic layer with opposite surface potential [8]. The effect of molecular geometry [9] on the SOP formation is more significant than that of an underlying layer and a substrate. In spite of these previous reports, the detailed SOP formation process and relationship between amorphous structures and SOP

is not completely understood. In actual OLED structures, a difference in SOP between stacked organic layers is known to cause a charge accumulation at the organic/organic interface [13]. Additionally, SOP itself and SOP-induced charge accumulation are known to be related to carrier injection efficiency [14] and device degradation [15–18]. Therefore, it is important to clarify the influence of SOP on OLED performance. Even though a comparison of two materials with different SOPs seems to be a simple way to investigate SOP in OLEDs, it is virtually impossible to change only the permanent dipole because other parameters, such as molecular orientation, energy level, and carrier transport properties, are also changed simultaneously.

In this chapter, I aim at controlling SOP of single-material films by changing T_{sub}. To investigate SOP, OLEDs are fabricated with a simple two-layer structure containing an α-NPD hole transporting layer and an Alq_3 electron transporting and emitting layer vacuum-deposited at different T_{sub}. I discuss the relationship between T_{sub}, SOP, and OLED performance.

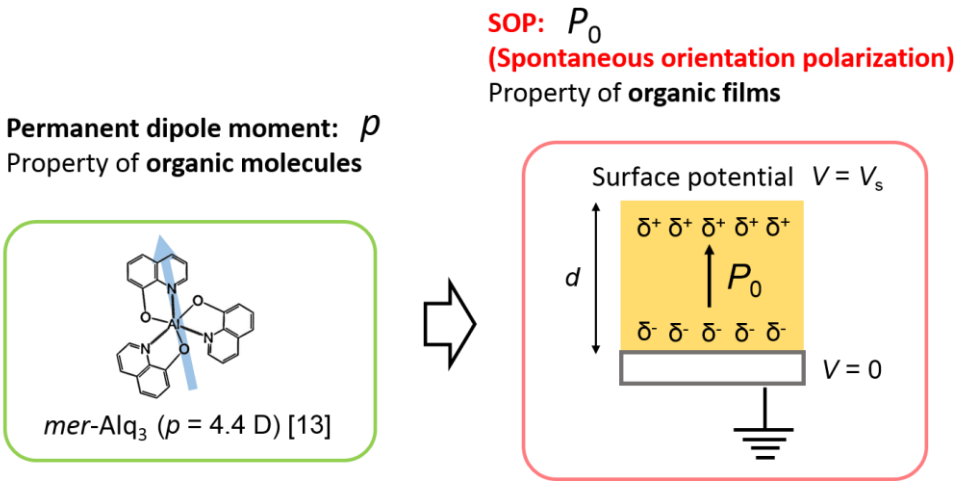

Fig. 5-1. Schematics of permanent dipole moment and spontaneous orientation polarization. V_s is the surface potential of a film.

5-2. Experimental

Both α-NPD and Alq_3 were purchased from Nippon Steel & Sumikin Chemical and used as-received. With these materials, I fabricated OLEDs with a structure of glass substrate/ITO (100 nm)/α-NPD (100 nm)/Alq_3 (80 nm)/LiF (0.8 nm)/Al (100 nm). Alq_3 is known to form amorphous films with the large SOP while the SOP of α-NPD films is small [13–15,19]. First, ITO-coated glass substrates were carefully cleaned by sequential ultrasonication in detergent, water, acetone, and isopropanol, followed by UV/O_3 treatment. Vacuum deposition was performed at a base pressure of $< 2.0 \times 10^{-4}$ Pa under the dark. A pressure sensor was turned off during vacuum deposition to avoid its influence on SOP properties [19]. α-NPD was vacuum-deposited on the substrates kept at 286 K, where the electrical properties and air stability of α-NPD is most enhanced as discussed in Chapter 2 [20]. Then, Alq_3 was vacuum-deposited at various T_{sub} ranging from 240 to 330 K to obtain different amorphous structures as discussed in Chapter 4 [21]. T_{sub} was calibrated using an alumel/chromel thermocouple beforehand. LiF and Al were deposited at room temperature as a cathode to complete OLEDs. Deposition rates of α-NPD and Alq_3 were 0.15–0.2 nm/s. The active device area was 0.04 cm^2. Completed OLEDs were directly transferred from the vacuum chamber to a glove box filled with nitrogen and encapsulated using a glass cap, a desiccant sheet, and UV curing epoxy resin. *J*–*V*–EQE characteristics were obtained using a sourcemeter (2400, Keithley) and an integrating sphere system (Hamamatsu Photonics). Operational stability was evaluated using an OLED lifetime measurement system (EAS-26B, System Engineers Co.) under continuous operation at a constant current of 10 mA/cm^2 under the dark.

Displacement current measurements (DCMs) were performed using a waveform generator (waveStation 2052, Teledyne Japan Corporation), a current amplifier (CA5350, NF Corporation), and an oscilloscope (HDO4054, Teledyne Japan Corporation). Triangular-wave voltages in the range of –4 to 4 V were applied to OLEDs. Obtained current signals were converted into capacitance (*C*). One triangular wave was composed of forward (–4 to 4 V) and reverse (4 to –4 V) sweeps with a sweep rate of 100 V/s. This triangular wave was repeatedly applied by 3 times in a single measurement. The data of the third sweep was assumed as a quasi-steady-state and used for discussion.

To get insight into the effect of T_{sub} on the electrical properties of Alq_3, electron-only devices (EODs) were fabricated. The device structure was glass substrate/ITO (100 nm)/Alq_3 (300 nm)/LiF

(0.8 nm)/Al (100 nm). The vacuum deposition conditions and measurement methods of their *J-E* properties were the same as those described earlier.

5-3. Results and discussion

5-3-1. Displacement current measurement

SOP and interfacial charge accumulation in OLEDs composed of α-NPD and Alq_3 layers are discussed based on the interfacial charge model [12,15,22]. Energy diagrams and carrier dynamics are affected by an applied voltage, and are summarized in **Fig. 5-2**. The SOPs of α-NPD and Alq_3 layers are represented as $P_{\alpha\text{-NPD}}$ and P_{Alq3}. It is known that the direction of $P_{\alpha\text{-NPD}}$ and P_{Alq3} are positive and that P_{Alq3} is larger than $P_{\alpha\text{-NPD}}$ because the permanent dipole moment of α-NPD molecules is quite smaller than that of Alq_3. Here, the α-NPD/Alq_3 interface is negatively polarized because $P_{\alpha\text{-NPD}}$ is smaller than P_{Alq3}, and the negative interfacial charge σ_{int} at this interface is given by:

$$\sigma_{int} = P_{\alpha-NPD} - P_{Alq3}. \qquad (5\text{-}1)$$

Here V_{inj} is a voltage, at which hole injection from ITO to α-NPD begins and V_{th} is a voltage, at which hole injection from α-NPD to Alq_3 begins. When the applied voltage is smaller than V_{inj}, holes are not injected into the device but accumulate on the electrodes, and the capacitance corresponding to the whole OLED device (C_{OLED}) is observed [(1) in **Fig. 5-2**]. When the applied voltage reaches V_{inj}, a forward bias is applied to the α-NPD layer and holes are injected [(2) in **Fig. 5-2**]. In the voltage range of $V_{inj} < V < V_{th}$, the injected holes accumulate at the α-NPD/Alq_3 interface. Under this condition, the capacitance originating from the Alq_3 layer (C_{Alq3}) is observed [(3) in **Fig. 5-2**]. Here, the total amount of the accumulated charge (hole) σ_{acc} is equal to $-\sigma_{int}$. Above V_{th}, holes are injected into the Alq_3 layer and recombine with electrons injected from the opposite electrode to induce EL [(4) in **Fig. 5-2**]. V_{inj} and σ_{int} are given by:

$$V_{inj} = V_{th} + \sigma_{int}\frac{S}{C_{Alq3}} \qquad (5\text{-}2) \qquad \text{and}$$

$$\sigma_{int} = (V_{th} - V_{inj})\frac{C_{Alq3}}{S}, \qquad (5\text{-}3)$$

while S is the active area of OLEDs. V_{inj} depends on σ_{int}, which corresponds to a difference in SOP between the α-NPD and Alq_3 layers. σ_{acc} and corresponding σ_{int} can be obtained by dividing an area of a C-V curve in a range from V_{inj} to V_{th} by S.

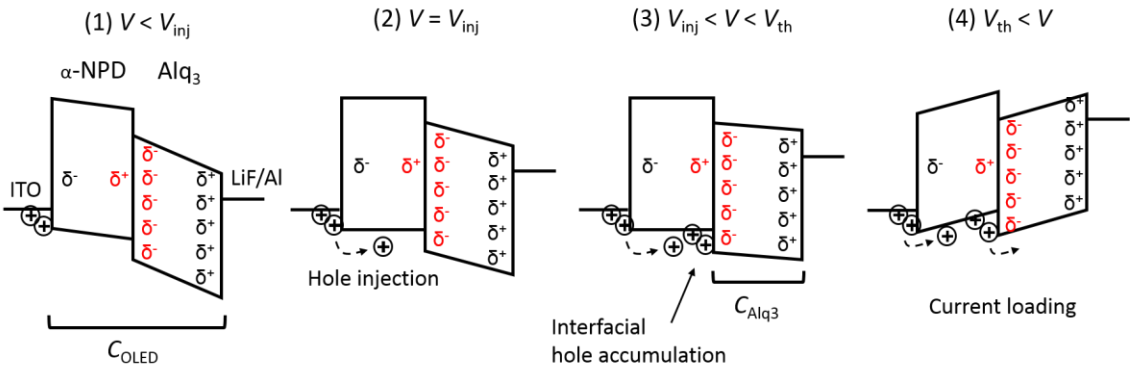

Fig. 5-2. Examples of energy diagrams of a typical OLED containing α-NPD and Alq_3 layers at (1) $V < V_{inj}$, (2) $V = V_{inj}$, (3) $V_{inj} < V < V_{th}$, and (4) $V_{th} < V$.

DCM was performed to obtain how the SOP of Alq_3 is affected by T_{sub}. Representative C-V curves are shown in **Fig 5-3**(a). At –4 V, all OLEDs exhibited similar capacitance around 0.7 nF, which corresponds to the total capacitance of OLEDs (C_{OLED}). Meanwhile, V_{inj} clearly depended on T_{sub} and ranging from –2 to 0 V. It should be noted that when P_{Alq3} is large, hole injection and accumulation can happen even below 0 V. C_{Alq3} values were ~1.6 nF in an accumulation region between V_{inj} and V_{th} but the observed steps of C were not completely flat, probably due to the relatively fast voltage sweep rate used in this study (100 V/s). V_{th} was determined using the capacitance drop in the reverse voltage sweep [19]; there was no clear difference in V_{th} among all OLEDs [see the dotted line in **Fig 5-3**(a)]. OLEDs deposited at 246 K revealed an unusual capacitance rise below V_{th} in the forward voltage sweep as indicated in **Fig. 5-3**(b), probably implying that an injection of holes or electrons accidently happened below V_{th}. Although the formation of trap states is conceivable as an origin of this phenomenon [19], the detail is still unclear. There is a possibility that a small amount of water in the vacuum chamber was condensed and remained in the films and acted as carrier traps as discussed in Chapter 2 [20]. **Figure 5-3**(c) exhibits the T_{sub} dependence of the absolute σ_{int} values calculated by integrating the C-V curves. $|\sigma_{int}|$ decreased almost monotonically as T_{sub} increased, except for the plot at 246 K. This slight decrease of $|\sigma_{int}|$ is possibly related to the formation of carrier traps.

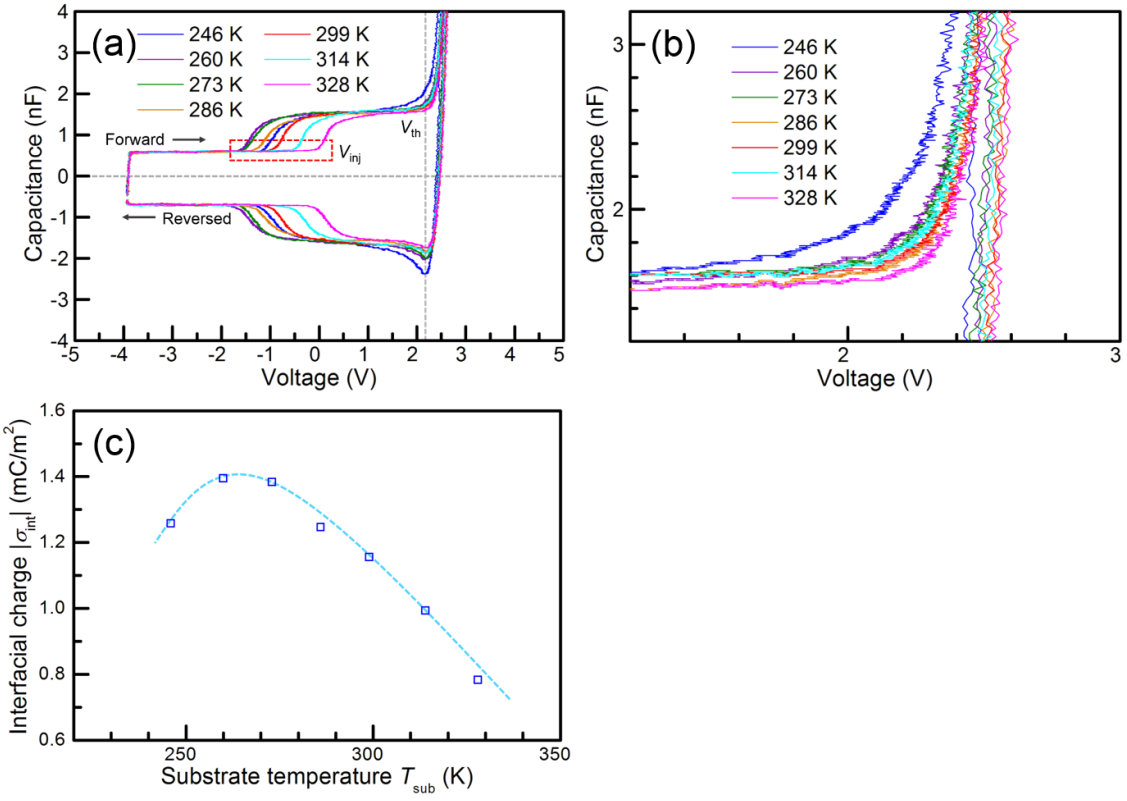

Fig. 5-3. (a) Capacitance (*C*)–voltage (*V*) curves of OLEDs with Alq_3 layers vacuum-deposited at different substrate temperatures (T_{sub}), (b) enlarged view of *C*-*V* curves around V_{th}, and (c) plot of absolute values of interfacial charge (σ_{int}) against T_{sub}, which was obtained from (a).

The obtained value of σ_{int} at a T_{sub} of 299 K (near room temperature) was –1.16 mC/m^2 and consistent with the reported values [13,19]. $P_{\alpha\text{-NPD}}$ is assumed unchanged in all OLEDs because α-NPD was vacuum-deposited at the same condition. Therefore the change of σ_{int} originates from the difference of P_{Alq3}, meaning the dependence of P_{Alq3} on T_{sub}. To my knowledge, this is the first report on a control of SOP in single-material films used for OLEDs.

Formation of an anti-parallel configuration has been suggested as one of the origins of unexpectedly small SOP of a material with large permanent dipole moment [10,11]. In close distance, molecules of such materials are electrostatically stabilized by diminishing their dipole each other. As shown in Chapter 4-3-1, the density of Alq_3 films is maximized at around T_{sub} = 340 K because Alq_3 molecules with sufficient kinetic energy during vacuum deposition can find more stable and packed

configuration. Here, the SOP was smaller at around T_{sub} = 330 K, which is similar to the trend of film density. Probably the SOP of Alq_3 vacuum-deposited at high T_{sub} decreased because Alq_3 molecules tended to find the electrostatically stable anti-parallel configuration. Meanwhile, orientation of transition dipole moment of Alq_3 is affected by T_{sub}, as discussed in Chapter 4-3-1. Although the orientation of permanent dipole moment is expected to be also affected by T_{sub} and influence the SOP, further analysis is difficult at present because I do not have a method to analyze the orientation of permanent dipole moment. I cannot deny the possibility that the horizontal orientation of permanent dipole moment of Alq_3 simply reduced the SOP in the substrate-normal direction.

5-3-2. Current density–voltage properties

Effect of T_{sub} on electrical properties of OLEDs was investigated. *J*-*V* properties of OLEDs, in which Alq_3 layers were vacuum-deposited at different T_{sub}, are shown in **Fig. 5-4**(a) and (b). Although the onset of *J* at 2 V did not depend on T_{sub}, the different *J* appeared at high *V*. For comparison, the *J* values at 6 V were plotted as a function of T_{sub} in **Fig. 5-4**(c). *J* decreased at high T_{sub}. Because the vacuum deposition conditions for the α-NPD hole transporting layers were the same among all the OLEDs, the different *J* can be attributed to a change in electron current in Alq_3 layers.

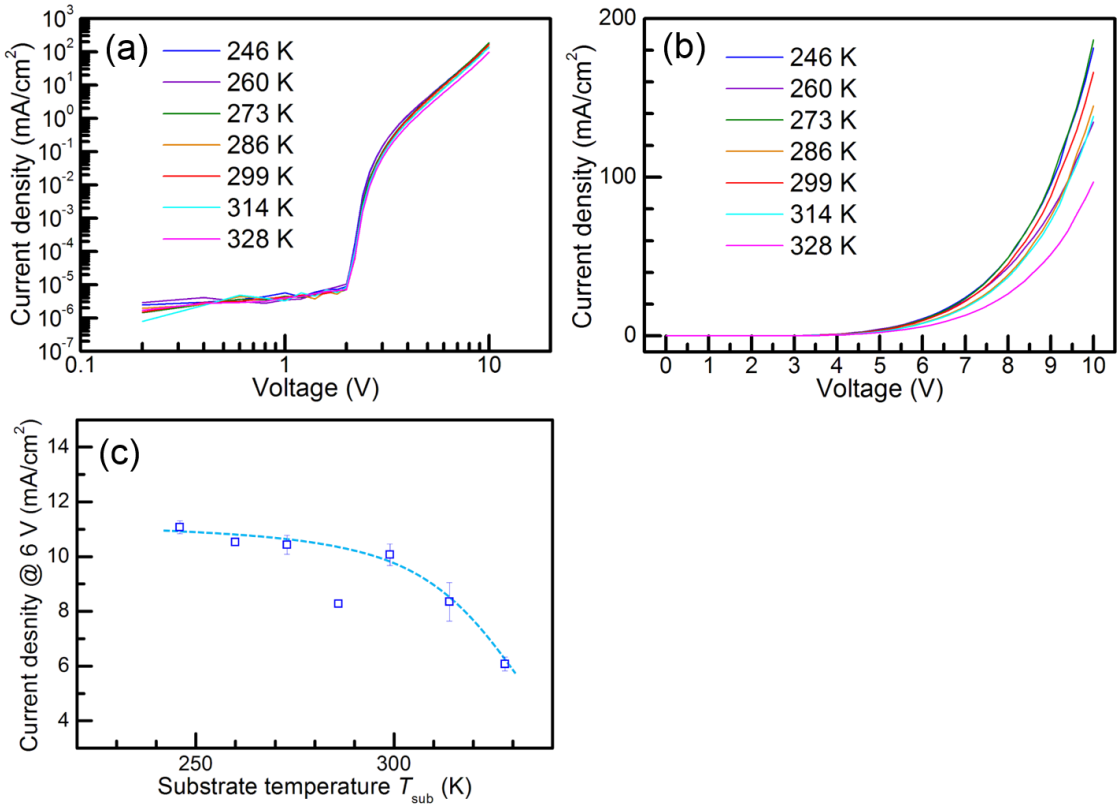

Fig. 5-4. Current density (*J*)–voltage (*V*) properties of OLEDs with Alq_3 layers vacuum-deposited at different substrate temperatures (T_{sub}) with (a) log and (b) linear axes. (c) Plot of *J* values at 6 V against T_{sub}.

EODs of Alq_3 were fabricated for a better understanding of the observed J modulation in OLEDs. J-E properties of EODs and a plot of J values at $E = 3.0 \times 10^5$ V/cm as a function of T_{sub} are shown in **Fig. 5-5**(a) and (b), respectively. Although holes were injected from the ITO anode into the Alq_3 layer above 4.0×10^5 V/cm and weak electroluminescence (EL) was observed, there was no EL below 4.0×10^5 V/cm. Thus, the electron current was assumed to be dominant than the hole current below 4.0×10^5 V/cm. The behavior of the J-E curves of EODs was similar to that of the J-V curves of OLEDs. Values of J at 3.0×10^5 V/cm were smaller when Alq_3 was deposited at high T_{sub}. These results suggest that the electron current in Alq_3 was changed by T_{sub}, leading to the different J-V properties of OLEDs.

The electron current decreased at high T_{sub}, where the density of Alq_3 films was maximum. It is not probable that the change of the orientation of Alq_3 molecules increased a transfer integral between adjacent molecules considering its spherical-shaped molecular structure. Although I found the enhancement of the hole current in high-density α-NPD films, it was not the case in Alq_3 films. A reduction of carrier injection barrier by positive SOP has been suggested because the formation of a dipole at the organic/cathode interface makes the energy levels of organic materials deeper [14]. As indicated in **Fig. 5-3**(c), the SOP of Alq_3 decreased at high T_{sub}. It is conceivable that the smaller SOP results in a weaker interfacial dipole and, therefore, lowers electron injection efficiency. In the case of spherical-shaped molecule of Alq_3, the effect of molecular packing on electron current seems not so large and buried under that of SOP.

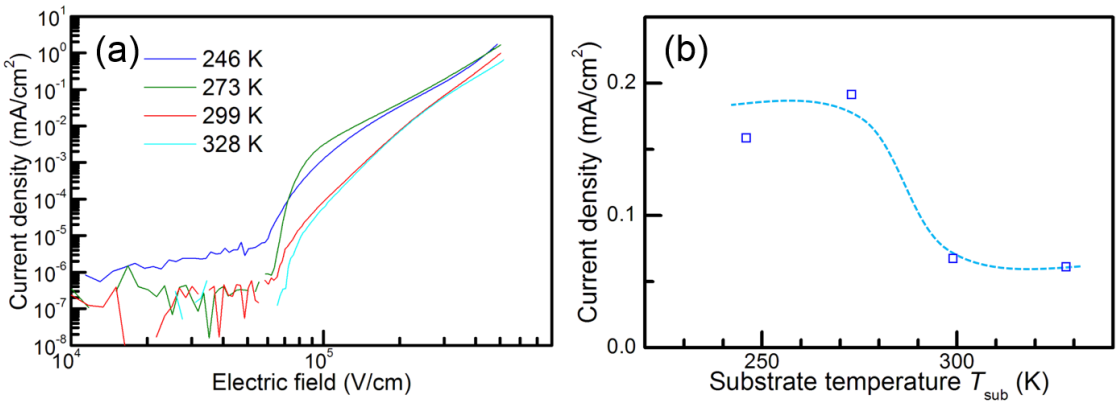

Fig. 5-5. (a) Current density (J)–electric field (E) properties of EODs with Alq_3 layers vacuum-deposited at different substrate temperatures (T_{sub}) and (b) plot of J values at $E = 3.0 \times 10^5$ V/cm against T_{sub}.

5-3-3. External quantum efficiency

EQE-*J* properties of OLEDs and values of EQE at 20 mA/cm^2 are shown in **Fig. 5-6**(a) and (b), respectively. These results exhibited a clear EQE dependence on T_{sub}; EQEs were higher when T_{sub} was increased. The enhancement of EQE between 246 and 328 K was 42 %. Several factors are related to this significant EQE enhancement: (1) fluorescence quantum yield, (2) light outcoupling efficiency, (3) carrier balance, and (4) singlet-polaron annihilation (SPA).

For factor (1), I have already discussed the T_{sub} dependence of fluorescence quantum yield of Alq_3 bulk films in Chapter 4-3-2. According to **Fig. 4-2**(a), the fluorescence quantum yields at T_{sub} = 246 and 328 K were 0.185 and 0.195, respectively, corresponding to the 4.9% increase. The amount of impurities remained in the films were decreased at high T_{sub}, and contributed to the EQE enhancement. Factor (2) seems important because the orientation of transition dipole moment of Alq_3 was proved to be changed by T_{sub}, as discussed in Chapter 4-3-1. To obtain the light outcoupling efficiency, I performed an optical simulation using an OLED simulation software (Setfos, FLUXiM). The anisotropy of *n* and *k* of Alq_3 films and the orientation of transition dipole moment were considered in the optical simulation. The emission of OLEDs with α-NPD and Alq_3 layers is known to happen near the α-NPD/Alq_3 interface when they are vacuum-deposited at room temperature [23]. Because the EL spectra were almost the same in all OLEDs as shown in **Fig. 5-6**(c), the recombination zone can be assumed independent on T_{sub} and fixed at the interface. Thus, the exciton generation was represented as a delta function at the interface of the Alq_3 layer in the optical simulation. The simulation results are shown in **Fig. 5-7**. The light outcoupling efficiency at T_{sub} = 246 and 328 K were 0.19 and 0.21, respectively, corresponding to the 10.5% increase. Although the influence of molecular orientation of spherical-shaped Alq_3 on OLED performance was smaller compared with the case of stick-shaped emitter materials [2,3], its contribution to EQE is still large.

Although the contribution of the ~15% increase can be explained using the fluorescence quantum yield and light outcoupling efficiency, the origin(s) of the remained 27% increase is still unclear. Factor (3) is possible to affect EQE. At high T_{sub}, the amount of the interfacial accumulated holes and electron current decrease simultaneously because of the decrease of SOP in Alq_3 layer, making the estimation of carrier balance complicating. I plan to measure EQE-*J* properties at a high *V* condition and analyze a roll-off behavior of the EQE curves for a further discussion on carrier

dynamics under operation. I believe that factor (4) is the additional origin of the EQE enhancement. As I discussed earlier, carrier recombination happens at the interface where holes are accumulated. Accumulated holes should exist as radical cations of α-NPD. It has been reported that α-NPD cations have an absorption band around a wavelength of 500 nm [24], which overlaps with the emission band of Alq_3. This means that the α-NPD cations can quench the singlet states of Alq_3. The amount of accumulated holes at the interface became smaller at high T_{sub}, as shown in **Fig. 5-3**(c). It is conceivable that the suppression of SPA leads to the EQE enhancement at high T_{sub}. I plan a direct observation of quenching by the accumulated holes to verify this hypothesis.

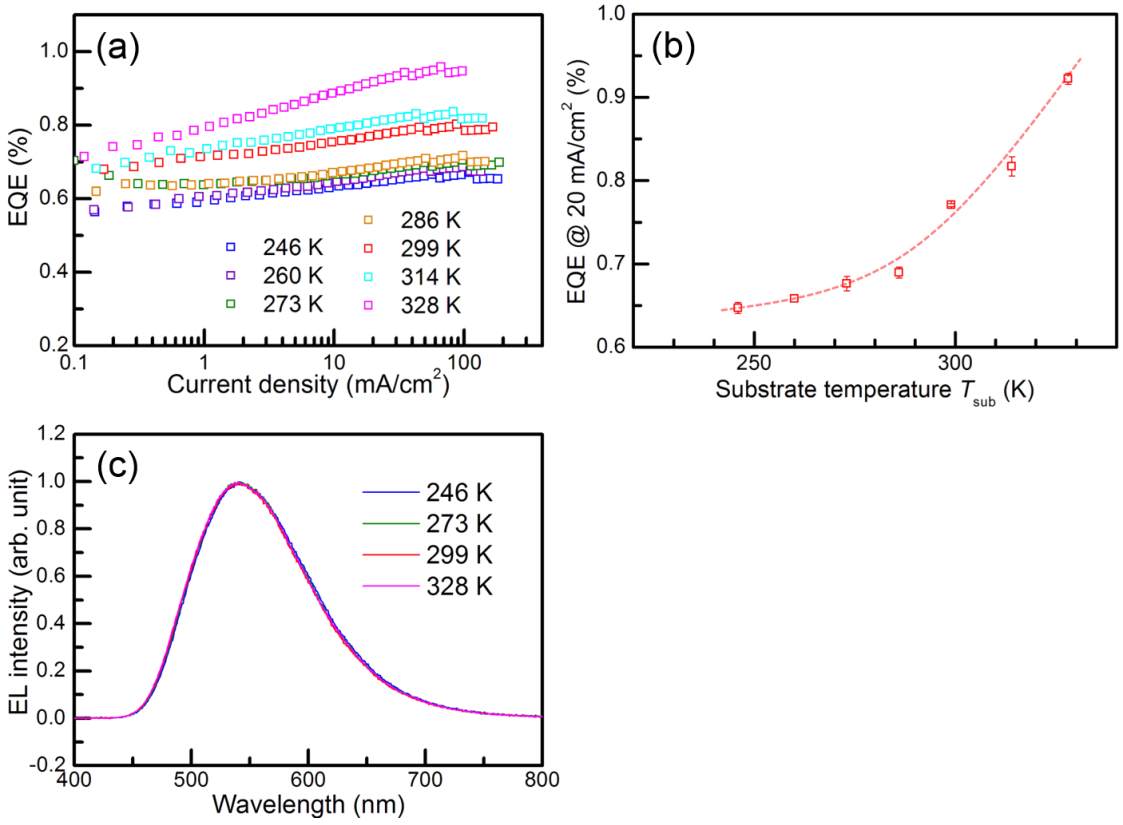

Fig. 5-6. (a) External quantum efficiency (EQE)–current density (J) properties of OLEDs with Alq_3 layers vacuum-deposited at different substrate temperatures (T_{sub}), (b) plot of EQE values at J = 20 mA/cm^2 as a function of T_{sub}. (c) Normalized EL spectra of OLEDs at J = 20 mA/cm^2.

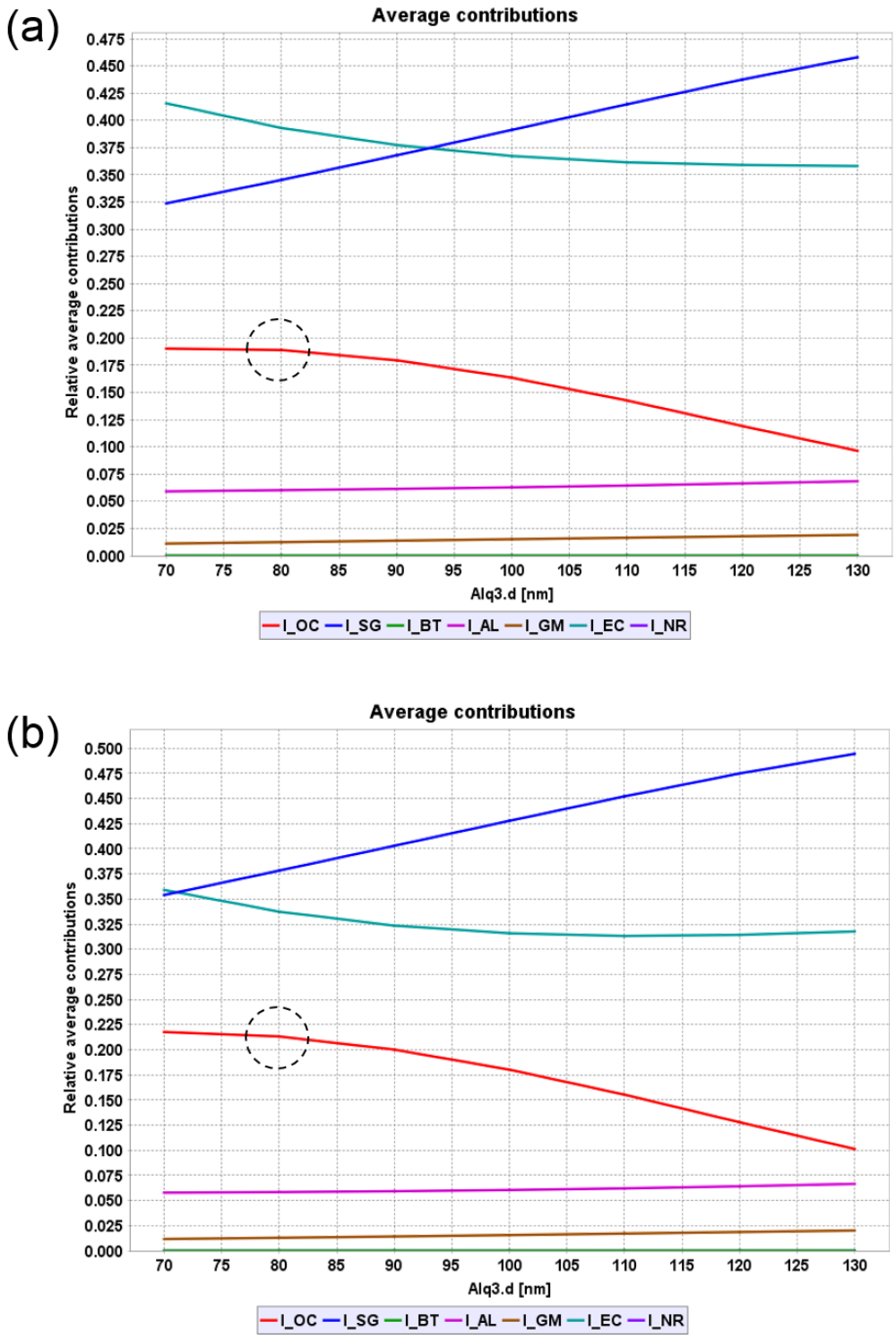

Fig. 5-7 Results of optical simulations for OLEDs with Alq_3 layers vacuum-deposited at a T_{sub} of (a) 246 and (b) 328 K. Red lines are the contributions of the outcoupled mode (I_OC) against the film thickness of Alq_3 layer. The values at the thickness of 80 nm (circled) were used for discussion.

5-3-4. Operational stability

Effect of T_{sub} on the operational stability of OLEDs driven at a constant J of 10 mA/cm^2 was evaluated. Evolution curves of normalized luminance and a plot of LT80 (the time at which the luminance decreased to 80% of the initial value) are shown in **Fig. 5-8**(a) and (b), respectively. Behavior of the luminance evolution was clearly depended on T_{sub}. Note that a slight amount of dark spots was observed after degradation, but I could not find a clear relationship between dark spot generation and T_{sub}. LT80 showed a convex-shaped trend against T_{sub} with the maximum value around 300 K. It seems difficult to relate this unique trend of LT80 directly to the density or SOP of Alq_3 films because the film density was the largest and the SOP was the smallest at around 340 K and did not have any peak around 300 K. Several factors are likely to affect the operational stability. Water molecules incorporated in the film is known to accelerate the degradation of OLEDs because of a chemical decomposition or side-reactions of α-NPD and Alq_3 [25]. In Chapter 4, I suggested that the amount of impurities incorporated in the films during deposition increased when vacuum-deposited at lower T_{sub}, because the re-sublimation of impurities are suppressed by the smaller kinetic energy of molecules [21]. In addition, the density of Alq_3 films deposited at low T_{sub} is low, which results in the penetration and absorption of water molecules into the films during the operation, as discussed in Chapter 2 [20]. Although the amount of water vapor in the encapsulation glass would be quite small, a trace amount of water is known to have a possibility to accelerate the degradation of materials [26]. Therefore, existence of water molecules in Alq_3 films is expected to be one of the reasons for the lower operational stability of OLEDs fabricated at low T_{sub}. On the other hand, in the OLEDs fabricated at high T_{sub}, quenching routes of the singlet Alq_3 (energy transfer to impurities and α-NPD cations induced by SOP) are suppressed and thus the lifetime of the singlet Alq_3 is longer. OLEDs were driven at the same J condition in this measurement. Assuming that the amount of generated excitons are similar in all OLEDs, Alq_3 molecules probably decomposed more significantly when the lifetime of the singlet Alq_3 is longer. Furthermore, considering that the electron current was deceased at high T_{sub}, there is a possibility that a change in carrier balance accelerated a generation of unstable Alq_3 cations [27] and lowered the operational stability.

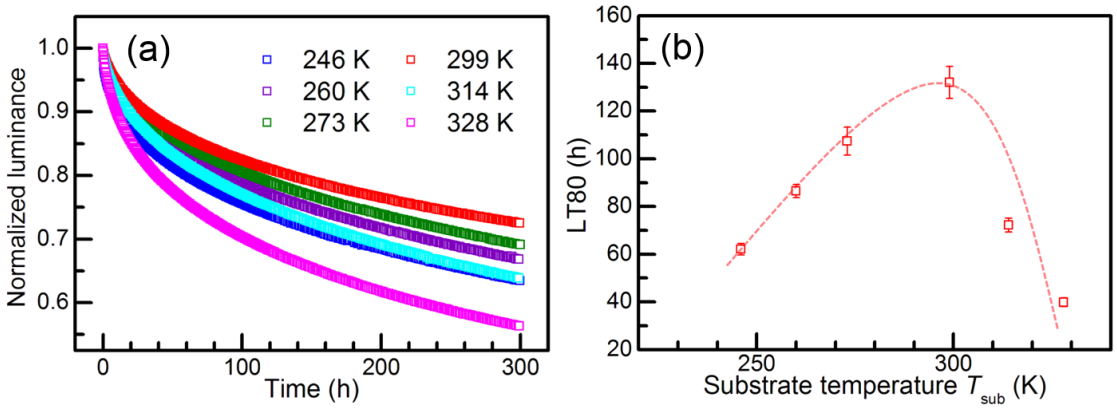

Fig. 5-8. (a) Evolutions of normalized luminance of OLEDs with Alq_3 layers vacuum-deposited at different substrate temperatures (T_{sub}) under continuous operation at a constant current density of 10 mA/cm^2 and (b) T_{sub} dependence of LT80.

It has been reported that the amount of accumulated charge at the interface decreases after the degradation of α-NPD/Alq_3 based OLEDs [15]. This phenomenon has also been observed in OLEDs containing doped emitting layers of phosphorescent and TADF materials [17,18]. Two mechanisms have been suggested for this phenomenon. One is a decrease of SOP due to the randomization of Alq_3 molecules during continuous operation, which was proved using sum frequency generation (SFG) spectroscopy [16]. The other one is the compensation of polarization charge by the trapped holes in the α-NPD layer near the interface [17]. DCMs and TSC measurements on the degraded OLEDs need to be conducted in future to clarify the detailed relationship between SOP and OLED degradation.

5-4. Conclusion

The comprehensive effect of a structural control of amorphous films was investigated by evaluating performance of OLEDs with α-NPD and Alq_3 layers vacuum-deposited at different T_{sub}. I succeeded in controlling the SOP of Alq_3 films by changing T_{sub}. Although amorphous structures did not affect the electron transporting properties of Alq_3, the SOP probably affected electron injection and influenced the *J-V* properties of OLEDs. EQE was dramatically affected by T_{sub} and enhanced by 42% at most. Not only the fluorescence quantum yield and light outcoupling efficiency, but also the carrier balance and SPA associated with the SOP and accumulated interfacial charge were probably related to this EQE enhancement. Operational stability was also affected by T_{sub}. Further analysis are required to clarify the detailed mechanisms of the change in EQE and operational stability.

References

[1] T. Komino, H. Nomura, T. Koyanagi, C. Adachi, Suppression of efficiency roll-off characteristics in thermally activated delayed fluorescence based organic light-emitting diodes using randomly oriented host molecules, *Chem. Mater.* **25**, 3038–3047 (2013).

[2] T. Komino, H. Tanaka, C. Adachi, Selectively controlled orientational order in linear-shaped thermally activated delayed fluorescent dopants, *Chem. Mater*. **26**, 3665–3671 (2014).

[3] T. Komino, Y. Sagara, H. Tanaka, Y. Oki, N. Nakamura, H. Fujimoto, C. Adachi, Electroluminescence from completely horizontally oriented dye molecules, *Appl. Phys. Lett.* **108**, 241106 (2016).

[4] J. R. Ribé, P. A. Will, C. Hänisch, M. G. Silveira, S. Lenk, J. R. Viejo, S. Reineke, High-performance organic light-emitting diodes comprising ultrastable glass layers, *Sci. Adv.* **4**, eaar8332 (2018).

[5] Y. Qiu, L. W. Antony, J. J. de Pablo, M. D. Ediger, Photostability can be significantly modulated by molecular packing in glasses, *J. Am. Chem. Soc.* **138**, 11282–11289 (2016).

[6] Y. Qiu, L. W. Antony, J. M. Torkelson, J. J. de Pablo, M. D. Ediger, Tenfold increase in the photostability of an azobenzene guest in vapor-deposited glass mixtures, *J. Chem. Phys.* **149**, 204503 (2018).

[7] E. Ito, Y. Washizu, N. Hayashi, H. Ishii, N. Matsuie, K. Tsuboi, Y. Ouchi, Y. Harima, K. Yamashita, K. Seki, Spontaneous buildup of giant surface potential by vacuum deposition of Alq_3 and its removal by visible light irradiation, *J. Appl. Phys.* **92**, 7306–7310 (2002).

[8] Y. Okabayashi, E. Ito, T. Isoshima, M. Hara, Positive giant surface potential of tris(8-hydroxyquinolinolato) aluminum (Alq_3) film evaporated onto backside of Alq_3 film showing negative giant surface potential, *Appl. Phys. Express* **5**, 055601 (2012).

[9] T. Isoshima, Y. Okabayashi, E. Ito, M. Hara, W. W. Chin, J. W. Han, Negative giant surface potential of vacuum-evaporated tris(7-propyl-8-hydroxyquinolinolato) aluminum(III) [$Al(7\text{-}Prq)_3$] film, *Org. Electron.* **14**, 1988–1991 (2013).

[10] L. Jäger, T. D. Schmidt, W. Brütting, Manipulation and control of the interfacial polarization in organic light-emitting diodes by dipolar doping, *AIP Adv.* **6**, 095220 (2016).

[11] K. Osada, K. Goushi, H. Kaji, C. Adachi, H. Ishii, Y. Noguchi, Observation of spontaneous orientation polarization in evaporated films of organic light-emitting diode materials, *Org. Electron.* **58**, 313–317 (2018).

[12] Y. Noguchi, W. Brütting, H. Ishii, Spontaneous orientation polarization in organic light-emitting diodes, *Jpn. J. Appl. Phys.* **58**, SF0801 (2019).

[13] Y. Noguchi, Y. Miyazaki, Y. Tanaka, N. Sato, Y. Nakayama, T. D. Schmidt, W. Brütting, H. Ishii, Charge accumulation at organic semiconductor interfaces due to a permanent dipole moment and its orientational order in bilayer devices, *J. Appl. Phys.* **111**, 114508 (2012).

[14] Y. Noguchi, H. Lim, T. Isoshima, E. Ito, M. Hara, W. W. Chin, J. W. Han, H. Kinjo, Y. Ozawa, Y. Nakayama, H. Ishii, Influence of the direction of spontaneous orientation polarization on the charge injection properties of organic light-emitting diodes, *Appl. Phys. Lett.* **102**, 203306 (2013).

[15] D. Y. Kondakov, J. R. Sandifer, C. W. Tang, R. H. Young, Nonradiative recombination centers and electrical aging of organic light-emitting diodes: direct connection between accumulation of trapped charge and luminance loss, *J. Appl. Phys.* **93**, 1108–1119 (2003).

[16] T. Miyamae, N. Takada, T. Yoshioka, S. Miyaguchi, H. Ohata, T. Tsutsui, Rearrangement of the molecular orientation of Alq_3 in organic light-emitting diodes under constant current aging investigated using sum frequency generation spectroscopy, *Chem. Phys. Lett.* **616–617**, 86–90 (2014).

[17] T. D. Schmidt, L. Jäger, Y. Noguchi, H. Ishii, W. Brütting, Analyzing degradation effects of organic light-emitting diodes via transient optical and electrical measurements, *J. Appl. Phys.* **117**, 215502 (2015).

[18] Y. Noguchi, H. J. Kim, R. Ishino, K. Goushi, C. Adachi, Y. Nakayama, H. Ishii, Charge carrier dynamics and degradation phenomena in organic light-emitting diodes doped by a thermally activated delayed fluorescence emitter, *Org. Electron.* **17**, 184–191 (2015).

[19] Y. Noguchi, N. Sato, Y. Miyazaki, H. Ishii, Light- and ion-gauge-induced space charges in tris-(8-hydroxyquinolate) aluminum-based organic light-emitting diodes, *Appl. Phys. Lett.* **96**, 143305 (2010).

[20] Y. Esaki, T. Komino, T. Matsushima, C. Adachi, Enhanced electrical properties and air stability of amorphous organic thin films by engineering film density, *J. Phys. Chem. Lett.* **8**, 5891–5897 (2017).

[21] Y. Esaki, T. Matsushima, C. Adachi, Dependence of the amorphous structures and photoluminescence properties of tris(8-hydroxyquinolinato)aluminum films on vacuum deposition conditions, *Org. Electron.* **67**, 237–241 (2019).

[22] S. Berleb, W. Brütting, G. Paasch, Interfacial charges and electric field distribution in organic hetero-layer light-emitting devices, *Org. Electron.* **1**, 41–47 (2000).

[23] C. W. Tang, S. A. Vanslyke, Organic electroluminescent diodes, *Appl. Phys. Lett.* **51**, 913–915 (1987).

[24] T. Matsushima, Y. Kinoshita, H. Murata, Formation of Ohmic hole injection by inserting an ultrathin layer of molybdenum trioxide between indium tin oxide and organic hole-transporting layers, *Appl. Phys. Lett.* **91**, 253504 (2007).

[25] S. Scholz, D. Kondakov, B. Lüssem, K. Leo, Degradation mechanisms and reactions in organic light-emitting devices, *Chem. Rev.* **115**, 8449–8503 (2015).

[26] J. E. Knox, M. D. Halls, H. P. Hratchian, H. B. Schlegel, Chemical failure modes of AlQ3-based OLEDs: AlQ3 hydrolysis, *Phys. Chem. Chem. Phys.* **8**, 1371–1377 (2006).

[27] H. Aziz, Z. D. Popovic, N.-X. Hu. A.-M. Hor, G. Xu, Degradation mechanism of small molecule–based organic light-emitting devices, *Science* **283**, 1900–1902 (1999).

Chapter 6

Conclusion

In this thesis, I controlled structures of organic amorphous films by changing T_{sub} during vacuum deposition and investigated its effect on the fundamental electrical and PL properties and OLED performance. In Chapter 2, I succeeded in enhancing the electrical properties and air stability of α-NPD films by increasing their film densities. In Chapter 3, the precise analysis of the thermally stimulated currents revealed a possibility that the reduced carrier trap depth contributed to the enhanced electrical properties in the high-density α-NPD films. In the OLED research field, the concept of film density has been ignored for a long period of time. Here I demonstrated that film density significantly affected the carrier transport properties and air stability, which are key factors that determine OLED performance. In Chapter 4, I found that the PL properties of Alq_3 depended on the vacuum deposition conditions. Even with widely used vacuum deposition on room-temperature substrates, impurities have a possibility to be included in the films and act as quenchers. For obtaining the true PL properties, materials should be vacuum-deposited on substrates kept at higher temperature to reduce the inclusion of impurities. In Chapter 5, I analyzed how the structures of Alq_3 films affected the SOP and OLED performance. Active control of SOP was achieved by changing T_{sub}, and its impact on *J-V* properties, EQE, and operational stability was demonstrated. The detailed mechanism is now under consideration.

Finally, I state the future perspectives. In my study, the degradation of α-NPD-based HODs was suppressed by engineering the film density. If the film-density engineering demonstrated in this thesis can be combined with other technologies such as an inverted OLED architecture with air-stable metal oxide and Au electrodes [1], OLEDs with extremely high air stability will be realized. Insufficient operational stability and complicated device encapsulation processes used to manufacture OLEDs make a device cost higher and limit OLED commercialization. This study has an impact on not only establishing the fundamental science regarding organic amorphous systems but also promoting OLED industry.

Molecular orientation has been considered as one important factor that changes carrier transport properties in amorphous films. In contrast, I proved in this thesis that the carrier transport in α-NPD films was dominated by the film density while Alq_3 films had no clear relation to both molecular orientation and film density. This disagreement probably originates from the difference in their molecular shapes, details of which is still unclear. The single-crystal state with better molecular

packing is most favorable for carrier transport. In this thesis, I pursued the formation of the single-crystal-like molecular packing in amorphous state. Amorphous films have a relatively dense structure and its density is not far from that of a single crystal. For example, the density of a vacuum-deposited film of 4,4'-bis[*N*-(p-tolyl)-*N*-phenylamino]biphenyl (TPD) is 1.14 g/cm^3, which is approximately 94% of that of its single crystal (1.21 g/cm^3) [2,3]. Considering this difference in molecular packing below 10%, the 1%–2% change in film density as observed in Chapter 2 is expected to reduce the structural disorder in amorphous films significantly. In a previous report on a theoretical calculation, it was suggested that carrier transport in amorphous films is dominated by energetic disorder rather than structural disorder [4]. Estimation of activation energy of carrier hopping and DOS distribution will clarify the unknown physics on molecular condensed states and carrier transport properties and give us a guide for a new molecular design. Meanwhile, although vacuum deposition at a T_{sub} of 0.75–0.9 $T_{g, bulk}$ is necessary to fabricate high-density films with higher electrical properties and air stability, a control of processing temperature takes high cost and is not suitable for practical applications. However, the results obtained in this study indicate that a potential of organic materials can be maximized even with vacuum deposition on room-temperature substrates if organic materials with $T_{g, bulk}$ around 340–400 K are used to fabricate devices. Even though the scope of this thesis was the clarification of device physics, the present findings can provide a new molecular design strategy for advanced organic devices.

Through this thesis, the superiority of the "classical" vacuum deposition process was confirmed, which has been used by many researchers for a long time. However, I believe that the structural control of organic films by engineering molecular kinetics during film formation is not limited in some special cases but provides a general concept that will trigger the enhancement of the performance of various organic devices. I hope that this thesis contributes to future organic electronics.

References

[1] H. Fukagawa, K. Morii, M. Hasegawa, Y. Arimoto, T. Kamada, T. Shimizu, T. Yamamoto, Highly efficient and air-stable inverted organic light-emitting diode composed of inert materials, *Appl. Phys. Express* **7**, 082104 (2014).

[2] Z. Zhang, E. Burkholder, J. Zubieta, Non-merohedrally twinned crystals of *N*,*N*'-bis−(3-methyl−phenyl)-*N*,*N*'-diphenyl-1,1'-biphenyl-4,4'-diamine: an excellent triphenylamine-based hole transporter, *Acta Crystallogr. Sect. C: Cryst. Struct. Commun.* **60**, o452–o454 (2004).

[3] M. Shibata, Y. Sakai, D. Yokoyama, Advantages and disadvantages of vacuum-deposited and spin-coated amorphous organic semiconductor films for organic light-emitting diodes, *J. Mater. Chem. C* **3**, 11178–11191 (2015).

[4] F. Suzuki, S. Kubo, T. Fukushima, H. Kaji, Effects of structural and energetic disorders on charge transports in crystal and amorphous organic layers, *Sci. Rep.* **8**, 5203 (2018).

Lists of symbols and abbreviations

Symbols

C	Capacitance
C_{OLED}, C_{Alq3}	Capacitances of an OLED and an Alq_3 layer
d	Film thickness
d_t, $d_{t,cal}$	Hole trap depth and calibrated trap depth
e	Elementary charge
E	Electric field
E_c	Collecting field
f	Reduced electric field in ILC model
I	Current
I_0	Peak height in pseudo-Voigt function
J	Current density
k	Extinction coefficient
k_B	Boltzmann constant
k_{ISC}	Intersystem crossing rate constant
k_{nr}	Non-radiative decay rate constant
k_r	Radiative decay rate constant
k_q	Quenching rate constant
k_x, k_x	Extinction coefficients in directions parallel and perpendicular to a substrate plane
M	Mixing ratio of Lorentzian and Gaussian functions in pseudo-Voigt function
M_w	Molecular weight
n	Refractive index
n_x, n_z	Refractive indexes in directions parallel and perpendicular to a substrate plane
N_0	Number density of molecules
N_A	Avogadro constant
N_t	Hole trap density
P	Polarization density
$P_{\alpha\text{-NPD}}$, P_{Alq3}	Spontaneous orientation polarization of α-NPD and Alq_3 layers
Q	Electric charge
Q_1, Q_2, Q_{tot}	Induced charge on each electrode and total amount of induced charge
S	Orientation order parameter
S	Active device area
T	Temperature

T_g	Glass transition temperature
$T_{g,\,bulk}$	Glass transition temperature of a bulk film
T_m	Temperature at a TSC peak
T_{sub}	Substrate temperature
V	Voltage
V_{bi}	Built-in voltage
V_c	Collecting voltage
V_{fill}	Trap-filling voltage
V_{inj}	Injection voltage
V_s	Surface potential
V_{sat}	Saturation voltage
V_{th}	Threshold voltage
x_0	Peak position in pseudo-Voigt function
x_{av}	Average distance of trapped holes
x_m	Distance from electrode of the minimum point of electric potential
α	Asymmetric parameter in pseudo-Voigt function
α	Molecular polarizability
β	Heating rate
γ	Poole–Frenkel factor
Γ	Parameter for a peak width in pseudo-Voigt function
Δ	Ellipsometric angle
$\Delta\Phi$	Barrier lowering by external electric field
ε_0	Vacuum permittivity
ε_r	Relative permittivity
θ	Angle
θ_{TDM}, θ_{PDM}	Orientation degree of TDM and PDM to a substrate-normal direction
μ	Carrier mobility
$\mu(0)$	Zero-field carrier mobility
ρ	Film density
ρ_{abs}	Absolute film density
ρ_{rel}	Relative film density
σ_{acc}	Accumulated charge at an interface
σ_{int}	Interfacial charge
τ	Fluorescence lifetime
τ_0	Constant in Eq. (3-6)
Φ	Fluorescence quantum yield

Φ_B	Injection barrier height
Ψ	Ellipsometric angle

Abbreviations

Alq_3	Tris(8-hydroxyquinolinato)aluminum
α-NPD	*N*,*N*'-Di(1-naphthyl)-*N*,*N*'-diphenyl-(1,1'-biphenyl)-4,4'-diamine
CIP	Cold isostatic pressing
DCM	Displacement current measurement
DOS	Density of states
EL	Electroluminescence
EOD	Electron-only device
EQE	External quantum efficiency
H_2PC	Metal-free phthalocyanine
HOD	Hole-only device
HQ	Hydroxyquinoline
ILC	Injection-limited current
ITO	Indium tin oxide
LT80	Time at which luminance decreased to 80% of initial luminance
MSE	Mean-squared error
OLED	Organic light-emitting diode
PDM	Permanent dipole moment
PL	Photoluminescence
SOP	Spontaneous orientation polarization
SPA	Singlet-polaron annihilation
TADF	Thermally activated delayed fluorescence
TDM	Transition dipole moment
TPD	4,4'-Bis[*N*-(p-tolyl)-*N*-phenylamino]biphenyl
TSC	Thermally stimulated current
VASE	Variable angle spectroscopic ellipsometry

Publication lists

Original Papers

[1] **Y. Esaki**, T. Matsushima, and C. Adachi

"Current enhancement in organic films through gap compression by cold isostatic and hot isostatic pressing"

Advanced Functional Materials **26**, 2940–2949 (2016).

[2] **Y. Esaki**, T. Komino, T. Matsushima, and C. Adachi

"Enhanced electrical properties and air stability of amorphous organic thin films by engineering film density"

The Journal of Physical Chemistry Letters **8**, 5891–5897 (2017).

[3] **Y. Esaki**, T. Matsushima, and C. Adachi

"Dependence of the amorphous structures and photoluminescence properties of tris(8-hydroxyquinolinato) aluminum films on vacuum deposition conditions"

Organic Electronics **67**, 237–241 (2019).

[4] **Y. Esaki**, T. Matsushima, and C. Adachi

"Discussion on hole traps of amorphous films of *N*,*N*'-di(1-naphthyl)-*N*,*N*'-diphenyl-(1,1'-biphenyl)-4,4'-diamine (α-NPD) deposited at different substrate temperatures"

Applied Physics Letters **114**, 173301 (2019).

Joint Papers

[1] T. Matsushima, **Y. Esaki**, and C. Adachi

"Enhancement of the electrical characteristics of metal-free phthalocyanine films using cold isostatic pressing"

Applied Physics Letters **105**, 243301 (2014).

[2] T. Matsushima, A. S. D. Sandanayaka, **Y. Esaki**, and C. Adachi

"Vacuum-and-solvent-free fabrication of organic semiconductor layers for field-effect transistors"

Scientific Reports **5**, 14547 (2015).

[3] T. Matsushima, T. Fujihara, C. Qin, S. Terakawa, **Y. Esaki**, S. Hwang, A. S. D. Sandanayaka, W. J. Potscavage, Jr., and C. Adachi

"Morphological control of organic–inorganic perovskite layers by hot isostatic pressing for efficient planar solar cells"

Journal of Materials Chemistry A **3**, 17780 (2015).

[4] T. Matsushima, S. Yoshida, K. Inada, **Y. Esaki**, T. Fukunaga, H. Mieno, N. Nakamura, F. Bencheikh, M. R. Leyden, R. Komatsu, C. Qin, A. S. D. Sandanayaka, and C. Adachi

"Degradation mechanism and stability improvement strategy for an organic laser gain material 4,4'-bis[(*N*-carbazole)styryl]biphenyl (BSBCz)"

Advanced Functional Materials **29**, 1807148 (2019).

[5] A. Mikaeili, T. Matsushima, **Y. Esaki**, S. A. Yazdani, C. Adachi, and E. Mohajerani

"The origin of change in electrical properties of organic layers fabricated at various vacuum deposition rate"

Optical Materials **91**, 93–100 (2019).

Acknowledgements

The studies in this thesis were carried out at Adachi laboratory, Department of Chemistry and Biochemistry, Graduate School of Engineering, Kyushu University from 2015 to 2020.

First, I am deeply grateful to Professor Chihaya Adachi for supervising this thesis, excellent experimental environment, helpful discussion, and exact comments and advice for all of my works. I am also deeply grateful to Professor Takuma Yasuda and Professor Yuji Oki for co-supervising this thesis. I would like to express my special gratitude to Associate Professor Toshinori Matsushima for teaching me the research from A to Z and giving me a chance to devote this fantastic topic. I also deeply express my gratitude to Associate Professor Takeshi Komino, who now belongs to University of Hyogo, for insightful discussion and kind advice. I would like to thank Associate Professor Hajime Nakanotani, Associate Professor Kenichi Goushi, and Mr. Masaki Tanaka for helpful discussion and comments.

I also acknowledge all members of Adachi laboratory and all people who I met through my works for their supports not only for my work but also my daily life. Finally, I would also like to thank to my family and friends for their kind supports and encouragements.

January, 2020

Yu Esaki